Molecular Dynamics Study of Phase Transition Phenomena

Changman Moon

The degree of Doctor of Philosophy

University of Edinburgh

2000

Abstract

This computer simulation study carried out by classical the molecular dynamics technique (MD) investigates structural phase transitions of various atomic and molecular condensed matter systems. Particularly, our attention is focused on the signals for their observation.

Classical nucleation theory is briefly reviewed in relation to the present study. An overall review is made on the methodology of the MD simulation technique such as the integration of the equations of motion, the rotational motion of molecules which is dealt with the four-component quaternion, and other various techniques involved with the simulation of atomic clusters, the simulation of bulk molecular systems using periodic boundary conditions, and isobaric molecular dynamics.

There are also reviews on measurements of thermodynamic quantities which are monitored during the simulation including the pressure, the kinetic energy, and the potential energy as well as their corrections due to the spherical cutoff. In addition, various analysis techniques for the observation of the signals of structural phase transitions are discussed. All the potential functions used in this study are of the pairwise additive atom-atom Lennard-Jones interaction for both the atomic and the molecular systems.

A small cluster of a binary mixture of krypton and argon atoms is studied by triggered breathing motions to investigate anharmonic motion which involves the structural phase transitions. A small cluster of krypton atoms is also simulated and discussed in detail concerning the very first moment of nucleation in relation to five-fold symmetric structures.

In simulations of sulphurhexafluoride molecule systems, artifacts of finite size and periodic boundary conditions are investigated. Freezing the system by MD is investigated since it is known to supercool in computer simulations. Furthermore, accelerating the nucleation process by various methods such as shear flow, accelerated layer, inclusion of defect molecules, and pressure fluctuations is investigated.

Reorientational diffusion motions are studied for a system of sulphurhexafluoride solvent molecules into which linear defects are included to understand experimental results made by NMR and Raman scattering measurements. Theoretical models for reorientational diffusion motion of molecules are reviewed and extended for the spherical top molecule allowing comparisons to be made for the model functions with the MD simulation results.

Acknowledgements

First of all, I am pleased to thank Stuart Pawley for indepth supervision to my scientific reasoning. I would also like to thank my parents and grandparents, especially my grandfather to whom I owe more than words can describe for his lifelong love and devotion. I wish to dedicate this work to those who have given meaning to my life – to my lovely wife, Jeoungeun, for her unfailing encouragement and forbearance with what has seemed a never ending process and my little daughter, Chaewon, for allowing me a good night's sleep. Last but not least, I thank God for guidence throughout the work.

Declaration

This thesis has been composed by myself and it has not been submitted in any previous application for a degree. The work reported within was executed by me, unless otherwise stated.

Changman Moon

December 1999

Contents

Chapter 1

Introduction

1.1 Nucleation

Water evaporates when it is heated over its boiling point, vapour condenses back into water as it is cooled down to under the boiling point, and becomes ice as cooled further under its freezing point. This is a simplest and a commonly referred example in phase transitions. Such transition behaviours are seen throughout nature.

Macroscopic changes between phases, the solid, the liquid, and the gas, may be observed directly without the aids of sophisticated instruments. However, as we approach to the point where transitions happen, detailed physical changes are rather ambiguous. At the very beginning of a transition, microscopic changes occur and they are the driving forces behind the macroscopic changes. The detailed physics may only be revealed by dynamics of localised groups of atoms. Such transition behaviours therefore have been focussed over a long time and are still an important topic in physics.

In a metastable state a small number of atoms or molecules in a system begins to form an ordered phase in which symmetry is broken. Such formations happen throughout the system and are easily destroyed by thermal fluctuation until they grow to a certain size called the critical nucleus at which they can withstand the thermal fluctuations and grow further. Nucleation is the appearance of such a localised new

stable phase in a metastable state.

The rate of nucleation of a system often affects the property of the system and therefore has been a key part of nucleation study. In 1935, Becker [1] proposed an equation for the rate of homogeneous nucleation in condensed systems given in a exponential functional form, in which the exponent is a sum of the maximum free energy necessary for nucleus formation and the activation energy for diffusion across the phase boundary, with an undefined constant. This was later extended by Turnbull and Fisher [2] in 1949 known as classical nucleation theory (CNT). They derived the undefined constant on the basis of the theory of absolute reaction rates [3]. Recent development in the nucleation theory was made by density functional approaches (DFA) [4, 5] and the difference between CNT and DFA raised questions about the validity of using nucleation experiments to measure liquid-solid surface free energies [5], and questioning CNT.

In CNT, a nucleation rate essentially depends on the surface free energy between phases such as gas-liquid, liquid-solid. In case of the gas-liquid nucleation study in experiment, the surface tension of the liquid is equated to the gas-liquid surface free energy. Experimental results are limited [6] since the surface free energy and the surface tension are no longer equal in liquid-solid nucleation due to the possible strain in the crystals and even devising a measurement method for the interfacial tension is not simple.

Computer simulation techniques such as the Monte Carlo method and the Molecular Dynamics method were also applied due to the fact that the simulation methods can produce considerablely detailed information on simulated samples. Although the computer time scale in simulation methods is limited compared to the experimental time scale, simulation methods have grown extensively in the study of nucleation.

Mandell, McTague, and Rahman [7] first observed nucleation by means of the structure factor in MD simulations of 128-particle Lennard-Jones systems. Subsequently, a

large number of MD simulation studies followed [8, 9, 10, 11]

Although the main themes of nucleation theories are focused on the rate of nucleation rather than on the kinetics of the nucleation process and are not directly related to this work due to the fact that no consideration will be made of the rate of nucleation in this work, it is worth briefly including nucleation theories with an interest in the nucleation process.

1.2 Classical nucleation theory (CNT)

In 1949, Turnbull and Fisher [2] extended the work of Becker and Döring [1] on the homogeneous nucleation of the gas-liquid transition to the liquid-solid transition. They assumed the local free energy change associated with the formation of a region of a new phase β in a parent phase α as

$$\Delta F_i/kT = Ai^{2/3} - Bi.$$

In this equation i is the number of atoms or molecules in the transformed region. A is proportional to the interfacial free energy per unit area of α-β-interface, and B is proportional to the bulk free energy difference between β and α in the absence of surfaces. $\Delta F_i/kT$ has its maximum at $i^* = 2A/3B$. In this equation the free energy increases until the number of atoms or molecules in the transformed region reaches i^*, which is called the critical nucleus. Those of transformed region containing more than i^* grow freely with decreasing free energy. Small nuclei containing fewer atoms than i^* are likely to disappear due to thermal fluctuations though a long sequence of favourable energy fluctuations sometimes produces a nucleus exceeding the critical size.

Based upon the theory of absolute reaction rates [3], a chemical reaction or other rate process is characterised by continuous change of coordinates from an initial configuration into the final configuration through a intermediate configuration, called the activated complex of the reaction, which is essential for the process and when it is

attained there is a high probability that the reaction will continue to completion. They derived the following equation for the steady state rate of nucleation,

$$r^* \simeq (NkT/h)\exp[-(\Delta f^* + \Delta F^*)/kT]$$

nuclei per mole per second to an order of magnitude where Δf^* is the free energy of activation for the short-range diffusion of atoms or molecules across an interface to join a new lattice and ΔF^* is the maximum free energy necessary for nucleus formation.

Chapter 2

Molecular Dynamics Methods

2.1 Introduction

When the first computer was introduced to the world of science, its main purpose was to spare the tedium of work which no human could do better. Although it was no more than a simple computing device, it soon liberated all areas in science.

With understanding of the interactions between constituents of a system, it is possible both to find the trajectories of every particle by calculating all forces acting on each particle and to examine the physical properties under the change of thermodynamic conditions. Simulation of the evolution of a system due to interaction forces produces valuable information about particles under various external conditions and may open a simple way to study structural changes of matter. Although Newton's work was mainly to understand the motion of planets and their moons to which the same mechanical laws and the same universal gravitational attraction apply to all large bodies, his conception of nature can apply down to the atomic scale under the careful consideration of interatomic forces.

Molecular motion is basically described by both translation and rotation while in a atomic system, only the description of translational motion is needed. Rotational motion of molecules is known to be governed strongly by intermolecular forces and

torques, and determines physical characteristics of condensed phases. Rotational motion is therefore an essential part in the study of dynamics of molecular systems and understanding the motion is indispensable for physical model building for molecular dense phases. On this quest, considerable research activities have been devoted to the study of rotational motions of molecules, in theory [12, 13, 14, 15, 16, 17, 18, 19, 20], in experiment [21, 22, 23], and in computer simulation [24, 25, 26].

In theory, the usual approach to the rotational dynamics in a condensed phase is to postulate a model which describes a plausible physical dynamics of the system, such as collisions and free rotations. Few parameters of the model are then subjected to adjustment to agree with experimental results. Since reorientation motion of molecules varies broadly from an almost free rotation to a complete constraint by neighbouring molecules, there is therefore a limitation in applicability of a particular model developed for a particular system.

Advances in computer technology in the late 1950's allowed the development of a computationally intensive method: the molecular dynamics(MD) simulation method. The MD simulation method computes phase-space trajectories of a collection of molecules which individually obey classical laws of motion. Alder and Wainwright [27] first simulated a hard sphere system using the MD technique to study the relaxations accompanying various nonequilibrium phenomena with several systems(32, 96, and 108 particles)and the first simulation of an atomistic system was performed by Rahman in 1964 [28] with a system of 864 liquid argon particles and a time step of 0.01ps using the Lennard-Jones potential [29].

In a MD simulation, the integration of equations of motion at every step involves intensive computation. As far as system size is concerned, with a system of N point particles in three dimensions, the number of positions and momenta produced in every step of integration is 6N. For 100 steps for 100 particles, the amount of data produced is thus 6×10^4 numbers. In case of molecular simulations, more calculations are required

for rotational motion. It is clear that the larger the simulated size, the more computer memory and speed would be required. System size and computation time are, in general, subject to the availability of appropriate computers.

Although it has been a tendency that the sizes of simulation systems have been growing rapidly in conjunction with the development of modern computers, certain areas in MD simulation require no more computing power than can be delivered by ordinary workstations. In some of this work, some simulations were performed on a Hewlett–Packard workstation in order to study the nucleation phenomena. It is also possible, in practice, to increase the system size up to 1×10^5 atoms for the workstation with a cost of time. Recent development in personal computer industries has also achieved great advance in computing power as well as in memory size, made PC possible to be used in serious scientific area. There even exists a parallel computing environment configured with numerous networked PCs. Increasing network communication capability also promises its practicality.

In this chapter, the aim is to give an overview of the fundamental formulation of the molecular dynamics techniques relevant to this work.

2.2 Thermodynamic Quantities

Temperature is directly derived by the equipartition theorem of kinetic theory. This states that in atomic systems the average translational kinetic energy of each atom is given by $\frac{3}{2}k_BT$, where k_B is the Boltzmann constant,

$$\langle E_t \rangle = \sum_{i=1}^{N} \frac{1}{2} \frac{m_i |\vec{v}_i|^2}{N} = \frac{3}{2} k_B T_t.$$

where we call T_t the translational temperature. In molecular systems with fixed bond lengths and angles, there is an angular velocity term in the definition of temperature due to the fact that molecules have rotational degrees of freedom. Therefore, the average rotational kinetic energy, $\langle E_r \rangle$, is defined as,

$$\langle E_r \rangle = \sum_{i=1}^{N} \frac{1}{2} \frac{I_i |\vec{\omega}_i|^2}{N} = \frac{3}{2} k_B T_r$$

where I_i is the inertia tensor, ω_i the angular velocity of molecule i, and T_r the rotational temperature.

The thermodynamic temperature of a system is defined as the average of the translational temperature, T_t, and the rotational temperature, T_r,

$$T = \frac{1}{2}(T_t + T_r).$$

Pressure is likewise derived from the virial theorem.

$$PV = N k_B T + \frac{1}{3} \sum_{i=1}^{N} \sum_{j>i}^{N} \vec{f_{ij}} \cdot \vec{r_{ij}}$$

and

$$\vec{r_{ij}} = (\vec{r_j} - \vec{r_i})$$

where, for atomic systems, $\vec{f_{ij}}$ and $\vec{r_{ij}}$ stand for the force acting on an atom i from an atom j, and the vector between two atoms respectively. However, for molecular systems, $\vec{f_{ij}}$ is the force acting on an atom of molecule i from an atom of molecule j and $\vec{r_{ij}}$ is the vector between these two molecules. We shall consider a molecular system with site-site pairwise interactions and pressure shall be presented as follow.

The interaction between a pair of molecules i and j is a function of their relative positions $\vec{r_i}$, $\vec{r_j}$ and orientations, $\vec{\Omega}_i$, $\vec{\Omega}_j$. In a simplified 'site-site' approximation model, the total interaction is a sum of pairwise contributions from distinct sites a in molecule i, at position $\vec{r}_{ia}$, and b in molecule j, at position $\vec{r}_{jb}$

$$\Phi(r_{ij}, \vec{\Omega}_i, \vec{\Omega}_j) = \sum_{a,b} \Phi_{ab}(|\vec{r}_{ia} - \vec{r}_{jb}|)$$

where Φ_{ab} is a pair potential acting between sites a and b.

For the Lennard-Jones potential,

$$\Phi = \left(-\frac{A}{r_{ab}^6} + \frac{B}{r_{ab}^{12}} \right).$$

From the virial theorem

$$P = \rho k_B T + \mathcal{W}/V$$

where $N/V = \rho$ the molecular number density, T temperature, and $\mathcal{W}$ is the internal virial, defined as follows

$$\begin{aligned} \mathcal{W} &= \frac{1}{3} \sum_{i,j>i} \vec{r}_{ij} \cdot \vec{f}_{ij} \\ &= -\frac{1}{3} \sum_{i,j>i} \vec{r}_{ij} \cdot \nabla_{r_{ij}} \Phi(r_{ij}, \vec{\Omega}_i, \vec{\Omega}_j) \end{aligned}$$

where $\vec{r}_{ij}$ is the vector between centres of two molecules i and j, and $\vec{f}_{ij}$ the force on molecule i due to molecule j.

$\mathcal{W}$ can then be rewritten with the 'site-site' pair potential Φ_{ab} as follows,

$$\mathcal{W} = -\frac{1}{3} \sum_{i,j>i} \left[\vec{r}_{ij} \cdot \sum_{a,b} \frac{\partial \Phi_{ab}(r_{ab})}{\partial r_{ij}} \right]$$

and

$$\frac{\partial \Phi_{ab}}{\partial r_{ij}} = \frac{\partial \Phi_{ab}}{\partial r_{ab}} \frac{dr_{ab}}{dr_{ij}}$$

where $dr_{ab}/dr_{ij} = 1$ as we are considering a homogeneous volume change. Thus

$$\frac{\partial \Phi_{ab}(r_{ab})}{\partial r_{ab}} = \left(\frac{6A}{r_{ab}^8} - \frac{12B}{r_{ab}^{14}} \right) \vec{r}_{ab} \, .$$

Thus, $\mathcal{W}$ is written as follows,

$$\mathcal{W} = -\frac{1}{3} \sum_{i,j>i} \sum_{a,b} \left(\frac{6A}{r_{ab}^8} - \frac{12B}{r_{ab}^{14}} \right) (\vec{r}_{ab} \cdot \vec{r}_{ij})$$

and the pressure

$$P = \rho k_B T - \frac{1}{3V} \sum_{i,j>i} \sum_{a,b} \left(\frac{6A}{r_{ab}^8} - \frac{12B}{r_{ab}^{14}} \right) (\vec{r}_{ab} \cdot \vec{r}_{ij}).$$

However, it is common to use a spherical cutoff with a pair potential to save computation time.

2.3 Pressure and Energy correction due to spherical cutoff

In certain computer simulations, a pair potential is used with a spherical cutoff at r_c to reduce computation. As a result, thermodynamic quantities such as the energy and pressure must be corrected for the long-range part of the potential.

For a molecule with n atomic sites, the energy correction can be written as follow,

$$\begin{aligned} E_c &= \frac{N}{2} \int_{r_c}^{\infty} n^2 w(r) 4\pi r^2 \rho dr \\ &= 2n^2 \rho \pi N \left(-\frac{A}{3{r_c}^3} + \frac{B}{9{r_c}^9} \right) \end{aligned}$$

where $w(r)$ is the intermolecular pair virial function given by

$$w(r) = r \cdot \frac{d\Phi(r)}{dr}$$

and, for a Lennard-Jones potential,

$$\Phi(r) = -\frac{A}{r^6} + \frac{B}{r^{12}},$$

$w(r)$ is then

$$w(r) = \frac{6A}{r^6} - \frac{12B}{r^{12}}.$$

Therefore, the average energy correction $\langle E_c \rangle$ is

$$\langle E_c \rangle = 2n^2\pi\rho\left(-\frac{A}{3{r_c}^3}+\frac{B}{9{r_c}^9}\right).$$

Here, we would like to generalise the correction in case of having more than one species which interact with a same potential. Then, we shall have n_1 with its number density ρ_1, n_2 with ρ_2,..., and n_k with ρ_k where k is the number of species. Therefore, the above correction term for the energy is written as a generalised form,

$$\begin{aligned}\langle E_c \rangle &= 2n^2\pi\rho\left(-\frac{A}{3{r_c}^3}+\frac{B}{9{r_c}^9}\right)\left(n_1^2\rho_1+n_2^2\rho_2+\cdots+n_k^2\rho_k\right)\\ &= 2\pi\sum_{i=1}^{k}\left(n_i^2\rho_i\right)\left(-\frac{A}{3{r_c}^3}+\frac{B}{9{r_c}^9}\right).\end{aligned}$$

The correction term for the pressure P_c for a spherical cutoff at a distance of r_c can be written as

$$\begin{aligned}P_c &= -\frac{N}{6V}\int_{r_c}^{\infty} n^2 w(r) 4\pi r^2 \rho dr\\ &= -\frac{2}{3}n^2\pi\rho^2\int_{r_c}^{\infty} r^2 w(r) dr\end{aligned}$$

where $\rho = N/V$ is the molecular number density.

The pressure correction therefore is written as follow,

$$\begin{aligned}P_c &= -\frac{2}{3}n^2\pi\rho^2\int_{r_c}^{\infty}\left(\frac{6A}{r^4}-\frac{12B}{r^{10}}\right)dr\\ &= -\frac{2}{3}n^2\pi\rho^2\left[-\frac{2A}{r^3}+\frac{4B}{3r^9}\right]_{r_c}^{\infty}\\ &= -\frac{2}{3}n^2\pi\rho^2\left(\frac{2A}{r_c^3}-\frac{4B}{3r_c^9}\right).\end{aligned}$$

In the computation of the pressure correction, only the molecular number density ρ changes. The force calculation is done for atomic distances, which are less than r_c.

Here, the generalised form of the pressure correction is also written as

$$P_c = -\frac{2\pi}{3}\sum_{i=1}^{k}\left(n_i^2\rho_i^2\right)\left(\frac{2A}{r_c^3} - \frac{4B}{3r_c^9}\right) .$$

Therefore, the pressure with the correction term is written as follows,

$$P = k_B\sum_{i=1}^{k}\rho_i T_i - \frac{1}{3V}\sum_{i,j>i}\sum_{a,b}\left(\frac{6A}{r_{ab}^8} - \frac{12B}{r_{ab}^{14}}\right)(\vec{r}_{ab}\cdot\vec{r}_{ij}) - \frac{2\pi}{3}\sum_{i=1}^{k}\left(n_i^2\rho_i^2\right)\left(\frac{2A}{r_c^3} - \frac{4B}{3r_c^9}\right)$$

where T_i is the temperature of each species.

2.4 Entropy representation

We shall assume a system under analysis is close to equilibrium. In this way our calculation of thermodynamic quantities for the system will have somewhat meaningful validity. Here we like to have entropy representation simply as an indicator for the system.

At each velocity rescaling, there is a transfer of energy dQ either to or from the system at a given temperature T where this transfer takes place. Therefore entropy change can be calculated.

The mean kinetic energy per molecule increases on velocity rescaling by a factor α,

$$\frac{1}{2}\left(m|\vec{v}|^2 + I|\vec{\omega}|^2\right) \longrightarrow \frac{1}{2}\left(m\alpha^2|\vec{v}|^2 + I\alpha^2|\vec{\omega}|^2\right),$$

and we can write

$$dQ = 3k_BT\left(\alpha^2 - 1\right),$$

since

$$\frac{1}{2}m|\vec{v}|^2 = \frac{1}{2}I|\vec{\omega}|^2 = \frac{3}{2}k_BT.$$

Therefore, entropy change is written as,

$$dS = \frac{dQ}{T} = 3k_B\left(\alpha^2 - 1\right).$$

It should be noted that the entropy change is also a valuable means of observing equilibrium. It is possible to identify equilibrium state of a system by continuous summing over entropy changes.

2.5 Integrating the equations of motion

Solving an ordinary differential equation involves an initial condition and a rate, and is the so-called initial-value problem. To solve the differential equation on a computer finite difference schemes are employed and performed in a step–wise way. At each step approximations for trajectories, such as positions and velocities, are obtained as the integration proceeds in time. The third-order Strömer algorithm, first used by Verlet [30], has been widely used in molecular dynamics simulations and is known as Verlet's method. The same level of approximation can be obtained when Beeman's algorithm [31] is used, which produces both positions and velocities whereas traditional Verlet algorithm produces positions only. Beeman's algorithm is written as,

$$u(t+\delta t) = u(t) + v(t)\delta t + \frac{1}{6}[4a(t) - a(t-\delta t)]\delta t^2 \ .$$

At new positions $u(t+\delta t)$ finds new accelerations $a(t+\delta t)$ and then new velocities are

$$v(t+\delta t) = v(t) + \frac{1}{6}[2a(t+\delta t) + 5a(t) - a(t-\delta t)]\delta t$$

where u, v, a denote the position, velocity, and acceleration respectively, t, $t-\delta t$, $t+\delta t$ are used here as the current, the previous, and the next time for which the approximation is made. The time step used for atomic simulations is order of 0.005ps and 0.01ps for molecular simulations. The choice of time steps depend on the characteristics of the molecules used, such as masses and potential parameters.

2.6 Rotational Motion

The simulation of molecular systems involves not only translational motion but also the rotational motion of molecules. For such rotational motion, quaternions, invented by Sir William R. Hamilton in 1843, have first been applied by Evans, due to the advantages [32] of a singularity free procedure for orienting a rigid body in space. Computation can also be improved by avoiding trigonometric functions as used in Euler angles.

A rotation of an angle α of a body about the unit vector $\vec{r}$ is described by the quaternion,

$$\mathbf{q} = (\cos(\alpha/2), \vec{r}\sin(\alpha/2)),$$

where $0 \leq \alpha/2 < 2\pi$. This can be written as $\mathbf{q} = (L_4, \vec{L})$ where $\vec{L} = (L_1, L_2, L_3)$. Quaternions are subject to the following rules of addition and multiplication.
If $\mathbf{q} = (w, \vec{v})$ and $\mathbf{q}' = (w', \vec{v}')$, then

$$\mathbf{q} + \mathbf{q}' = (w + w', \vec{v} + \vec{v}')$$

$$\mathbf{q}\mathbf{q}' = (ww' - \vec{v} \cdot \vec{v}', w\vec{v}' + w'\vec{v} + \vec{v} \times \vec{v}')$$

Transformation of a quaternion, $\mathbf{q} = (0, \vec{v})$, involving the three-dimensional vector, $\vec{v}$, can be written as,

$$\mathbf{q}' = (0, \vec{v}') = \mathbf{p}\mathbf{q}\mathbf{p}^{-1} \ . \tag{2.1}$$

Following the rule of multiplication, the right-hand side of equation 2.1, $\mathbf{p}\mathbf{q}\mathbf{p}^{-1}$, is evaluated explicitly and we then obtain

$$\vec{v}' = (1 - 2L^2)\vec{v} + 2(\vec{v} \cdot \vec{L})\vec{L} - 2L_4\vec{v} \times \vec{L}. \tag{2.2}$$

The equation 2.2 can be rewritten as,

$$\vec{v}' = \mathbf{R}(L_i)\vec{v}$$

where the transformation matrix $\mathbf{R}$ is

$$\mathbf{R} = \begin{pmatrix} \mathbf{1} - 2({L_2}^2 + {L_3}^2) & 2(L_1L_2 - L_3L_4) & 2(L_1L_3 + L_2L_4) \\ 2(L_1L_2 + L_3L_4) & \mathbf{1} - 2({L_1}^2 + {L_3}^2) & 2(L_2L_3 - L_1L_4) \\ 2(L_1L_3 - L_2L_4) & 2(L_2L_3 + L_1L_4) & \mathbf{1} - 2({L_1}^2 + {L_2}^2) \end{pmatrix} .$$

If we denote $\vec{v}$ as the position of an atom in a molecule, then the new atomic position is defined as $\mathbf{R}(L_i)\vec{v}$. If the molecule makes another rotation by the rotational matrix $\mathbf{\Omega}(\delta t)$ after time δt, its new position is written as,

$$\mathbf{\Omega}(\delta t)\mathbf{R}(L_i)\vec{v} = \mathbf{R}(L'_i)\vec{v}$$

where L'_i are the components of the quaternions describing the new orientations and

$$L'_i = L_i + \dot{L}_i\delta t \ . \tag{2.3}$$

If the angular velocity of the molecule is $\vec{\omega}$, a small angular displacement for time δt is $\frac{1}{2}\vec{\omega}\delta t$. This displacement as a quaternion is $(1, \frac{1}{2}\vec{\omega}\delta t)$ since $L_4 \cong 1$ that the rotation angle is very small. Therefore the quaternion which describes the rotated position is written as

$$L'_i = (1, \frac{1}{2}\vec{\omega}\delta t)(L_4, \vec{L})$$

$$= (L_4 - (\vec{\omega}\cdot\vec{L})\frac{\delta t}{2}, \vec{L} + (\vec{\omega}L_4 + \vec{\omega}\times\vec{L})\frac{\delta t}{2}) \ . \tag{2.4}$$

From equations 2.3 and 2.4 we find $(\dot{L}_4, \dot{\vec{L}})$,

$$\dot{\vec{L}} = \frac{1}{2}(\vec{\omega}L_4 + \vec{\omega}\times\vec{L}),$$

$$\dot{L}_4 = -\frac{1}{2}(\vec{\omega} \cdot \vec{L}) \ . \tag{2.5}$$

Finally, differentiation of equation 2.5 with respect to time establishes the equations of motion for molecular orientation in terms of quaternions, $(\ddot{L}_4, \ddot{\vec{L}})$,

$$\ddot{\vec{L}} = \frac{1}{2}(\dot{\vec{\omega}} L_4 + \vec{\omega}\dot{L}_4 + \dot{\vec{\omega}} \times \vec{L} + \vec{\omega} \times \dot{\vec{L}}) \ .$$

$$\ddot{L}_4 = -\frac{1}{2}(\dot{\vec{\omega}} \cdot \vec{L} + \vec{\omega} \cdot \dot{\vec{L}}) \ .$$

2.7 Molecular Bulk Simulation

Systems in typical MD simulation contain about a few thousand atoms or less. They, therefore, inevitablely incorporate the so-called surface effects that such systems are normally simulated as either contained in walls or confined in space, cluster simulation, resulting that atoms interact with the container walls or are under different pressure due to the interaction between atoms. The surface effect greatly influence physical properties of the system under investigation. If the surface effects or the systems under the surface effects themselves are not of interest, they can be removed by employing periodic boundary conditions (PBC).

The method (PBC) allows a system, the MD cell, to be copied infinitely throughout space, and therefore, the movements of atoms in the original MD cell are exactly the same as in all neighbouring cells. In such a way, the MD cell does not have boundaries in all directions.

The cubic boundary conditions is commonly used due to its simplicity although there exist other variants such as the method developed by Parrinello and Rahman [33]. It allows changes in the shape of the MD cell so that strain caused due to structural changes in solid phase simulations is relaxed. Another variant [34] was to simulate shear flow by allowing each layer of the periodic cells to drift against each other.

Despite the usefulness in simulating bulk systems, it is affected by the size of the system basically due to the fact that atoms will feel themselves if the system size is

small and the cell length is, therefore, short compared to the interaction distance for force calculation. The atoms in the system may well be highly correlated themselves under limited system sizes.

2.8 Constant Pressure MD

Several methods [35, 33, 36, 37] have been proposed for isobaric MD simulations. The simplest method can be devised by systematically changing the volume of a container where particles may be kept inside.

Let us consider a volume, V, which is to be changed to a new volume, V', in order to maintain a certain pressure. The volume ratio β

$$\beta = \frac{V'}{V} \tag{2.6}$$

where

$$\begin{cases} \beta < 1.0 & : \text{ volume decreased,} \\ \beta = 1.0 & : \text{ no change,} \\ \beta > 1.0 & : \text{ volume increased.} \end{cases}$$

The physical meaning of the ratio, β, can be found from the definition of the bulk modulus, K, which is defined as

$$\mathrm{K} = -\frac{\text{force per unit area}}{\text{change in volume per unit volume}} = -\frac{p}{\Delta V/V} = -\frac{p}{(\beta - 1)}$$

where p is the pressure applied. Therefore the ratio β can be found if the bulk modulus and the pressure applied are known within the Hooke's regime where the response is linear.

More conveniently, constant pressure shall be maintained using the method, proposed by Andersen [35], which allows the volume change according to the internal pressure of the system. In this method, a periodic box volume is allowed to change in

every time step so that the pressure of the system is maintained at a constant value. In order to realise such volume change, let us consider a volume which expands or contracts isotropically in 3-dimensions as in the figure 2.1.

The box may be regarded as a isotropic piston with a mass term M(the unit of [mass][length]$^{-4}$) and a volume V except for the fact that a normal piston expands or contracts the system along only one direction. The kinetic energy of the piston can be written as

$$K_p = \frac{1}{2}M\dot{V}^2.$$

If we let p be the instantaneous pressure of a system and p_o be the specified pressure, and P the difference between these two pressures, the potential energy V_p associated with the piston is

$$V_p = (p - p_o)V = PV.$$

Therefore, the Lagrangian L_p for the piston is

$$L_p = K_p - V_p = \frac{1}{2}M\dot{V}^2 - PV$$

and an equation of motion can be obtained directly from the Lagrangian,

$$\ddot{V} = \frac{P}{M} = \frac{(p - p_o)}{M}.$$

Here, the imbalance P between the two pressures will cause the piston to accelerate. As the motion of the atoms causes the internal pressure to fluctuate, the piston volume will fluctuate and the time scale for this fluctuation is determined by the piston mass M. The mass should be chosen carefully since the fluctuation of the piston volume would be too sensitive to the fluctuation of the internal pressure if we chose too small a value, or too insensitive if it is too large. However, the time scale of the fluctuation of the piston volume must be somewhat larger than the time step used. In this work the

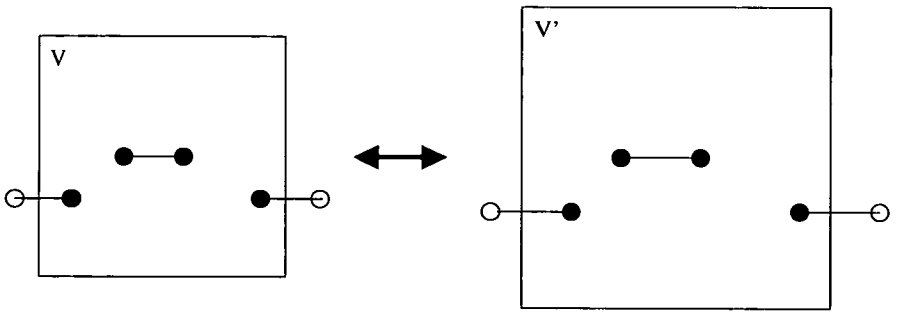

Figure 2.1: Isotropic expansion or contraction

piston mass M of 0.0008 is used, which allows the piston to fluctuate approximately 15 times slower than thermal fluctuations.

After the volume change coordinates of atoms must be changed according to the volume change. Since the volume change is isotropic and β as defined in the equation 2.6 is a scalar for the volume, the scalar for the length is then $\beta^{1/3}$. Therefore the atomic (or molecular centre) coordinates $\vec{r_i}'$ in the new periodic box can be written,

$$\vec{r_i}' = \beta^{1/3}\vec{r_i}$$

where $\vec{r_i}$ are the coordinates of atoms before the volume change.

2.9 Molecular Cluster Simulation

Clusters have a space boundary called the surface, giving rise to surface tension which acts to minimise the surface area. There are some difficulties involved with cluster simulations such as having high translational and rotational kinetic energies which make analysis difficult. Therefore several procedures must be taken.

First, the coordinate system of a cluster has to be transformed to its centre of mass. With N equal point masses, this is done by,

$$\vec{r_i}'(t) = \vec{r_i}(t) - \frac{1}{N}\sum_{j=1}^{N}\vec{r_j}(t).$$

Since clusters may have an overall linear and angular momentum which cause the cluster to move and rotate, both momenta should be removed in order to focus our attention only on its own internal motion.

The linear momentum can be removed by changing velocities,

$$\vec{v}_i'(t) = \vec{v}_i(t) - \frac{1}{N}\sum_{j=1}^{N} \vec{v}_j(t).$$

There are two contributions to the angular momentum, one due to the movement of molecules about the cluster centre $\vec{L}_t$ and the other due to the individual rotation of every molecule $\vec{L}_r$.

The angular momentum, $\vec{L}_t$, is calculated as,

$$\vec{L}_t = \sum_i (\vec{r}_i \times \vec{p}_i) = \sum_i m_i(\vec{r}_i \times \vec{v}_i)$$

where $\vec{r}_i$ are molecular centres.

The angular momentum due to the rotation of molecules about their molecular centres is defined as,

$$\vec{L}_r = I\sum_i \vec{\omega}_i$$

where I is the principal moment of inertia and $\vec{\omega}_i$ is the angular velocity of the i-th molecule.

Total angular momentum due to the motions of molecular positions, $\vec{r}_i$, and rotations of every molecule can be written as,

$$\vec{L} = \vec{L}_t + \vec{L}_r = \sum_i m_i(\vec{r}_i \times \vec{v}_i) + I\sum_i \vec{\omega}_i \ .$$

If we let $\vec{\omega}$ be the angular velocity of the molecular cluster and I_i the inertia tensor for a molecule, then

$$\vec{\omega} = I_i^{-1}\vec{L} \ .$$

Here we only wish to zero angular momentum by altering $\vec{v_i}$. If we let $\delta\vec{v_i}$ be translational velocities causing rotational motion of the cluster, it is then calculated from the angular velocity $\vec{\omega}$ as,

$$\delta\vec{v_i} = \vec{\omega} \times \vec{r_i}$$

and therefore the angular momentum can be removed by subtracting $\delta\vec{v_i}$ from $\vec{v_i}$

$$\vec{v_i'} = \vec{v_i} - \delta\vec{v_i} = \vec{v_i} - \vec{\omega} \times \vec{r_i} \ .$$

where $\vec{v_i'}$ is the corrected velocities.

2.10 Analysis

2.10.1 Radial Distribution Function

The radial distribution function(RDF), $g(r)$, is a well known function in measuring the local structure of dense liquids. It is proportional to the probability of finding a pair of atoms separated by distance between r and $r + \delta r$. $g(r)$ is defined for a system of N atoms as,

$$g(r) = \sum_{i=1}^{N} \frac{n_i(r, r+\delta r)}{V(r, r+\delta r)}$$

where $n_i(r, r+\delta r)$ is the number of atoms in the radial shell between r and $r+\delta r$ from atom i and $V(r, r+\delta r) = \frac{4}{3}\pi\left[(r+\delta r)^3 - r^3\right]$ is the volume of the radial shell. In this simulation, a resolution δr is chosen as 0.1Å.

2.10.2 Equal Area Projection

For a symmetric molecule, all atomic sites, $\vec{u_i}$, about the molecular centre can be projected from the molecular centre on to a unit sphere as,

$$\hat{u_i} = \vec{u_i}/|\vec{u_i}|$$

where $\hat{u_i}$ are projected atomic sites on the unit sphere.

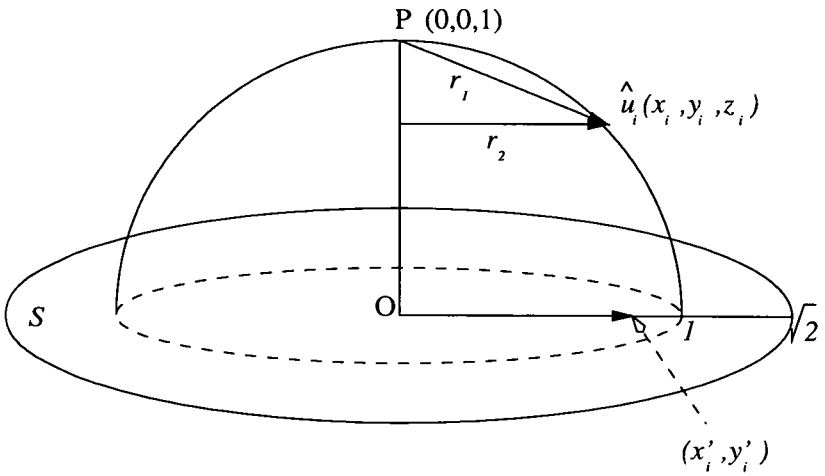

These points on a three-dimensional sphere can be represented on a two-dimensional plane, S, by using **the Lambert equal area projection**, which we call a dotplot.

The upper hemisphere of the unit sphere can be used to represent orientational order of a molecule. If we let **P** be the **north pole** and $\hat{u}$ any point on the unit sphere, the vector, $\vec{r_1}$, between the north pole and $\hat{u}$ can be projected on the plane, S, as a vector, (x', y') of the same length. Therefore the projected coordinates, $(x', y'i)$ are,

$$r_1{}^2 = x^2 + y^2 + (1 - z)^2$$

$$r_2{}^2 = x^2 + y^2$$

$$(x', y') = (x, y) \times (|\vec{r_1}|/|\vec{r_2}|)$$

where $|\vec{r_2}|$ is the distance from the z-axis.

Since the farthest distance from the north pole on the upperhemisphere of the unit sphere is $\sqrt{2}$ at equator, the area of the hemisphere being projected onto the plane is equal to the area of the projected plane. It can be proven that an area on the hemisphere is equal to the corresponding area projected on the plane.

2.10.3 Great-Circle angles

Angles between pairs of dense points on dot-plots can be found by measuring along common great circles. Figure 2.3 shows the common great circles divided in 10°.

The common great circles can be drawn on the two dimensional plane by projecting all cartesian coordinates of regular angles of a unit hemisphere, $Z \geq 0$, having a pole on (0,1,0) as in the figure 2.2. Coordinates of mesh points(x, y, z) are written in terms of angles,

$$\begin{aligned} x &= \sin\theta\cos\phi \\ y &= \cos\theta \\ z &= \sin\theta\sin\phi \end{aligned}$$

where coordinates and angles θ and ϕ are given in the figure.

All mesh points are then projected on $x - y$ plane by equal area projection method as follow,

$$(x', y') = \sqrt{\frac{2-2z}{x^2+y^2}}(x, y)$$

By using discrete angles $\Delta\theta$ and $\Delta\phi$, one could draw common great circles.

2.10.4 Pair Distribution Function

Translational ordering can be identified by projecting vectors between centres of neighbouring molecules on a unit sphere. These projected points indicate in which directions neighbouring molecule centres are placed. By taking advantage of the equal area projection explained in previous section, these points are then projected on the equatorial plane. The directions of neighbouring molecules projected on a unit sphere are given as,

$$\vec{u}_{ij} = \vec{r}_j - \vec{r}_i$$

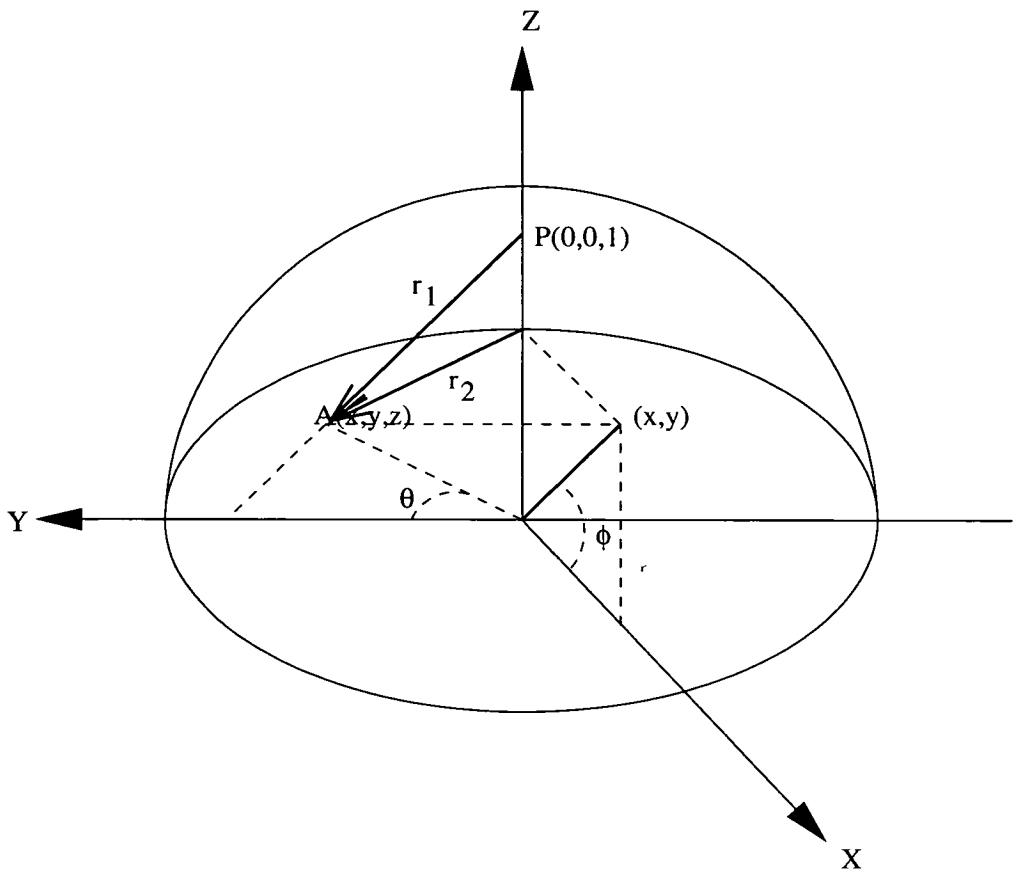

Figure 2.2:

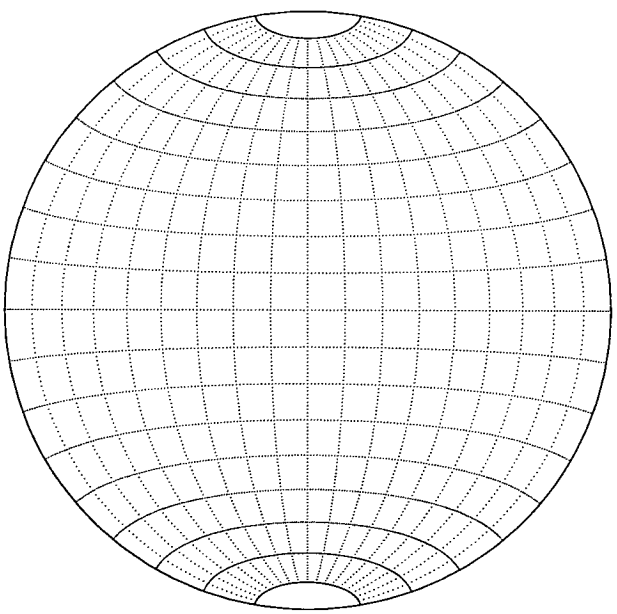

Figure 2.3:

$$\hat{u}_{ij} = \vec{u}_{ij}/|\vec{u}_{ij}|$$

where $\vec{r}_i$ and $\vec{r}_j$ are the coordinates of atomic positions, and j is the index of neighbours within a certain radial distance, and $\hat{u}_{ij}$ are the directional points of neighbouring atoms on the unit sphere centred on atom i.

The figure 2.4 is an example of the bcc crystalline phase showing the nearest neighbours and the next nearest neighbours.

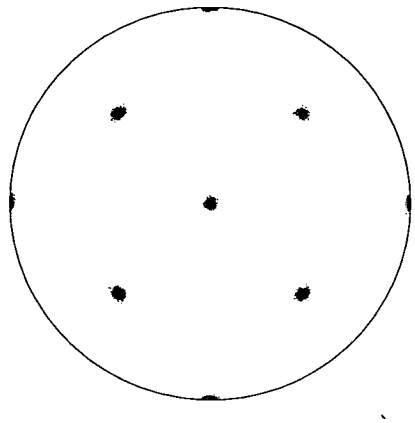

Figure 2.4: BCC crystalline phase

Chapter 3

Cluster Breathing Motion

3.1 Introduction

The essential feature for the phase transitions of condensed matter systems is the anharmonicity of thermal vibrational motion. We model a system with the Lennard-Jones inter-atomic potential. The potential is known as that the negative and the positive stresses are different and such properties are classified as anhamonicity.

As the amplitude of vibration increases, the anharmonicity of atomic vibration becomes much larger and may lead to structural transformation. In fact, the vibrational motion itself can be used as a means to investigate this phenomenon.

Vibrational motion has been studied by various methods on clusters such as normal mode analysis [38], molecular dynamics simulations [39] with the help of the velocity autocorrelation function, and the self-consistent phonon method [40] in theory. The phonons of bulk solid material are experimentally well studied by neutron inelastic scattering, far-infrared and Raman spectroscopy. For clusters, experimental results have been found from vibrational excitation of argon clusters in collisions with helium atoms [38].

In the present work, it is hoped to find a signal by which structural transition to a new phase can be identified by studying an artificially induced breathing motion of clusters. It is, however, by no means real but can be realised in the computer. Hence, it can be further utilised in various computer simulation study.

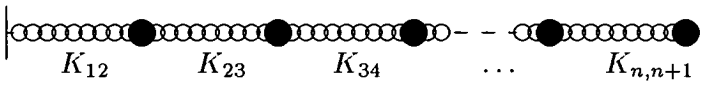

Figure 3.1: 1-dimensional coupled oscillator with one end fixed.

3.2 Mathematical Analysis

3.2.1 2-dimensional simplified disk with additions of new rings

It is essential in the MD simulations that all clusters taken to be studied must be equilibrated to a certain temperature in order either to make the clusters stable or to initialise them into certain states that we want. It is important to consider how the sizes of clusters are related to their vibration and what the equilibration sequences might be in MD simulations. In order to find the relation between the frequency of decay oscillation and the extra addition of atoms, we can conceive the 2-dimensional cluster as a disk. Suppose a disk is divided into several rings which have the same area. The circles dividing each ring have radius r_i for i-th disk.

One then makes the following equations. The innermost area in the disk is πr_1^2 for r_1, and the area of second ring is πr_1^2 because each ring has the same area. Therefore, $\pi {r_2}^2 = 2\pi {r_1}^2$. Consequently, $r_2 = \sqrt{2}r_1$, $r_3 = \sqrt{3}r_1$, and $r_4 = \sqrt{4}r_1$, and so on. If $r_1 = 1$, then $r_2 = \sqrt{2}$, $r_3 = \sqrt{3}$,... $r_n = \sqrt{n}$. This two-dimensional disk can be considered as the one-dimensional coupled oscillator as shown in figure 3.1 in which all masses are same because equal area makes equal masses ideally. The spring constants are increased by the factor of $\sqrt{n}$ of K for n-th spring which is made previously by supposing the circumference of ring to be the main factor of elasticity. The coupled oscillator is then formed to have one fixed point and other chained masses by springs. Thus, the configuration of the coupled oscillator is drawn above.

Spring constants $k_{12}, k_{23}, ..., k_{n,n+1} = K, \sqrt{2}K, \sqrt{3}K, ..., \sqrt{n}K$

For obtaining the eigenfrequencies of the coupled oscillator, one must solve the $2n$-th order equations which are known as the eigenvalue problem, n is the number of chained masses.

Let us consider a mass linked by a spring having spring constant K to the fixed point. This mass can move by x_1. Thus, the equation is

$$\begin{aligned} m\ddot{x}_1 &= -Kx_1 \quad , \\ -m\omega^2 x_1 &= -Kx_1 \quad , \\ \omega_0^2 &= \frac{K}{m} \quad . \end{aligned}$$

For two masses, the equations are written as,

$$\begin{aligned} m\ddot{x}_1 &= -Kx_1 - \sqrt{2}K(x_1 - x_2) \quad , \\ m\ddot{x}_2 &= -\sqrt{2}K(x_2 - x_1) \quad , \\ -m\omega^2 x_1 &= -K(1+\sqrt{2})x_1 + \sqrt{2}Kx_2 \quad , \\ -m\omega^2 x_2 &= +\sqrt{2}Kx_1 - \sqrt{2}Kx_2 \quad . \end{aligned}$$

This can be extended to n-th order equations as follows.

$$\begin{aligned} m\ddot{x}_1 &= -Kx_1 - \sqrt{2}K(x_1 - x_2) \quad , \\ m\ddot{x}_2 &= -\sqrt{2}K(x_2 - x_1) - \sqrt{3}K(x_2 - x_3) \quad , \\ &\vdots \quad , \\ m\ddot{x}_{n-1} &= -\sqrt{n-1}K(x_{n-1} - x_{n-2}) - \sqrt{n}K(x_{n-1} - x_n) \quad , \\ m\ddot{x}_n &= -\sqrt{n}K(x_n - x_{n-1}) \quad , \end{aligned}$$

and

$$\begin{aligned} -m\omega^2 x_1 &= -K(1+\sqrt{2})x_1 + \sqrt{2}Kx_2 \quad , \\ -m\omega^2 x_2 &= \sqrt{2}Kx_1 - (\sqrt{2}+\sqrt{3})Kx_2 + \sqrt{3}Kx_3 \quad , \\ &\vdots \end{aligned}$$

$$
\begin{aligned}
-m\omega^2 x_{n-1} &= \sqrt{n-1}Kx_{n-2} - (\sqrt{n-1}+\sqrt{n})Kx_{n-1} + \sqrt{n}Kx_n \quad , \\
-m\omega^2 x_n &= \sqrt{n}Kx_{n-1} - \sqrt{n}Kx_n \quad .
\end{aligned}
$$

It is rewritten to matrix form to compute eigenvalues and eigenvectors.

$$
\mathbf{A} = \begin{pmatrix}
\frac{(1+\sqrt{2})K}{m} & \frac{-\sqrt{2}K}{m} & \cdots & 0 & 0 \\
\frac{-\sqrt{2}K}{m} & \frac{(\sqrt{2}+\sqrt{3})K}{m} & \cdots & 0 & 0 \\
\vdots & \vdots & \ddots & \frac{-\sqrt{n-1}K}{m} & 0 \\
0 & 0 & \frac{-\sqrt{n-1}K}{m} & \frac{(\sqrt{n-1}+\sqrt{n})K}{m} & \frac{-\sqrt{n}K}{m} \\
0 & 0 & 0 & \frac{-\sqrt{n}K}{m} & \frac{\sqrt{n}K}{m}
\end{pmatrix}
$$

$$
|\mathbf{A} - \omega^2 \mathbf{1}| = 0, \tag{3.1}
$$

$$
(\mathbf{A} - \omega^2 \mathbf{1})|x_i\rangle = 0. \tag{3.2}
$$

From equations 3.1 and 3.2, we can then obtain the secular equations, and consequently eigenvalues and eigenvectors as well by solving that equations .

$$
\begin{vmatrix}
\frac{(1+\sqrt{2})K}{m} - \omega^2 & \frac{-\sqrt{2}K}{m} & \cdots & 0 & 0 \\
\frac{-\sqrt{2}K}{m} & \frac{(\sqrt{2}+\sqrt{3})K}{m} - \omega^2 & \cdots & 0 & 0 \\
\vdots & \vdots & \ddots & \frac{-\sqrt{n-1}K}{m} & 0 \\
0 & 0 & \frac{-\sqrt{n-1}K}{m} & \frac{(\sqrt{n-1}+\sqrt{n})K}{m} - \omega^2 & \frac{-\sqrt{n}K}{m} \\
0 & 0 & 0 & \frac{-\sqrt{n}K}{m} & \frac{\sqrt{n}K}{m} - \omega^2
\end{vmatrix} = 0
$$

Because this matrix is a real, symmetric, tridiagonal matrix, both eigenvalues and eigenvectors can be easily computed by QL algorithm which calculates *the Lower triangular* of the tridiagonal matrix which must be prepared to that form before the calculation. However, it does not need to change its matrix form because the equation already has tridiagonal matrix form. For the two-mass problem, the secular equations are

$$
\begin{vmatrix}
\frac{(1+\sqrt{2})K}{m} - \omega^2 & \frac{-\sqrt{2}K}{m} \\
\frac{-\sqrt{2}K}{m} & \frac{\sqrt{2}K}{m} - \omega^2
\end{vmatrix} = 0 \quad .
$$

We then have the equation;

$$\omega^4 - \frac{(1+2\sqrt{2})K}{m}\omega^2 + \frac{\sqrt{2}K^2}{m^2} = 0 \quad .$$

Thus, the eigenfrequencies are,

$$\omega_1 = \sqrt{2+\sqrt{2}}\sqrt{\frac{K}{m}} \quad ,$$

$$\omega_2 = \sqrt{-1+\sqrt{2}}\sqrt{\frac{K}{m}} \quad .$$

If we put these two frequencies into equation 3.2, we then know that ω_1 is the mode that two masses are moving in opposite direction (anti-parallel) and ω_2 is the mode that two masses are moving in same direction - parallel. These frequencies can be compared as followed.

$$\omega_1 > \omega_0 = \sqrt{\frac{K}{m}} > \omega_2 \quad ,$$

where ω_0 is the frequency of the single mass problem. The eigenvalues which are solved by computation can be seen in figure 3.2.

3.2.2 3-dimensional sphere with additions of new shells

The 2-dimensional case can be simply transformed to the 3-dimensional case by changing the factor of spring constant from square root to cube root because, from the same idea as the 2-dimensional case, the volume of the first shell is $(4/3)\pi r_1^3$ and the equation, $(4/3)\pi r_2^3 = 2.0 \times (4/3)\pi r_1^3$ is satisfied due to the fact that each shell has same volume. Hence, if $r_1 = 1$, $r_2 = \sqrt[3]{2}$, $r_3 = \sqrt[3]{3}$, etc. In this case, the main factor of elasticity is interfacial surface between two shells.

Therefore, the secular equation of the 3-dimensional case is obtained as followes.

$$\begin{vmatrix} \frac{(1+\sqrt[3]{2})K}{m} - \omega^2 & \frac{-\sqrt[3]{2}K}{m} & \cdots & 0 & 0 \\ \frac{-\sqrt[3]{K}}{m} & \frac{(\sqrt[3]{2}+\sqrt[3]{3})K}{m} - \omega^2 & \cdots & 0 & 0 \\ \vdots & \vdots & \ddots & \frac{-\sqrt[3]{n-1}K}{m} & 0 \\ 0 & 0 & \frac{-\sqrt[3]{n-1}K}{m} & \frac{(\sqrt[3]{n-1}+\sqrt[3]{n})K}{m} - \omega^2 & \frac{-\sqrt[3]{n}K}{m} \\ 0 & 0 & 0 & \frac{-\sqrt[3]{n}K}{m} & \frac{\sqrt[3]{n}K}{m} - \omega^2 \end{vmatrix} = 0 \quad .$$

From the computation of the eigenvalue equation, the eigenfrequencies of the 3-dimensional case are rather lower than 2-dimensional case. From figure 3.2, one can see that when the more shells are added to the cluster, the lowest frequency goes to zero which means that the cluster only can move very slowly.

3.2.3 3-dimensional sphere divided by a different number of shells

Two previous analyses are for the different size which is increased by adding either new rings or shells. However, in this study, it is insisted first that the analysis for the same size of clusters and different numbers of shells should be done for this simulation studied.

The eigen frequencies are obtained by dividing all spring constants by cube root of n because this should be done for same cluster. Therefore, the secular equation for the same cluster is written as,

$$\begin{vmatrix} \frac{(1+\sqrt[3]{2})K}{\sqrt[3]{nm}} - \omega^2 & \frac{-\sqrt[3]{2}K}{\sqrt[3]{nm}} & \cdots & 0 & 0 \\ \frac{-\sqrt[3]{K}}{\sqrt[3]{nm}} & \frac{(\sqrt[3]{2}+\sqrt[3]{3})K}{\sqrt[3]{nm}} - \omega^2 & \cdots & 0 & 0 \\ \vdots & \vdots & \ddots & \frac{-\sqrt[3]{n-1}K}{\sqrt[3]{nm}} & 0 \\ 0 & 0 & \frac{-\sqrt[3]{n-1}K}{\sqrt[3]{nm}} & \frac{(\sqrt[3]{n-1}+\sqrt[3]{n})K}{\sqrt[3]{nm}} - \omega^2 & \frac{-\sqrt[3]{n}K}{\sqrt[3]{nm}} \\ 0 & 0 & 0 & \frac{-\sqrt[3]{n}K}{\sqrt[3]{nm}} & \frac{\sqrt[3]{n}K}{\sqrt[3]{nm}} - \omega^2 \end{vmatrix} = 0 \quad .$$

The eigenvalues given in figure 3.3 show that the lowest frequency gradually approaches to zero as the number of shells (rings) increases, which is similar to figure 3.2. However, the highest frequency in the figure approaches 2.0 rather than increases continuously suggesting a limit for the highest frequency.

3.2.4 Triggered Breathing Motion

In a cluster, a breathing vibration motion (s-wave) of the cluster is radial motion from its centre of mass. This can be induced by systematically changing the motion of atoms in a cluster by adding radial velocities to each atom proportional to its distance from

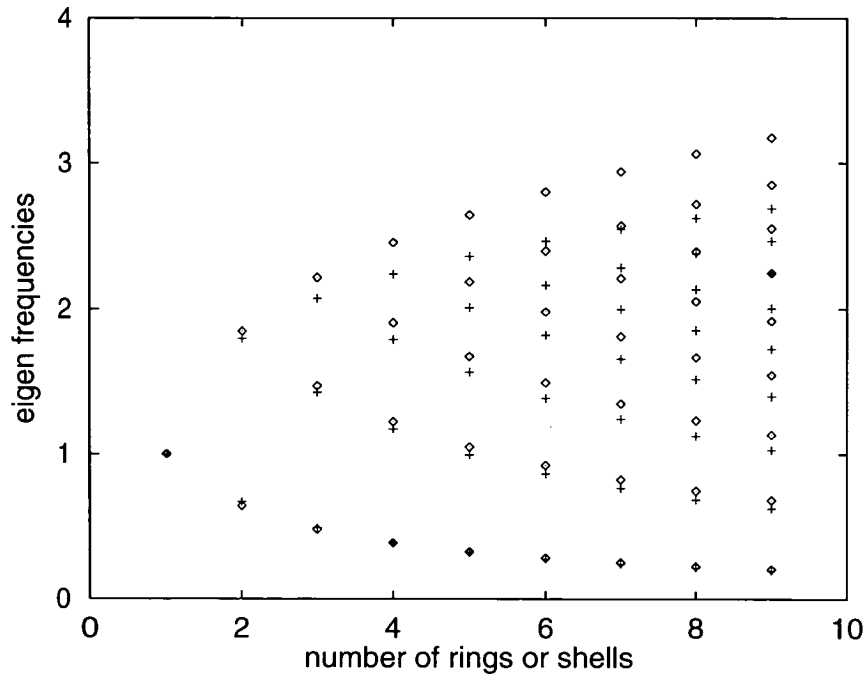

Figure 3.2: Eigen frequencies for 2-D disk (diamond) and for 3-D sphere (cross) as the system size increases by adding new rings or shells.

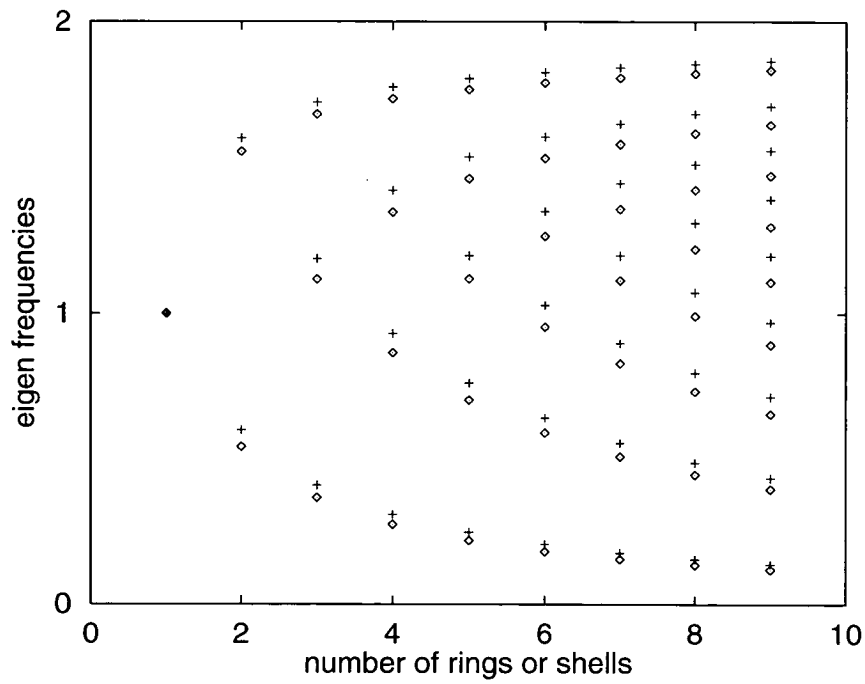

Figure 3.3: Eigen frequencies for 2-D disk (diamond) and for 3-D sphere (cross) as the number of rings or shells increases whereas the size of the sphere does not change.

the centre of mass. Having added radial velocities, each atom of the cluster will have additional radial motion from the centre of mass of the cluster.

If we let $\vec{u}_i$ be the velocities before the change and $\vec{v}_i$ be the velocities after the change, then $\vec{v}_i$ is written with an added radial term

$$\vec{v}_i = \vec{u}_i + \alpha \vec{r}_i$$

where $\vec{r}_i$ is the position of i-th atom from the centre of mass. Here α has the unit of $(\text{time})^{-1}$ and defines the proportion of the additional radial term. A large α value will cause a large radial motion. If we wish to have radial velocities consistent with a certain temperature T_r, then

$$\alpha = \frac{1}{|\vec{r}|}\sqrt{\frac{3k_B T_r}{m}}$$

where k_B is the Boltzmann constant and m is the mass of an atom. In this study α is calculated for a unit vector $|\vec{r}| = 1\text{Å}$ and $T_r = 5\text{K}$.

It is important that the kinetic energy must remain constant after the induction of s-wave motion which alters temperature since our interest is to study the breathing motion decay at a defined temperature. The kinetic energy can be kept constant by conserving $\sum_{i=1}^{N} v_i^2$. There will be no change in the potential energy since the positions of the atoms are not changed.

The conservation of the kinetic energy can be made by adjusting $\vec{v}_i$ by β, giving final velocities $\vec{v'}_i$,

$$\vec{v'}_i = \sqrt{\beta}\vec{v}_i,$$

$$\beta = \frac{\sum_{i=1}^{N} m_i u_i^2}{\sum_{i=1}^{N} m_i v_i^2}$$

where m_i is the mass of i-th atom.

Table 3.1: Lattice parameter† and atomic mass‡

element	lattice parameter at 4K	atomic mass unit (a.m.u)
Argon	5.31 Å	39.948
Krypton	5.64 Å	83.80

Table 3.2: Parameters for Lennard-Jones potential

interaction	A (Kcal/moleÅ^6)	B (Kcal/moleÅ^{12})
Kr-Kr	2937.00	6393405.0
Kr-Ar§	2366.01	4222192.2
Ar-Ar	1906.03	2788327.8

† *C. Kittel chapter 1* [42].
‡ *The physics quick reference guide* [43].
§ *The geometric mean of the A and B parameters is taken for the interaction of krypton and argon, e.g.* $A_{KrAr} = \sqrt{A_{Kr}A_{Ar}}$.

3.3 Simulation Detail

A cluster of a mixture of 136 Krypton and 136 Argon atoms [41]is initiated with lattice parameters at the temperature of 4K as given in the table 3.1 and a random velocity distribution. Parameters for Lennard-Jones potential function are given in table 3.2. The system is equilibrated at the same temperature and then again at 10K. The heating and cooling processes between 10K and 100K are then followed with temperature steps of 5K. In each step, the cluster is allowed to equilibrate for 200ps. A simulation time step of 0.005ps is chosen for this work. After the equilibration at each temperature step, the cluster will be triggered to induce a breathing motion and then allowed to equilibrate for 50ps while investigating the decay of this oscillation.

3.4 Analysis

Once a cluster has been triggered to induce s-wave, the wave will eventually disappear as equilibrium is reached. In such decay oscillations, decay parameters can be obtained and compared as a function of temperature to study structural transformation of a cluster through the variation of the anharmonicity.

Since breathing motion will not be purely homogeneous in every radial direction,

an arithmetic average of three principal moments of inertia I_{xx}, I_{yy}, and I_{zz} which are direct observables during simulations will give a reasonable approximation to the oscillation of s-wave,

$$\langle I \rangle = (I_{xx} + I_{yy} + I_{zz})/3.$$

If we sample peak points at crests of the oscillation of $\langle I \rangle$ as a function of time t and let the points be $\langle I(t) \rangle$, the decay oscillation can be fitted to an exponential function

$$\langle I(t) \rangle = e^{-\tau t}$$

where τ is the decay parameter, the larger the decay parameter τ the more rapidly decaying the oscillation.

s-wave oscillation will be analysed by the fourier transformation(FT) to study the normal mode frequency.

3.5 Results

3.5.1 Decay Oscillation

From the decay oscillation of triggered breathing motion, typical oscillations are given in figures 3.4, 3.5, and 3.6. A system of a cluster is prepared at 10K being perfectly ordered as a CsCl structure (figure 3.4) which is then heated to 100K by 5K step and equilibrated at 100K having the liquid phase (figure 3.5). It is then cooled and equilibrated at 10K being a solid phase (figure 3.6). Figure 3.4 of a perfectly ordered solid phase cluster clearly exhibits a long-lasting normal mode oscillation about $< I >$=1.2×10^{6}amuÅ^2 after breathing motion has been induced. Figure 3.6 of a solid phase (imperfect crystal), which is cooled from a liquid at 100K to 10K, shows immediate decay of the normal mode oscillation lasted about 10ps. It should be noted that two solid phases, 3.4 and 3.6, are clearly distinguished by the decay oscillation suggesting that they have different lifetime. Figure 3.5 is a typical decay oscillation of liquid cluster. Decay oscillation of the liquid seems no different compared to the solid, cooled from the liquid. The

differences between the solid phase (figure 3.6) after the cooling and the liquid phase (figure 3.5) can be found in fluctuation tails and average moments of inertia. The liquid phase shows an unstable fluctuating tail with a short lifetime as well as a large average moment of inertia whereas the average moment of inertia of the solid phase is comparable to that of the perfectly ordered solid (figure 3.4). It should be noted that the moment of inertia of the solid after the cooling is lower than that of the perfectly ordered solid phase. It seems to suggest that the solid is more sphere-like in shape than the perfectly ordered solid.

Decay parameters τ obtained from every 5K of temperature steps are drawn as a function of temperature as seen in figure 3.7 for heating of a Krypton-Argon cluster from a perfect CsCl crystal phase at the temperature of 10K until 100K.

Before the transition, the decay oscillations in phase **A** of figure 3.7 have the form of figure 3.4. Increase of temperature in phase **A** causes gradual changes of the decay parameter, shortening the decay time. When the cluster is heated above 80K, the decay parameter τ increases significantly compared to the changes in phase **A**. The oscillations for the phase **B** have the form of figure 3.5, showing that they do not last for long. The structural formations of the two phases **A** and **B** can be identified by dotplots (refer to section 2.10) which are drawn in figures 3.8 and 3.9, such that neighbour interatomic vectors within a range of 5 Å are taken to make dotplots.

Figure 3.8 shows a perfectly ordered CsCl structure before heating whereas figure 3.9 shows no order in the arrangement of neighbouring atoms after melting. Four groups of dense dot regions represent four (111) directions for the nearest neighbour atoms in the upper hemisphere and four groups around the circumference and the centre group represent the next nearest neighbours. These are dotplots of the CsCl structure.

After the equilibration at the temperature of 100K for 250ps, the krypton argon mixture is now cooled down to 10K. The T-τ figure for the cooling process is given in figure 3.10. This shows indication of crystallisation at around 75K. However, it is less

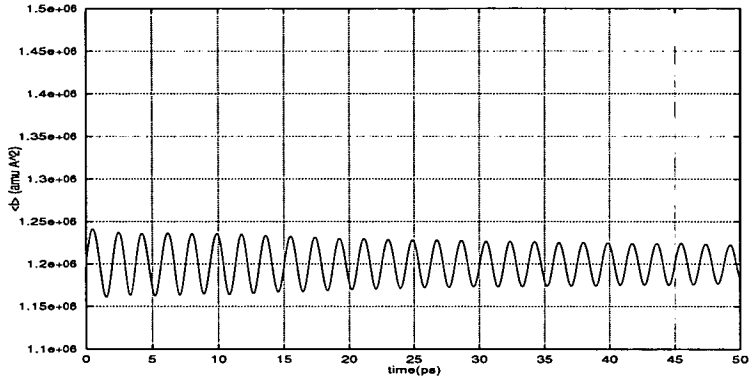

Figure 3.4: perfectly ordered solid at T=10K. $\langle I \rangle = (I_{xx} + I_{yy} + I_{zz})/3$.

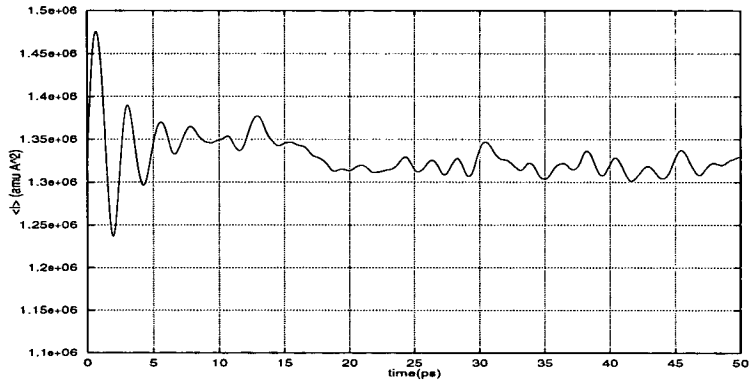

Figure 3.5: liquid at T=100K.

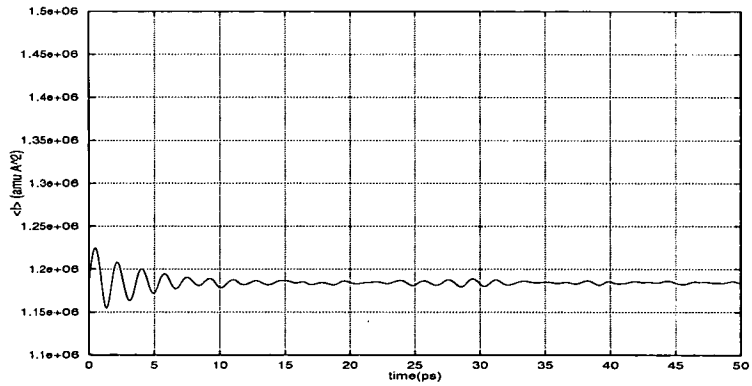

Figure 3.6: solid at T=10K (cooled from the liquid at 100K to 10K, then excited in s-wave).

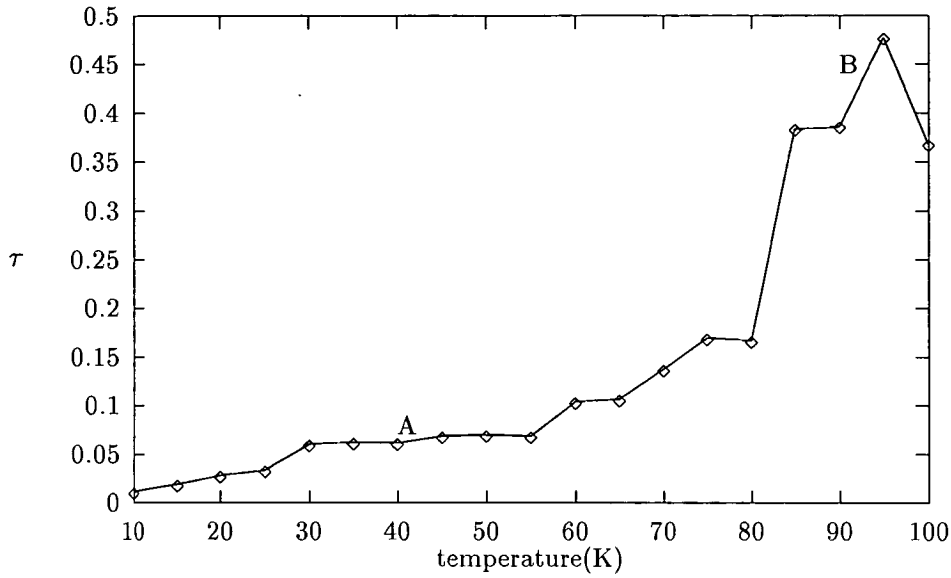

Figure 3.7: Decay parameter as a function of temperature in heating.

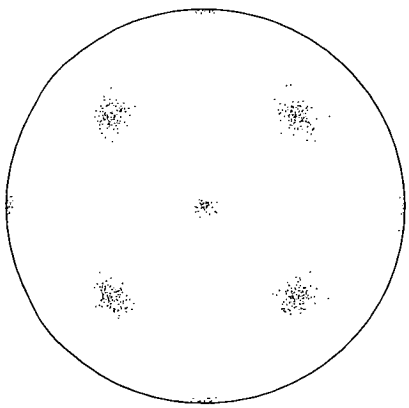

Figure 3.8: a perfectly ordered solid at T=10K before heating.

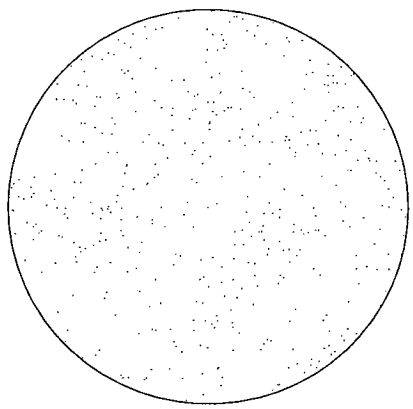

Figure 3.9: liquid at T=100K after melting.

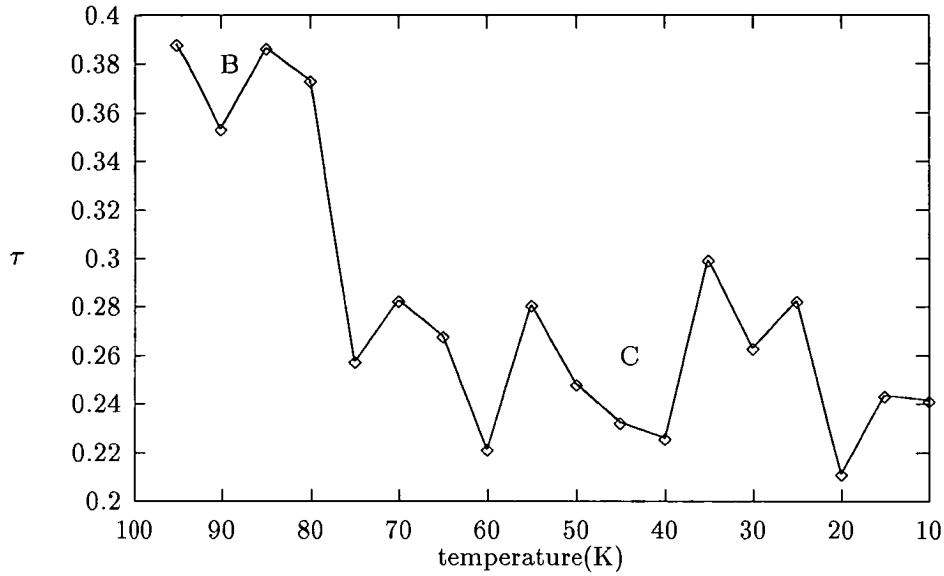

Figure 3.10: Decay parameter as a function of temperature in cooling.

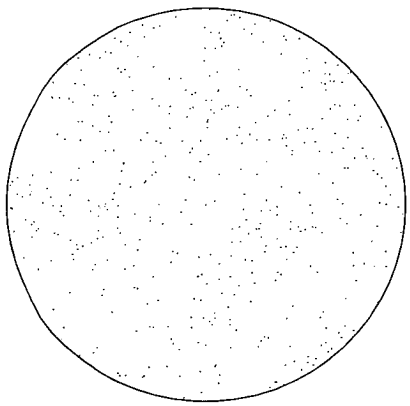

Figure 3.11: liquid at T=100K, phase **B**.

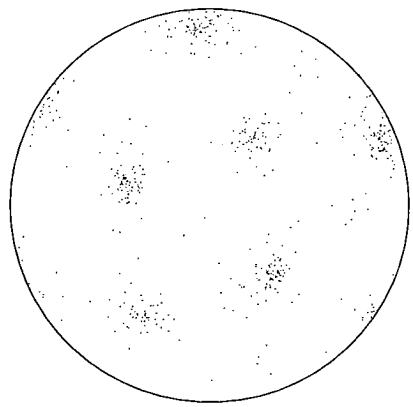

Figure 3.12: ordered solid at T=10K (cooled from 100K), phase **C**.

Figure 3.13: Spectral density changes as a function of temperature in heating from perfect single crystal to liquid. Each figure shows spectral densities at given frequencies (THz).

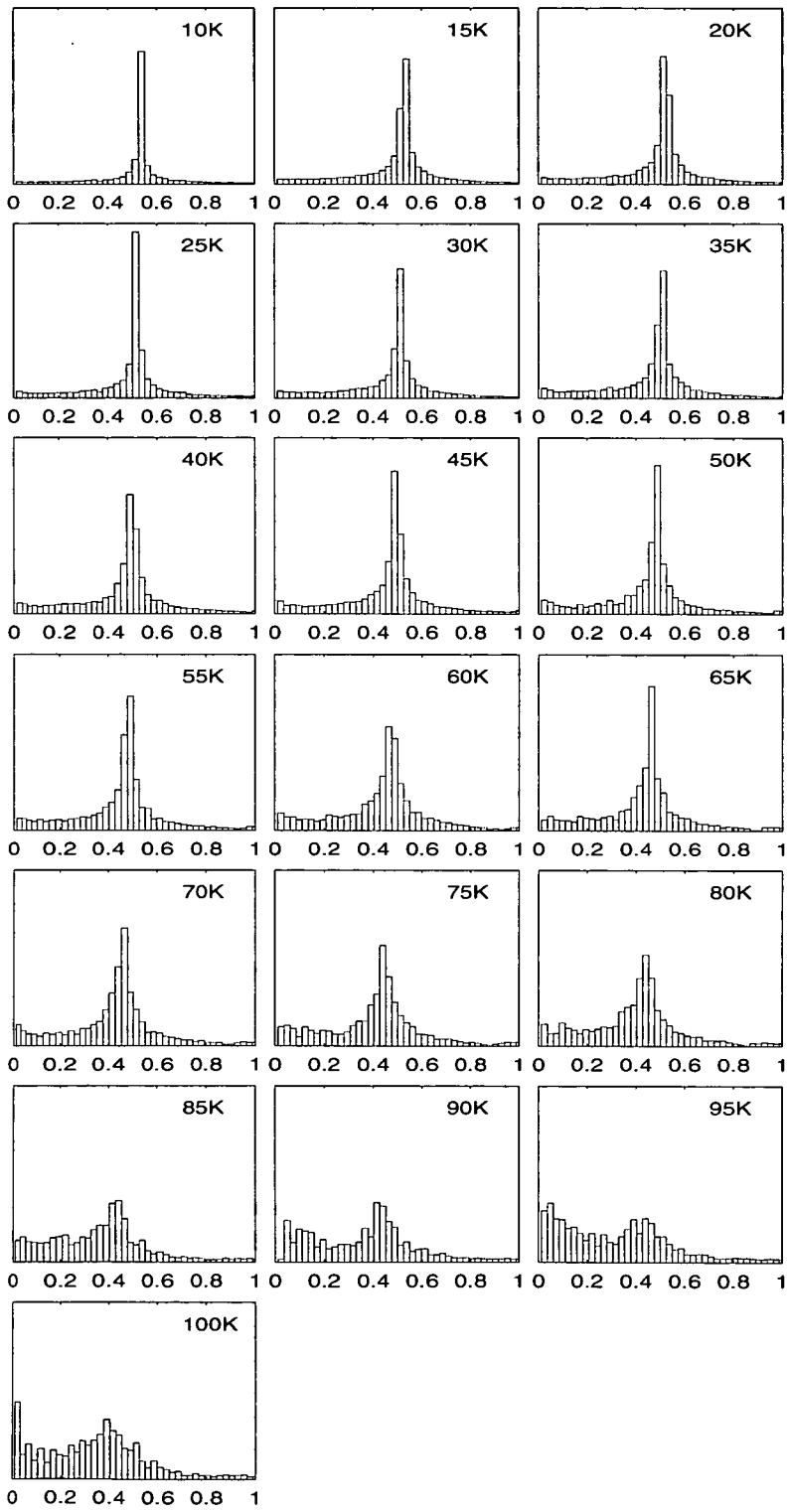

Figure 3.14: Spectral density changes as a function of temperature in cooling from liquid to crystal (imperfect).

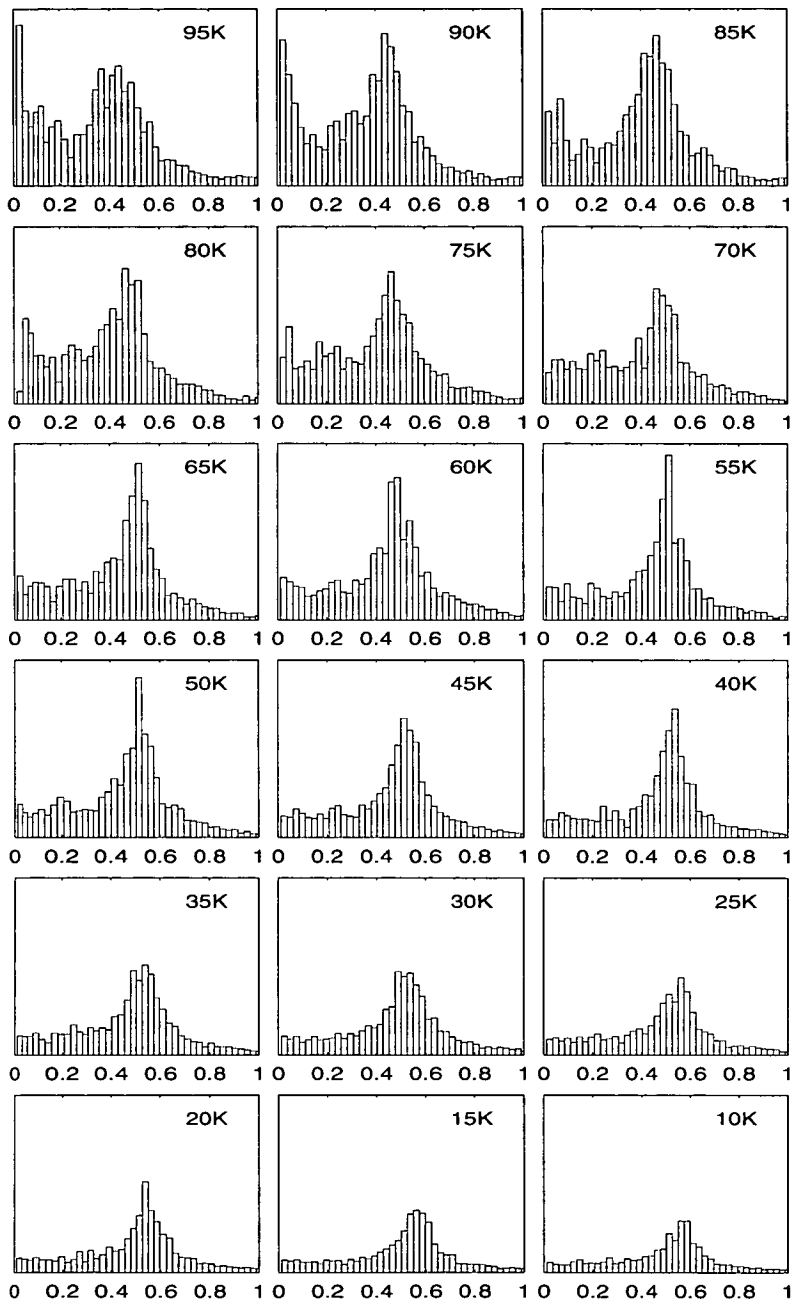

clear compared to the transition of the heating process. Dotplots of both **B** and **C** are shown in figures 3.11 and 3.12, and demonstrate that the cluster actually has formed a CsCl structure although it is not in a perfect order.

It should be noted from the comparison between figures 3.7 and 3.10 that decay parameters for both solid phases having the same CsCl structure, **A** and **C**, are quite different suggesting that the solid phase after cooling has not gone back to a perfect crystalline phase and has considerable defects. Since the oscillatory motions in phase **A** (figure 3.8) and **C** (figure 3.12) are different although their structural information seen by dotplots show no significant difference, it may suggest that there exist structural defects - occupations of argon atoms (or krypton) at the positions of krypton atoms (or argon) - in the cluster in phase **C**. Such defects are assumed to be involved with the feature of s-wave. Therefore, τ values from such oscillatory motions may be used as an indicator for crystal defects.

Fourier Transformation (FT) analysis is made for s-wave oscillations to examine changes in normal mode frequencies. Spectral density changes against temperature are drawn in figures 3.13 and 3.14 for heating and cooling respectively. For heating, spectral density figures are arranged in two columns in figure 3.13 where temperature increases by 5K from 10K to 100K for which figures are drawn from the left to the right and from the top to the bottom. As temperature increases the major frequency has a distinctive spectral density change from a high frequency to a low frequency. From above 80K, there seems no particular frequency having a distinctive spectral density indicating that a transition has occurred. This result is consistent with the previous analysis of decay parameters showing a phase transition at around the temperature of 80K in heating. At 10K, the figure in frequency domain shows a high peak within a very limited frequency region. It is suggestive of a lifetime decrease of s-wave showing underdamping. In case of the figures over 80K, they show a broad increase over all frequencies under 0.4THz suggesting that the wave is highly damped. When the temperature reaches

100K, most frequencies under 0.4THz increase significantly. It is the evidence of an almost overdamping by which s-wave quickly dies away.

Spectral density figures of FT analysis of s-wave oscillations for cooling are shown in figure 3.14 where temperature decreases by 5K from 95K to 10K for which figures are drawn from the left to the right and from the top to the bottom. The figures of cooling show no noticeable change at any point although the figures of the highest and the lowest temperatures are different. It suggests that on cooling there are a lot of localised modes at low T which are not present in a single crystal. It is, however, noted that at low temperatures the majority of normal mode frequencies are in a rather confined region around 0.5THz whereas there is a broad range of normal mode frequencies in high temperatures. Such confined region of normal mode frequencies at low T in figure 3.14 is seen more clearly in figure 3.13 showing very sharp spectra. Unlike figure 3.13 no clear distinction between ordered phase and liquid phase is seen in figure 3.14.

3.6 Discussion

This study was initiated to search for a clear signal that can be got from a MD simulation when a cluster changes phase. The signal τ clearly identified the transition from the crystalline solid to the liquid. However, when the system was cooled, the signal of the transition from the liquid to the solid state is significantly influenced by lifetime reduction due to defects inside the system although the transition point was identified. On the contrary, such a lifetime reduction itself is a manifestation of having defects or disorders and, therefore, can be used to identify the presence of defects. It would be very valuable to use this method to investigate the two transitions in sulphurhexafluorides (SF_6), which are the subject of chapter 5 and 6. Its value is that no analysis of detailed structure is necessary. Unfortunately the fact that the lifetime is determined so strongly by the structural defects we cannot use this method to give an unequivocal indication of anharmonicity.

Chapter 4

Monatomic simulation

4.1 Introduction

In the early stage of a phase transition, the new phase begins with the formation of nuclei which grow into critical nuclei. As a critical nucleus is able to withstand thermal fluctuations, it can extend its new phase region further until the transition is completed. Growth of such nuclei is called nucleation. In experiment, identifying the formation of nuclei is quite subtle and techniques are in general involved with spectroscopies using various sources such as X-ray, neutron beam, and electron beam. Diffraction of such beams from samples gives structural information. What we see from the experiments are merely statistically averaged peaks which may not be a sensitive indicator to the formation of nuclei.

Even in computer simulation with all the given coordinates and momenta as a function of time, the subtlety still exists due to the fact that most functions used to identify structural changes are macroscopic. The formation of nuclei is precursory of phase transitions and takes place in finite positions throughout a system. Until nuclei grow to a certain size, it would be impossible to detect their early formation with functions only sensitive to the macroscopic changes.

In the first successful crystal nucleation in molecular dynamics in three dimensions by Mandell and co-workers [7] with bulk systems of 108, 256 and 500 Lennard-Jones particles, the crystalline phase was identified by investigating the apparent absence of

diffusion, the characteristic radial distribution function, and the structure factor. For more detailed study on local structures the Voronoi polyhedron method can be used [44]. This method identifies various polyhedra although it has problems when dealing with dynamical structures.

There has been research on five-fold symmetric structures of small clusters [45, 46, 47], such as the icosahedron and decahedron. It has been argued that these structures are favourable in small systems although system size criteria vary broadly from N $\sim$ 500 to 1600. Van de Waal found that the simulated electron diffraction pattern of a 3000-atom argon cluster having a multiply twinned decahedral structure was in excellent agreement with an earlier experimental result [48]. Although the cluster size is intermediate between the icosahedral and fcc crystalline regimes, the model did not show structural transition, and the multiply twinned core remained with dominant five-fold symmetry. It was suggested that gradual changes of diffraction patterns towards those of fcc could be explained by further growth of fcc crystalline phase upon the twinned core. Therefore, the effect of the core on the diffraction pattern would gradually disappear.

Our main interest in the present simulation study focuses on the formation of a new phase through the identification of nuclei. Since all the investigation in this chapter will be made by cluster simulations, results would not be compatible with those of bulk simulations. However, the nucleation process studied in cluster simulations can be understood in broad. In search for a local ordering, since spatial positions of neighbour atoms are very specific to its structural formation around an atom, angles between directions of neigbour atoms are a precise indicator of a local ordering. Therefore, we will be looking at cosine angles formed between neigbour atoms.

4.2 Simulation detail

A cluster of 300 krypton atoms is simulated. The Lennard-Jones pairwise additive potential is used since it well represents the interactions of inert gas atoms. The parameters for the krypton-krypton interaction are given in table 3.2 in chapter 3, where the physical characteristics of krypton are also listed in table 3.1. A perfect initial face-centered cubic lattice structure with random velocities corresponding to a temperature of 1K is prepared. The system is then equilibrated at that temperature until a steady average potential energy is obtained to confirm that the system is in equilibrium. After the equilibration at 1K, the system is slowly heated at a rate of 0.02K/ps to above the melting point (120K). In the process of the melting simulation, certain atoms in the cluster can evaporate at higher temperatures. To prevent atoms from escaping entirely, any atom going beyond a certain threshold distance from the centre of the cluster is redirected to the cluster's centre. A virtual sphere which is bounded by the threshold is chosen significantly larger than the cluster size expected in liquid phase, in order to avoid interference with the physical properties of the cluster during the simulation. In such a way, the applied pressure due to the virtual sphere is to be close to zero and will be the vapour pressure for the stable equilibrium of the cluster of the size chosen, but it is purely to retain the atoms. When the system has reached 120K, it is equilibrated again and its structural memory of the solid phase will be totally lost. After this equilibration, the system is cooled down to 1K at various cooling rates.

4.3 Analysis

A very straightforward method for defining the structure of a cluster undergoing a change of thermodynamic conditions is measuring the angles between neighbour atoms in the cluster and presenting the distribution of measured angles. Distributions of these angles can be direct measures of the formation of nuclei. We shall call this function the angle distribution function (ADF). It was used by Hsu and Rahman [9]

for identifying structures of bcc and fcc. We have extended it for various structures including hexagonal close-packed and five-fold symmetric structures. All configuration numbers counted to produce ADF is 13 (=1+12 for fcc, hcp and icosahedron, =1+10+2 for decahedron) atoms except for the bcc structure which is 15 (=1+8+6) atoms. In the radial distribution function (RDF – refer to section 2.10.1), there is a common broad gap between the peaks of neighbouring atoms and the rest. The minimum in the gap is used to identify neighbouring atoms with which ADF is produced. Although the gap in the liquid RDF is not as clear as in the solid, it still can be identified as the first minimum in the RDF, which is in between the first and the second peak. ADF has advantage over RDF in that it has a definite number of peaks whereas for RDF, it is indefinite.

Typical ADFs for various perfect structures are given in figure 4.1. They will be used as standard references in later studies. There are two five-fold symmetric structures (icosahedron, decahedron) included in the figure in addition to the three standard lattice structures; bcc, fcc, and hcp. The icosahedron consists of 13 atoms, one at its centre surrounded by 12 atoms giving 20 triangular faces, 30 edges, and 12 vertices. The decahedron consists of five tetrahedra sharing an edge of each tetrahedron resulting in a polyhedron with 7 vertices where atoms are placed, 10 triangular faces, and 15 edges. In order for five tetrahedra to fit together to form a decahedron, each of them has to distort slightly. The x-axis in figure 4.1 stands for cosine angles and the y-axis for counts of the cosine angles within $\pm\alpha/2$ where α is the chosen resolution ($\alpha \simeq 0.0385$ rad.). Each structure has its own definitive distribution which can be distinguished one from another. In the case of the body-centered cubic (bcc) structure, both the eight nearest and the six next-nearest neighbours are included in the angle distribution. Possible angles(cosines) involving the nearest neighbours in bcc are 70.7°(0.33) and 109.5°(-0.33), involving the next-nearest neighbours 90°(0.0) and 180°(-1.0), and involving the nearest neighbours and the next-nearest neighbours 54.7°(0.58) and 125.3°(-0.58). In the

face-centered cubic (fcc) structure, each atom is surrounded by 12 nearest neighbours and possible angles(cosines) involving the neighbours are 60°(0.5), 90°(0.0), 120°(-0.5), and 180°(-1.0). The coordination number of the hexagonal close-packed (hcp) is 12, the same as for fcc. However, it has two more possible angles, 109°(-0.33) and 146°(-0.83) than fcc. The icosahedron has two possible angles at 63.6°(0.44) and 116.4°(-0.44). In the case of the decahedron, which has 12 nearest neighbours, all the possible angles of the nearest neighbours about its centre are the same as those found in hcp except for 113°(-0.39) in the decahedron and 109.5°(-0.33) in hcp. The angles are not all equally numerous, but this is taken into account in figure 4.1.

4.4 Results

In figures 4.2 and 4.3, continuous ADFs are represented as plots which vary with temperature for heating and cooling of a cluster at a rate of 0.0025K/ps. In order to examine the cluster in various parts, it is divided into three (core, mid-shell, and surface) having the same number of atoms counted from its centre. ADFs of the core, the mid-shell, and the surface are represented from the top to the bottom in both figures. The continuous ADF in temperature change of the two figures for heating and cooling clearly show structural transitions, and does identify the point of transition either from or to the crystalline phase.

In heating, the phase of the cluster started at the lowest temperature with a perfect fcc crystalline phase with random thermal velocities being in equilibrium at that temperature. As the temperature rises all the three peaks of the fcc angles broaden showing increasing thermal motion as seen in figure 4.2. Above 80K where phase transition to the liquid occurs, all the peaks become diffuse with no particularly favoured angles although there seem to exist very broad humps around 53°(0.6), 107°(-0.3), and 180°(-1.0). The peak around 60°(0.5) being the tetrahedral angle moves towards a lower angle 53°(0.6) and two peaks of fcc at 90° and 120° become as one at 107°(-

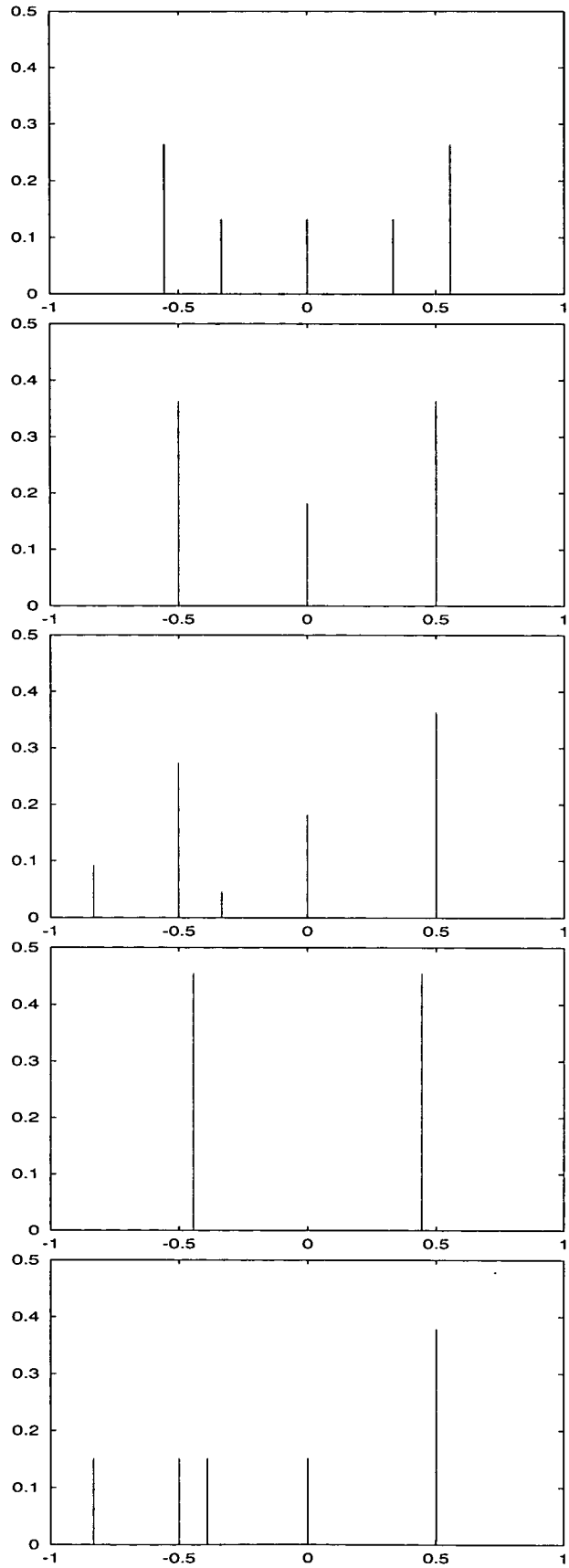

Figure 4.1: ADFs in order of bcc, fcc, hcp, icosahedron, and decahedron

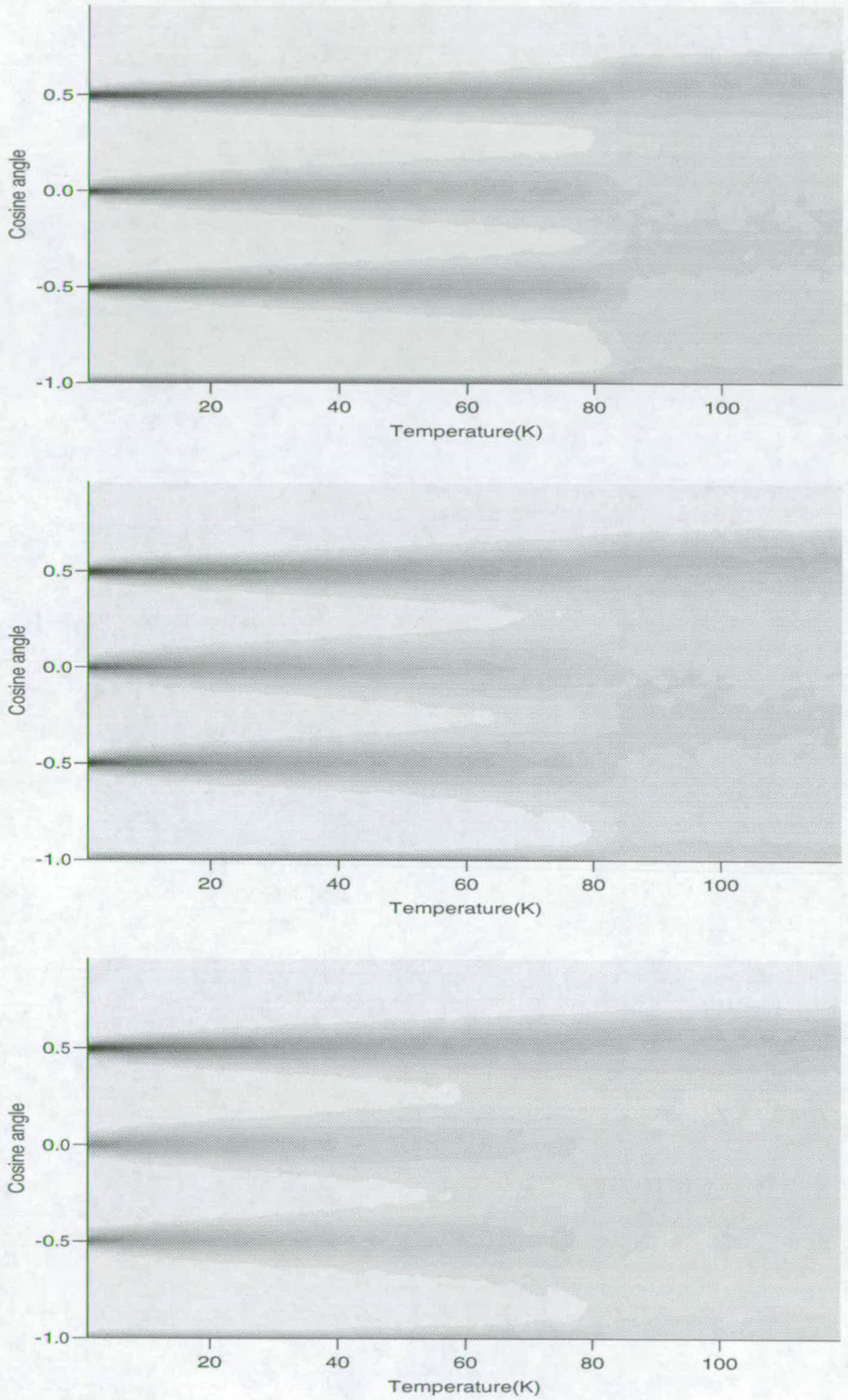

Figure 4.2: ADFs for the heating process: *core(top), mid-shell(middle), and surface(bottom).*

0.3), which is about twice of 53°. Since ADF is a function which sensitively identifies short range order, the broad humps can be regarded as a certain level of local order around atoms although the variation of each hump is large. It might be relevant to the structural formation of the liquid. The liquid phase is, in general, explained as a state where it exhibits absence of long-range order, and has a greater mobility compared to the solid. If solid melts, it shows increase in free volume between atoms although the change would be far less marked compared to the gas. It may be possible that, in the liquid phase, there are chances for two next-nearest atoms to come close to each other but move away from the referenced atom, resulting in the angles being slightly smaller than those found in the fcc crystalline lattice. In the core and the mid-shell in figure 4.2, the lowering of angles happens after the surface where it is rather gradual. It suggests that the order of the fcc structure is destroyed much earlier on the surface than inside the cluster.

Figure 4.3, which are the continuous ADFs of the three parts of the cluster for cooling, shows a supercooling and a transition from the liquid to the crystalline phase at 65K. It is 15K lower than the melting temperature (80K) of the heating simulation as seen in figure 4.2. It is clear from the comparison between ADFs of figure 4.2 and figure 4.3 below 20K that the structure which has formed after the cooling differs from the one initially constructed at low temperature prior to the heating simulation, which was a perfect fcc crystalline lattice structure. All the peaks of the ADF at low temperature in figure 4.3 coincide with those of hcp as shown in figure 4.1, having two faint but distinct peaks in between -0.3/-0.4, and -0.8/-0.9. Although such peaks also do exist in decahedron, one of the faint peaks is, in fact, closer to that of hcp -0.33 rather than that of decahedron -0.39. It is however quite difficult to assert that the structure is truly a hcp crystalline lattice without further analysis due to the fact that the difference in ADF between hcp and the decahedron appears to be very small.

In analysis of ADF for each atom, it is found that some ADFs show decahedral

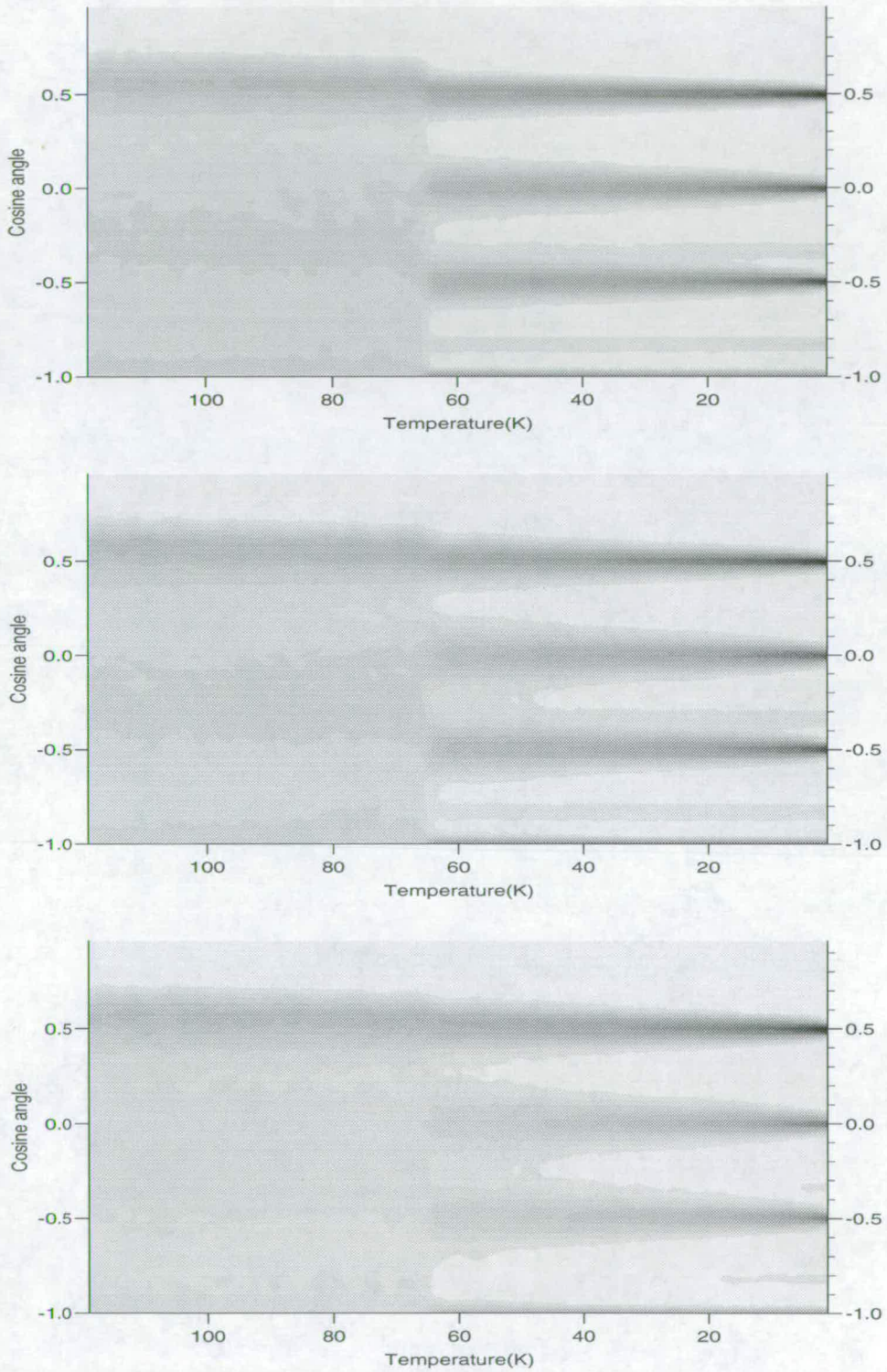

Figure 4.3: ADFs for the cooling process: *core(top), mid-shell(middle), and surface(bottom).*

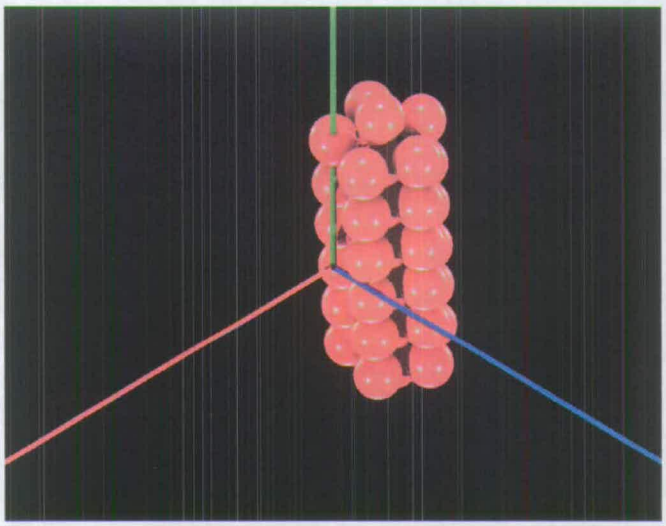

Figure 4.4: Decahedral chains at 1K formed after solidification which is in parallel to y-axis. The green coloured line in the figure represents y-axis in the MD coordinate system, the red is x-axis, and the blue is z-axis.

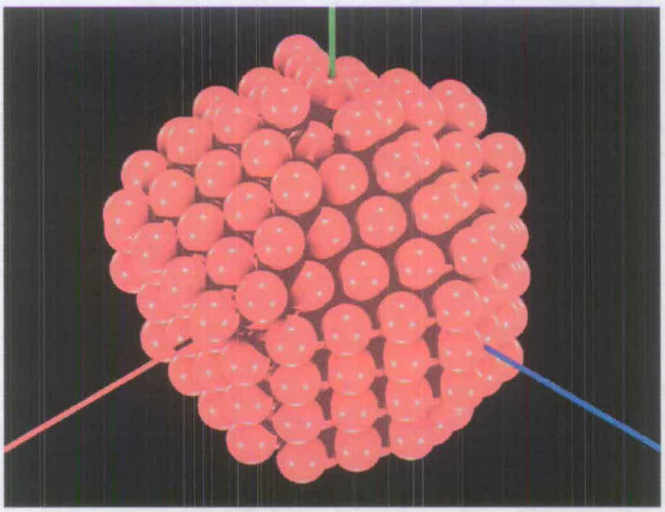

Figure 4.5: Whole view of the cluster at 1K after solidification.

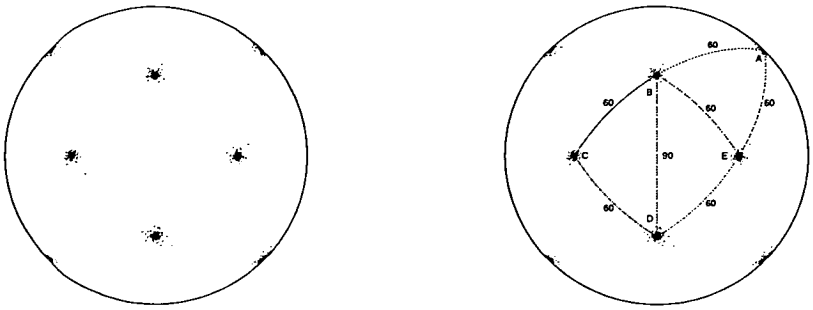

Figure 4.6: Dotplot of a perfect fcc crystal at 10K.

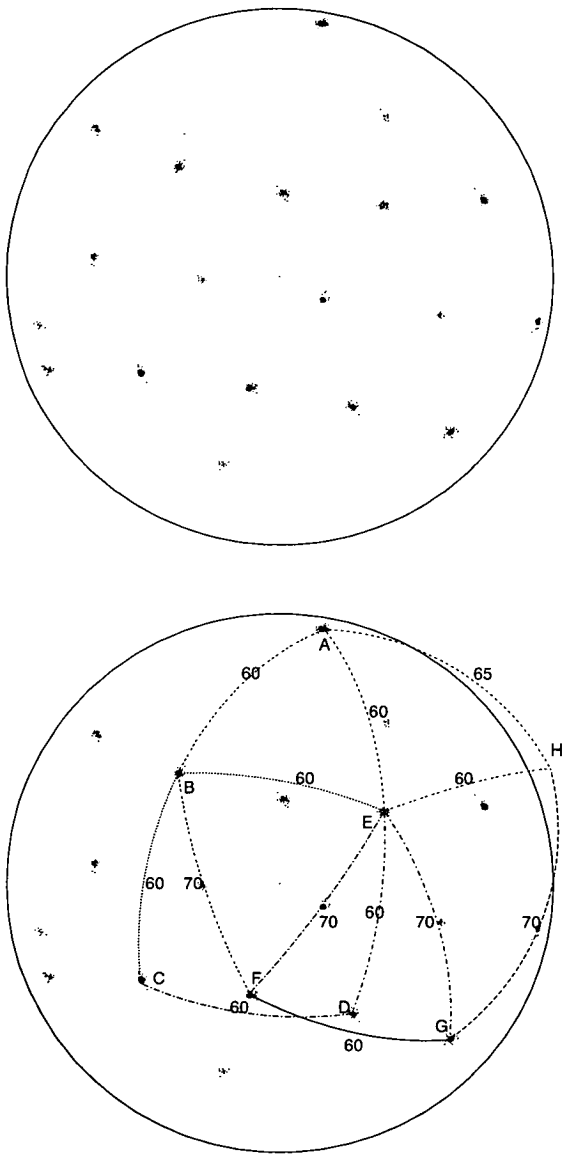

Figure 4.7: Dotplot after solidification at 1K.

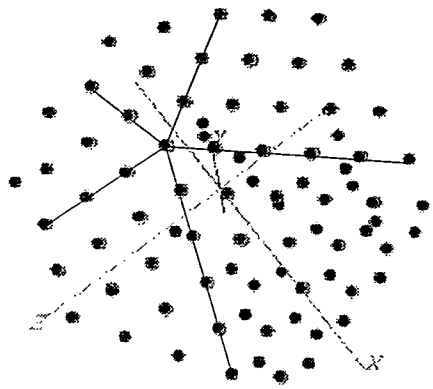

Figure 4.8: A view of all atomic coordinates projected on to x-z plane in the MD coordinate system. The point where five lines are joined together is the position of the five-fold axis.

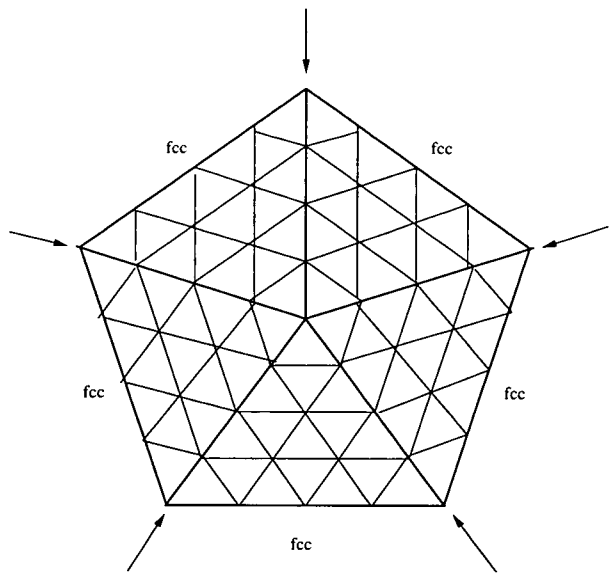

Figure 4.9: An idealised outline of the figure 4.8. The arrows show the boundary regions among the fcc lattice sections.

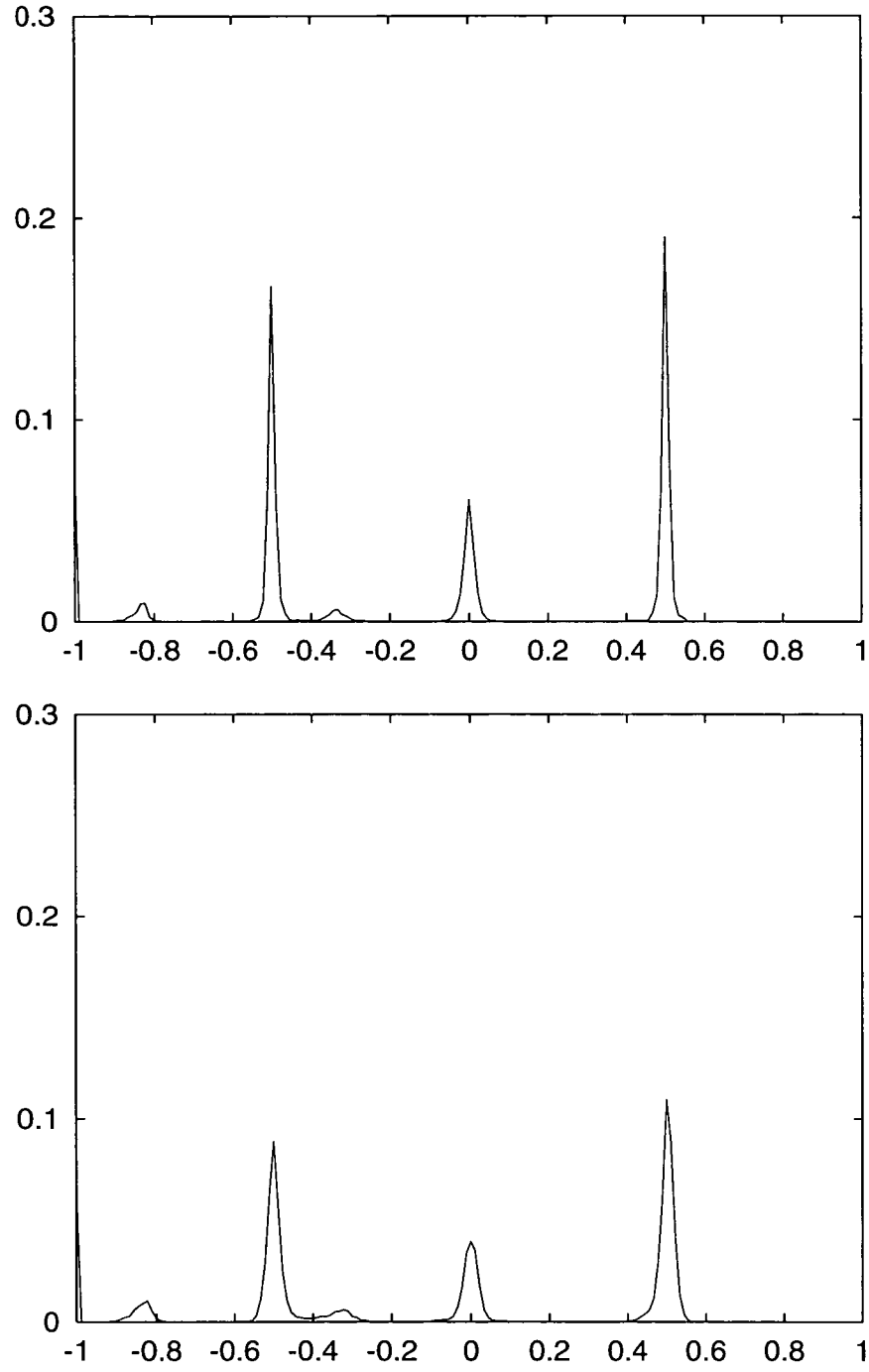

Figure 4.10: Typical ADFs of multi-shell five-fold structures averaged over all atoms in system. The top figure is an multi-shell decahedron and the bottom figure is an multi-shell icosahedron.

peaks. Specifically, they have a peak at -0.39. Every atom and their neighbours which show decahedral peaks in ADF are searched one by one and the label of these atoms are collected in order to find relative positions among atoms involved. It is found that these atoms are close to each other and form a three-dimensional structure, given as a pictorial view in figure 4.4. Three lines in the figure are the three axes of the MD coordinate system, x, y, and z-axis which are red, green, and blue coloured respectively. A series of decahedra chained almost parallel to y-axis is formed in perfect order, slightly offset from the centre of the cluster. In MD simulation, it is possible to trace the same coordinations of the decahedral atoms from the system at low temperature back to the point of the liquid $\rightarrow$ crystal phase transition in cooling. With this method, we can study when this decahedral chain has formed. It is confirmed from the study that the chain has formed at the point of the phase transition, and is very stable during the cooling once it is set except for some exchanges of atoms in the chain with neighbours.

In order to see the overall structure of the cluster with a minimum of thermal motion, a pictorial view of the whole cluster at 1K formed after the cooling is shown in figure 4.5, and the figure exhibits a clear 3-dimensional formation. What we can see from the figure is a multi-shell decahedron. Five triangular faces with hexagonal atomic arrangement are seen on the top of the cluster. The figure also shows that all atoms are arranged parallel to the five-fold axis.

The system is again analysed with the dotplot method (refer to section 2.10) for interatomic vectors which are restricted to nearest neighbours (and the next nearest neighbours for bcc and the decahedron). Figure 4.6 shows a perfect fcc crystalline lattice structure which is taken at the lowest temperature from the initial heating simulation. There are four sets of dot peaks (B, C, D, and E) inside the circle which represent four directions of the nearest neighbours, [011], [0$\bar{1}$1], [101], and [$\bar{1}$01]. Other four sets of dot peaks around the perimeter present four directions of the nearest, [110], [$\bar{1}$10], [1$\bar{1}$0], and [$\bar{1}\bar{1}$0]. A spherical triangle $\triangle$ ABE represents (111) face of the fcc lattice having

60° angles among three dot peaks.

A dotplot of the multi-shell decahedron is drawn in figure 4.7. It has a five-fold axis at point E around which there are five hexagonal faces with certain distortion, suggesting that the five-fold symmetric structure can not be constructed with the perfect fcc lattice. The perfect sites for neighbour atoms in the fcc lattice can be compared in the dotplot of the multi-shell decahedron with polygon ABCDE drawn in both figures. They match perfectly with each other with the same angles.

Figure 4.8 shows that all atoms in the cluster are projected on to the x-z plane in the MD coordinate system. An idealised outline of the figure is also given in figure 4.9 to show a simplified view of the formation of the cluster. In comparison with figure 4.5, it is clear that figure 4.8 shows five sections of hexagonal arrangement around the five-fold symmetric axis. Five lines in the figure joined at the five-fold axis show definite boundaries among the five sections. In fact, each section has the arrangement of the fcc lattice with possible distortion and defects. The bottom right section of the figure exhibits some defects which are presented inside. Since the fcc lattice stacking in a section cannot continue to another section, there are different stackings in the boundary region where another fcc lattice stacking is presented. Angles found in the boundary region are of hcp. Since the overall strucutural formation of each section is the fcc, this gives rise to three strong peaks at -0.5, 0.0, and 0.5 in ADF while the the atoms in the boundary regions give rise to the hcp specific cosine angles at -0.33 and -0.83 and the cosine angles coincided with the fcc.

It seems that five sections of the fcc ordering effectively fit in to a five-fold symmetric arrangement as seen in figure 4.9 with a certain degree of strain. The decahedral chain consists of small number of atoms, about 12 % of the system, whereas the boundary regions consist of about two thirds of the total configurational atoms. Contribution of decahedral peaks is, therefore, small in ADF and dominant peaks would be those of hcp rather than decahedron.

In order to test whether this multi-shell decahedron is reproducible, five more cooling simulations were done with different initial configurations. It is found in the further simulations that two clusters have multi-shell decahedral structure and the rest show multi-shell icosahedral. Typical averaged ADFs of multi-shell decahedral and icosahedral structures are compared in figure 4.10. The top figure shows the ADF of decahedral structure and the bottom figure show the ADF of icosahedral. All peaks seem to match each other although the peaks of the multi-shell icosahedron are much broader. In comparison with the standard ADF of icosahedron as given in figure 4.1, two high peaks of the multi-shell icosahedron are at different cosine angles, being -0.5 and 0.5, which are -0.44 and 0.44 in the standard ADF of icosahedron. It seems suggestive that the multi-shell icosahedron is, in fact, distorted considerably from the perfect icosahedron. Both ADFs of multi-shell decahedron and icosahedron are close to the ADF of hcp.

4.5 Discussion

All six cooling simulations of 300-atom systems show phase transitions to five-fold symmetric structures. This is consistent with experimental results. In fact, the system size used in the present study is within a range where five-fold symmetric structures are known to be dominant [49, 45, 47]. However, structural study by ADF has shown that its overall pattern is of close-packed structure rather than of five-fold symmetric. It is because the contribution of decahedral peaks to the overall ADF is, in fact, very small. Macroscopic analysis easily overwhelm the existence of a small portion of microscopic structures formed inside the system. Therefore, detailed information on the microscopic structures is likely to be lost.

The present cooling simulations have shown that the resulting structures are either the multi-shell decahedral structure or the multi-shell icosahedral with equal probability. Two structures have a common core in their five-fold axis which is decahedron. In the decahedral structure, a number of decahedra are stacked in serial which is a dec-

ahedral chain whereas the icosahedral has a core of two decahedra which are rotated to each other in half through. Following these results, a logical explanation may be possible about the mechanism of nucleation.

According to the classical nucleation theory, nucleus evolves from a small structure to a large one by taking neighbouring atoms until it reaches the critical nucleus whereby it is hardly broke away by thermal fluctuation and therefore grows into a full scale structure. In the liquid phase, tetrahedral formations are everywhere around the system although the formations may not be a perfect tetrahedron but they are considerably deformed from a regular tetrahedron and constantly changing their shapes. When the system is cooled, it is possible that such tetrahedra get stable and transform to a rather perfect form. It must be noticed that the regular tetrahedron is the fundamental building block in construction of close-packed structures, fcc and hcp. At this point however, how can these stable tetrahedra evolve to close-packed structures in large system is unknown. According to the suggestion by van de Waal [47] there is no simple icosahedral $\rightarrow$ fcc phase transition but fcc phase may grow upon a multiply twinned decahedral core. If this is so, possible ways of having close-packed structures is either by stacking normal lattice upon a defect core or by growing the lattice from the beginning.

The next possible step from a regular tetrahedron to a larger structure is to join several tetrahedra together. Two tetrahedra form a trigonal bipyramid which has the smallest binding energy for the configuration number. For the present systems under cooling study, pentagonal structures were formed. In order to construct decahedron, five tetrahedra, one trigonal bipyramid and three tetrahedra, or two trigonal bypyramids and one tetrahedron are required. There are at least three possible ways of forming decahedron. One of those is that a trigonal bipyramid takes one tetrahedron at a time until the completion of the decahedral formation. Another story may be possible that two trigonal bipyramids merge together and then take a tetrahedron to form decahedron. The last would be that one trigonal bipyramid takes a tetrahedron and

merges with another trigonal bipyramid.

Whatever the way it would be, the resulting decahedron cannot be made by perfect tetrahedra, each regular tetrahedron must be distorted to fill the gap of 7°20' which is the remainder angle after the addition of five tetrahedra. Despite the strain due to the distortion, decahedron is the next stable structure. It may be highly probable that the two pentagonal structures, the multi-shell decahedron and icosahedron resulted from the cooling simulations, are from a same origin which is suspected to be decahedron. Even at the following stage of nucleation, a twinned decahedron, which is either an chained double decahedron or icosahedron, still have lower binding energies compared to hexagonal structures. Consequently, large pentagonal structure can be formed by further growth processes upon these nuclei.

A similar atom by atom growth process was also discussed by Fukano and Wayman [49] in a simple hard-sphere-model analysis. However, unveiling the mechanism of the appearence of nuclei at the initial stage of nucleation requires rigorous microscopic structural study. Tracing trajectories of atoms in computer simulation method might particularily be useful in such a study as proved in the present study. In addition, whether or not such pentagonal structures would be followed by a transition to a hexagonal structure is open to a question.

Chapter 5

Freezing of Sulphur Hexafluoride (SF_6)

5.1 Introduction

Experimental research on the kinetics of homogeneous nucleation of molecular systems has been problematic due to the fact that crystallisation usually incorporates foreign matter which largely affects the process of nucleation. An alternative way of doing research into homogeneous nucleation is computer simulation and the technique has yielded fruitful results for decades in conjunction with the development of modern technology. The study of model molecular systems provides valuable insight into the understanding of physical phenomena found in real systems.

Pawley has developed a model [50] for simulating the condensed phases of sulphur hexafluoride (SF_6) in order to study the so-called plastic phase between the liquid and the crystal in which molecules are arranged on an ordered lattice, but exhibit orientational disorder. It was assumed in the model that the molecules were rigid, interacting through an atom-atom Lennard-Jones potential between the six F atoms of any one molecule and all the F atoms of its neighbours. Interactions with the central S atoms were neglected assuming that a modified F-F interaction can incorporate any S-S and S-F interaction. Therefore, the model simplifies into two parameters. There is a rather more complicated potential model [51, 52] developed by Bartell and coworkers

which incorporates 7-site interactions with partial charges. However, it is unlikely that this potential would give much difference due to the fact that the charge distribution gives a hexadecapole, and the hexadecapole-hexadecapole interaction is expected to be weak; in fact if this interaction were strong it is unlikely that there would be a plastic crystalline condensed phase of SF_6. When optimising the two parameters of the simplified potential in a fitting to structural results from neutron scattering studies [53, 54, 55], the potential has shown very little variation. Therefore, the present two-parameter model can be reliably compared with other results.

The real SF_6 molecular system is known to have a plastic crystalline phase between 96K and the melting point temperature 223K, which is translationally ordered with a bcc structure but orientationally disordered. As temperature decreases below 96K, the orientational order appears and the structure becomes monoclinic with space group *C2/m*. In this phase, there are two unidentical sites, one-third of molecules align towards one direction whereas the rest align towards a different direction.

After the development of the model for SF_6 [50], there has been considerable work covering the plastic-to-crystalline phase transition [56], the study of the plastic crystalline phase [57, 58], the collective excitations in an orientationally frustrated solid [53], the low temperature structure [54, 59], and the plastic phase transition in a cluster [60]. The transition temperatures of the model closely agree with the real system, being 110K $\pm$ 4K for crystallisation and 230K $\pm$ 7K for melting.

In one of the molecular dynamics simulations of SF_6, freezing of SF_6 clusters from the liquid state was not found to be successful [60]. It was suggested in the work as being due to the unrealistic purity of the simulated sample used. Bartell and coworkers [52], years later, have shown success in freezing of clusters of chalcogen hexafluorides(SF_6, SeF_6, TeF_6), and suggested that the unsuccessful freezing may have been due to the faster cooling rates adopted in the earlier work. Recently, we have performed a successful freezing MD simulation with an SF_6 bulk system [61] and are now in agreement

with Bartell's group.

In the present work, freezing of bulk SF_6 system will be studied. There are, however, arguments according to Swope and Anderson [11] that artifacts arising from the imposition of periodic boundary conditions (refer to section 2.7) have distorted conclusions derived from most simulations of the freezing of bulk systems. Avoiding such problems may well be by using enormous systems. They argued that, in simulations of small systems with the boundary conditions, a nucleus will feel an image of itself when a solid crystalline region which has developed in a liquid extends to distances approaching half the simulation cell length. Such consequences affect the nucleation process and the rate of crystal growth.

It was suggested in several reports [8, 9, 10] that a system size above 500 particles is enough to be far away from the artifacts of periodic boundary conditions and small system size. However, Honeycutt and Andersen [62, 63] reported simulation studies of 500 and 1300 Lennard-Jones particle systems where the size of the critical nucleus and the time for formation of a critical nucleus exhibited an anomalous dependence on the size of the simulated system. They concluded that this was due to the artifacts of the small size and periodic boundary conditions applied. This has been reviewed by Swope and Andersen [11] with much larger system sizes of 15000 and 10^6 particles, and they suggested that a 15000-particle simulation is large enough not to exhibit system-size dependence, but not large enough to exhibit the diversity seen in the 10^6-particle simulation. Although much study has been done on the analysis of such artifacts, no definitive criterion has been suggested for a simulation size which is not affected by the artifacts.

In computer simulations, equilibration in general requires a very long simulation time. As a result, simulated systems are easily supercooled. Therefore, it is highly desirable to find ways of accelerating transitions to low temperature phases. Since interfering with systems by the so-called non-equilibrium molecular dynamics method

(NEMD) is, however, likely to prolong the process of equilibration, it is important that such interference must be kept to a minimum otherwise the acceleration of transitions would not be achieved. In computer simulations, transition to an ordered phase by shear fluctuation has been widely observed for dense atomic systems [64, 65, 66]. Also, there has been successful simulation work on molecular systems by Gray et al. [67] where a disordered molecular system can be transformed into a positionally ordered phase by shearing, and the ordered state remains stable even after the shearing has stopped. The simulation, however, was carried out only for diatomic and triatomic molecules, which are respectively linear and triangular in shape and are bound to be simpler than 3-dimensional molecules such as SF_6.

5.2 Simulation Detail

Systems of SF_6 molecules are prepared with a density similar to values which can be obtained from the previous simulation results for the appropriate temperature. Densities for systems in plastic phase with bcc structure [57] and in low temperature monoclinic crystalline phase [59] are given in table 5.2. The Lennard-Jones pairwise additive potential function Φ is given as

$$\Phi(r) = \left(-\frac{A}{r^6} + \frac{B}{r^{12}}\right)$$

where A and B are the parameters for the potential function and r the F-F interaction distance. Two parameters are given in table 5.1, and were originally used in the early simulation work [50].

In this work, systems are initially prepared with the molecular number density of 0.01045Å^{-3} at 150K, then equilibrated at the same temperature before taking the system to any other temperature regime. At 150K, the system will have translational bcc ordering but will show orientational disorder since it is in the plastic phase regime.

Since the relative positions of six fluorine atoms from the sulphur atom at the centre of the molecule are fixed, molecular motion can be simply described by translation and

Table 5.1: **Parameters of the Lennard-Jones potential for SF_6**

A	216.81 Kcal/mole $Å^6$
B	83984.2 Kcal/mole $Å^{12}$

Table 5.2: **Density of SF_6 bulk systems**

Temperature(K)	Density(ρ)†
18	0.01120
23	0.01117
75	0.01085
85	0.01078
115.15 ± 0.64	0.01076
150.46 ± 0.78	0.01045
200.05 ± 1.10	0.00994

† *In the unit of molecular number density* ($Å^{-3}$).

rotation. The rotational motion is dealt with using quaternions (refer to section 2.6).

In order to maintain constant pressure, Andersen's method [35] (refer to section 2.8) is employed. It allows the MD cell either to expand or to contract isotropically according to the difference between the pressure of the system and the pressure to be externally applied causing intermolecular distances to change proportionally to the change of MD cell length. Here, the isotropic change in the MD cell may be thought as due to "the movement of a 3-dimensional piston". The piston has a term M with the unit of [mass][length]$^{-4}$ which resembles the physical entity of mass for the particular volume of the MD sample and determines the level of response to the pressure fluctuation. For simulations of bulk SF_6 systems, the value is chosen to be 0.0008 (amu $Å^{-4}$) throughout the simulation. This value allows the piston to fluctuate about 15 times slower than pressure fluctuations.

The rigid molecule model neglects internal vibrations which have oscillation periods on a far shorter time scale than the rotational and the translational motion. The MD time step is chosen to be 0.01ps, a value small enough for the motion of the system we are interested in.

In this work, periodic boundary conditions are applied to simulate bulk systems.

Influences of the boundary conditions on the nucleation process are investigated by simulating various systems of 128, 250, 432, and 1024 molecules with five different initial configurations. They are equilibrated at 240K being liquid and cooled down to 50K at the rate of -0.2K/ps and -0.1K/ps. Between these two temperatures, two first order phase transitions are expected, one from the liquid to the plastic phase and the other from the plastic to the crystalline phase. Stress in the low temperature crystalline phase will not fully be removed unless stress-free MD developed by Parrinello and Rahman (PR method) [33] is used. Since, in the present study, the shape of cyclic MD cell is fixed to be cubic, the so-called cubic boundary conditions, it is likely to have more unphysical affects on systems in low temperature crystalline phase than those in the plastic phase. However, as our main interest is focused on the phase transition between the liquid and the plastic the PR method is not required.

In order to investigate a way of accelerating the nucleation of the phase transition, methods such as shearing by the Lees and Edwards boundary conditions, inclusion of defect molecules, and applied pressure fluctuation are used. Including a small percentage of defect molecules, so that the overall thermodynamical properties are not much altered, would be a natural choice since nucleation is rarely homogeneous as it occurs in nature. Impurities such as foreign atoms and molecules often have a main role in nucleation. Because application of pressure to the system is easily achieved in the constant pressure non-equilibrium molecular dynamics (NEMD) simulation method and requires no alteration of the simulation program, a pressure fluctuation method is also conveniently facilitated. In the following subsections, details for a number of models we use in the present study are given and the results of the models are then given in section 5.3

5.2.1 Shear Flow

The cubic periodic boundary condition (refer to section 2.7) which was originally introduced for the simulation of bulk liquids can be used to set up a molecular system

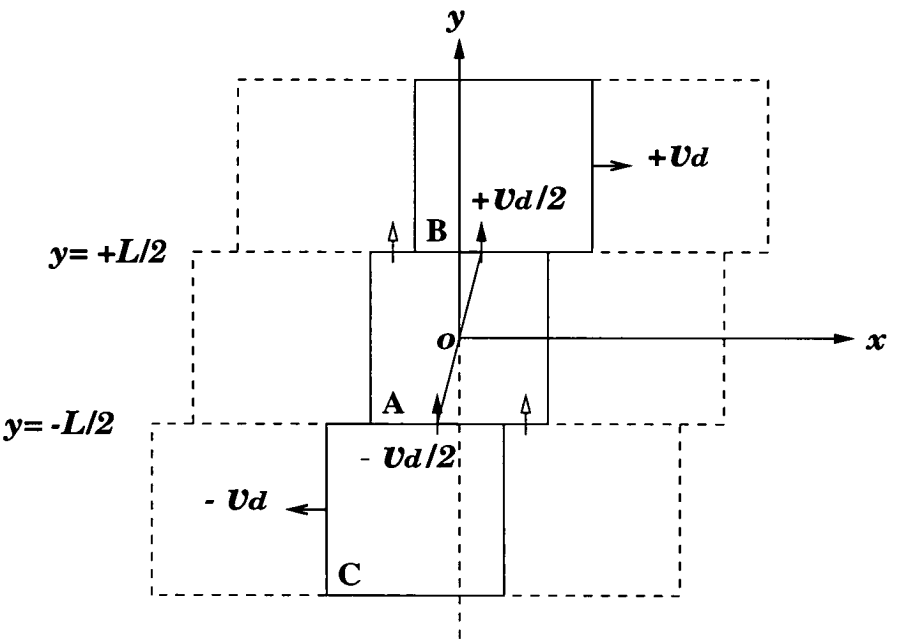

Figure 5.1: Shear boundary conditions

to maintain shear flow. A cubic box containing molecules is replicated throughout space to form an infinite lattice and the movement of a molecule in the original box is duplicated in exactly the same way in its periodic images.

A modification to this boundary condition was proposed by Lees and Edwards [34] in order to maintain a uniform shear flow. The scheme may be explained in the $x - y$ plane by figure 5.1. A simulated cubic box, **A**, shown as a square in the figure, situated at the origin, O, with the box edge of L on each side ranging $-L/2 < L_{x,y,z} < +L/2$ is replicated throughout space. Boxes neighbouring in the y-direction, **B** and **C**, are maintained to drift with a specified speed $\pm v_d (= \Delta r_x / \Delta t)$ in the x-direction to obtain steady shear flow where Δr_x is the displacement of boxes against neighbouring boxes for the time Δt. Molecules crossing the periodic cell boundaries, $y = \pm L/2$, are replaced in the opposite side of the cell with the displacement of $\mp \Delta r_x$ to prevent the build-up of differences in the x coordinates.

Simulations of shear flow are unavoidably involved with the creation of viscous heat which results in numerical complication in the calculation of thermodynamic quantities.

Therefore it is desirable to remove the viscous heat from the system during the shear. There are various different methods generally employed to do this. For instance, it can be done by the Nosé-Hoover thermostat [37, 68], by the Gaussian thermostat [69], or by *ad hoc* rescaling [70] in which two ordinary parallel planes of the MD cell in periodic boundary conditions are replaced by fluid walls flowing with a desired velocity. The Nosé-Hoover thermostat and the Gaussian thermostat incorporate the temperature control into the equations of motion whereas, in the last method the temperature of the fluid walls is maintained at a constant and, by contact with the walls, the viscous heat produced in the system is removed by conduction. However, tests [68, 71] of the various thermostating methods suggested that the results are insensitive to the type of thermostat used.

A steady shear can be obtained systematically with simultaneous removal of the viscous heat. It is achieved by rescaling velocity components of a molecule to maintain its kinetic energy constant after the addition of a shear velocity. First let the shear velocity profile to be applied to the system, $v_s(y)$, be as follows,

$$v_s(y) = \frac{v_d}{L} \times y,$$

where v_d is the velocity of neighbouring periodic box, y the $\mathbf{y}$ coordinate of a molecule, L the periodic box length. This shear velocity is then added to each molecule proportional to its $\mathbf{y}$ coordinate. The velocity before and after this addition may be written as $\vec{v}$ and $\vec{v}'$ respectively as follow,

$$\vec{v} = v_x\mathbf{i} + v_y\mathbf{j} + v_z\mathbf{k},$$

$$\vec{v}' = (v_x + v_s(y))\mathbf{i} + v_y\mathbf{j} + v_z\mathbf{k}\ .$$

However kinetic energy will not be conserved due to the shear application, therefore the final velocity $\vec{v}'$ should be rescaled in order to conserve kinetic energy. It is done systematically as follows,

$$\alpha = \frac{|\vec{v}|}{|\vec{v}'|} ,$$
$$\vec{v}'' = \alpha \vec{v}'$$

where α is the rescaling factor and $\vec{v}''$ the final velocity which is then used instead of $\vec{v}'$. The rescaling must be done on all three components of $\vec{v}'$ so that the shear velocity imposed on the x-component of $\vec{v}$ will diffuse throughout all three components.

It must be noted that there is in fact a limitation on v_d as it may not exceed the velocity limit v_{max} which is defined as follows,

$$v_{max} = \sqrt{\frac{3k_BT}{m}} ,$$

where k_B is the Boltzmann constant, T is the temperature, and m is the mass of the molecule; v_{max} is approximately 1.6Å ps^{-1} at $T = 150K$ for a SF_6 molecule.

When switching off the imposition of the velocity profile it is imperative for the system not to undergo any impulse and, therefore, the transition to the unsheared state must be smooth. Let us assume that the steady shear v_d is imposed. It would be closely given by

$$v_d = \frac{4}{N} \sum_{i=1}^{N} |v_i| , \tag{5.1}$$

where v_i is the x-component of the velocity of the i-th atom (or molecule) in a system of N atoms, taking the origin at O.

At any time-step, v_d can be calculated from equation 5.1, and as v_d will naturally decrease, the shearing will die away. Thermostating is necessary, otherwise the final system will be hotter than we wish. The x-component of the shear profile is subtracted from the vector velocity prior to the calculation of the kinetic energy. This systematic x-component will die away, and should be monitored so that its use in the thermostating algorithm should not continue when it is comparable to the mean thermal velocity for the temperature required.

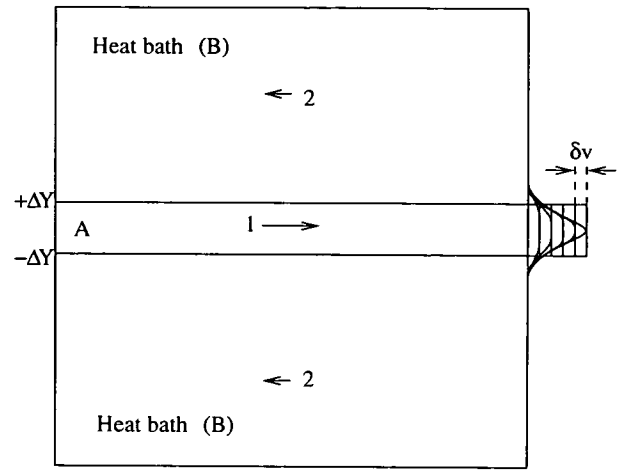

Figure 5.2: An extra small velocity component δv is given to molecules within a thin layer A of the sample.

5.2.2 Accelerated Layer

In this method a thin layer of the sample, 10% of the molecules, is given a small extra velocity component δv for short pulses of time. It is drawn in figure 5.2. The x-component of the velocities of the molecules within the layer between $y = \pm\Delta Y$ is given as

$$v_x \rightarrow v_x + \delta v \quad .$$

In this sequence δv is kept very small compared to the velocities of the molecules. In this manner, the small extra velocity given to the layer will diffuse into the heat bath B of its neighbours in every time step. As the simulation proceeds, v_x around the thin layer will develop a gaussian distribution as drawn in the figure. The region around the thin layer is studied since the given extra velocity components affect most molecules in that regime.

Since the introduction of a small extra velocity to the layer at MD steps will cause overall translational momentum Δv, it must be removed during the simulation by subtracting the overall velocity from all molecules as follow,

$$\Delta v = \frac{1}{N}\sum_{i=1}^{N} v_{x,i} \quad ,$$

$$v_{x,i} \leftarrow v_{x,i} - \Delta v$$

where $v_{x,i}$ is x-component of the velocity of i-th molecule.

5.2.3 Inclusion of Defect Molecules

Linear molecules are used as defects since a SF_6 molecule is easily changed to a linear molecule in computer simulation. The defect is assumed simply for convenience to have the same mass as the host molecule (SF_6) and the same moment of inertia except for the zero moment about the defect molecule axis. Four fluorine atoms in the host molecule are removed and an atom with the same interaction potential as a fluorine atom is added at the defect centre of mass giving three atoms aligned linearly with the same intramolecular bond of the host molecule. In preparation, switching the host molecules to the linear molecules will cause large scale thermal fluctuations due to the difference in potential energy involved between the system before and after the introduction of defects. In order to minimise such impact, the number of defects introduced to the system must be small. Although switching to defect molecules is possible in our model system, in fact it would not be realised in reality and is purely for the preparation of defect systems in simulation study. In a system of 1024 molecules, eight defects are included in the system and are chosen not to interact closely. A system in equilibrium at 240K is cooled down to 50K at the rate of -0.2K/ps to be compared with other freezing simulations.

5.2.4 Pressure Fluctuation

In any real system there will be pressure fluctuations over distances larger than the typical MD cell size. Such fluctuations cannot be generated naturally in the MD work,

and therefore in order to investigate the effects of such fluctuations we have to impose them on our simulated systems.

Systems of 1024 SF_6 molecules in cooling simulations at -0.2K/ps show supercooling down to a very low temperature as given in figure 5.6. Various ways of generating pressure fluctuations are applied to such supercooled systems at several temperatures. One of the pressure fluctuations introduced to the system at 140K is a single short pulse with the duration of 10ps with the pressure of 0.1GPa or 0.01GPa. Triple pulses are also applied with the same procedure of the single pulse. Continuous pressure pulses with the duration of 10ps interval of 10ps with 0.1GPa are also applied to systems at from 120K to 180K with the step of 10K. At 150K, pressure pulses with the combination of 10ps or 20ps of duration times of 0.1GPa or 0.05GPa are investigated. The results of the pressure fluctuation method are then compared with those of equilibration simulations of systems at each temperature in order to examine the effect of the pressure fluctuations on nucleation.

5.3 Results

5.3.1 Finite Size Artifacts

In order to find a proper system size which is free from the finite system size artifacts, cooling simulations were first done with various system sizes before applications of the various methods of accelerating the plastic phase transition.

Results of cooling simulations at -0.2K/ps from five different initial configurations are given for each system size, N=128, 250, 432, and 1024 in figures 5.3, 5.4, 5.5, and 5.6 respectively. They are represented as total energy as a function of temperature which decreases from 240K to 50K. In particular, figure 5.6 also includes a simulation result done with a cooling rate of -0.1K/ps as it shows two clear first-order phase transitions. In general, most cooling simulations show two first-order phase transitions except for some of the large systems. One transition is from the liquid to the plastic crystalline

phase, and the other is from the plastic phase to the solid phase. The four figures of different-sized systems show considerable decreases in the range of transition temperatures as the size of the systems increases. It may thus be observed that statistical variation of the transition temperature will decrease as the system size increases due to the fact that the periodic boundary conditions tend to affect small systems more and give a finite-size enhancement of the transition and a poorer defined temperature.

Figure 5.3 shows that the first transition temperature is between 105K and 165K having a range of 60K. The range becomes 35K from 105K to 140K in 250 molecule systems as seen in figure 5.4. In figure 5.5 for 432 molecules, only two systems show the first-order transition at 100K and 125K and the rest have no such transition throughout the cooling simulations. The 1024 molecule systems do not show clear indications of a phase transition in figure 5.6. The above results show the decrease in statistical variation of the first phase transition as the system size increases.

Since strain due to the cubic boundary condition at low temperature may not be removed from the systems, the solid phase which is not of a cubic lattice will be severely influenced and may exhibit degeneration from the monoclinic phase unless otherwise relieved. By either choosing a cubic lattice or forming a structure other than a single monoclinic crystal structure, a system could fit into the cubic MD cell. The former would have pronounced effects on small systems since nucleus in liquid will be influenced by its periodic images at close interaction. For a large system, the interaction with its periodic images or other local nuclei will be delayed so that the nucleus can grow into a large size where disruption of the grown nucleus by others or its periodic images under the strain would be hard. Competition between an ordered phase and the effect of the cubic boundary conditions would result in formation of abnormal structures which are not of the monoclinic crystalline phase of the SF_6 system.

Since the bcc plastic crystalline structure is known to become a monoclinic crystalline structure when it is cooled further, each high concentration region in the dot-

plots of intermolecular directions will split into two and molecular orientations will be divided into two distinctive directions. However, due to the above reason, systems may not follow the known transition pattern of the bulk system and would not have a perfect monoclinic phase at low temperature. The structures, therefore, may vary between samples.

However, it must be noted that, in this study, whether or not having a perfect monoclinic crystalline phase is not important because what we are most interested in is the phase transition between the liquid and the plastic phase. Examining the low temperature structure under the cubic boundary condition may tell us the effect of the boundary conditions. It is also noted that systems may have more than one crystalline region. In this case, number of dot peaks will be more than that expected from the single crystalline phase. If the system is in a single crystalline phase, the only splitting can be from the basic sets of dot peaks which are those of bcc.

Structures at 50K for various system sizes are given in figure 5.7 and 5.8 as dot-plots. In the figures, column A shows molecule orientations whereas column B shows intermolecular nearest neighbour directions showing the structural formations of the systems. In each column, there are five dot-plots from different cooling simulations which show variation in the low temperature structures. In figure 5.7, three systems of 128 molecules show a perfect bcc positional ordering in which only the top system shows orientational disorder typical of the plastic phase. The centre and the bottom systems are seen to have two distinct molecular orientations. Such orientational orderings differ from those of the monoclinic crystalline phase of the system and it is suspected that the abnormal orientational order may be involved with the cubic boundary conditions. The first system, in particular, is ordered in a perfect plastic phase which is not expected at the given temperature and is, in fact, parallel to the MD cell. It does not show any signs of splitting of dot peaks or local crystallites having different directions of arrangement. It seems to be an obvious example of the effects of the cubic boundary conditions in

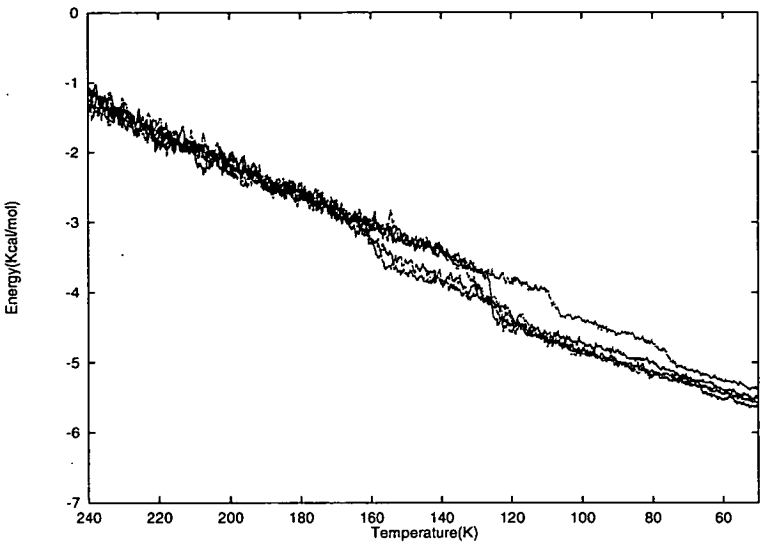

Figure 5.3: Coolings of 128 molecule systems of SF_6 at a rate of 0.2K/ps from different initial configurations.

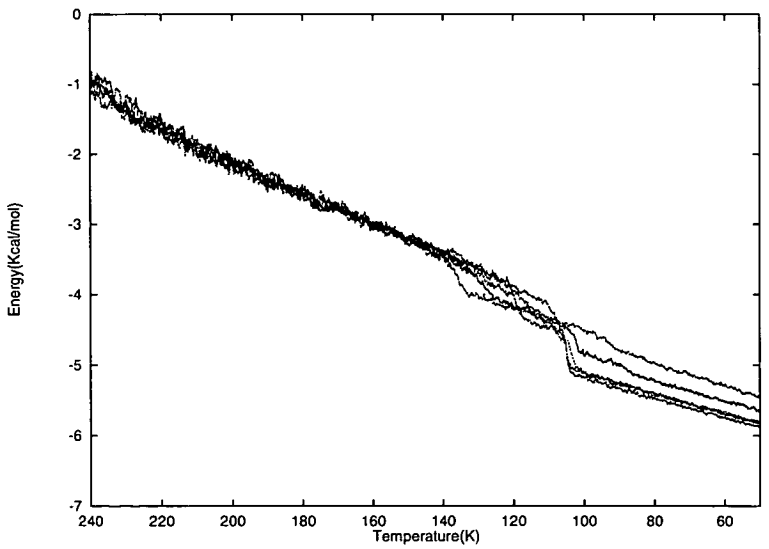

Figure 5.4: Coolings of 250 molecule systems of SF_6 at a rate of 0.2K/ps from different initial configurations.

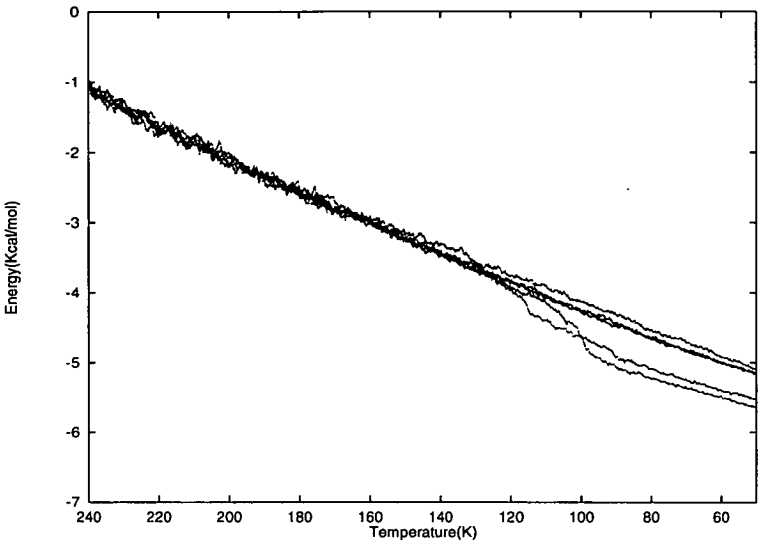

Figure 5.5: Coolings of 432 molecule systems of SF_6 at a rate of 0.2K/ps from different initial configurations.

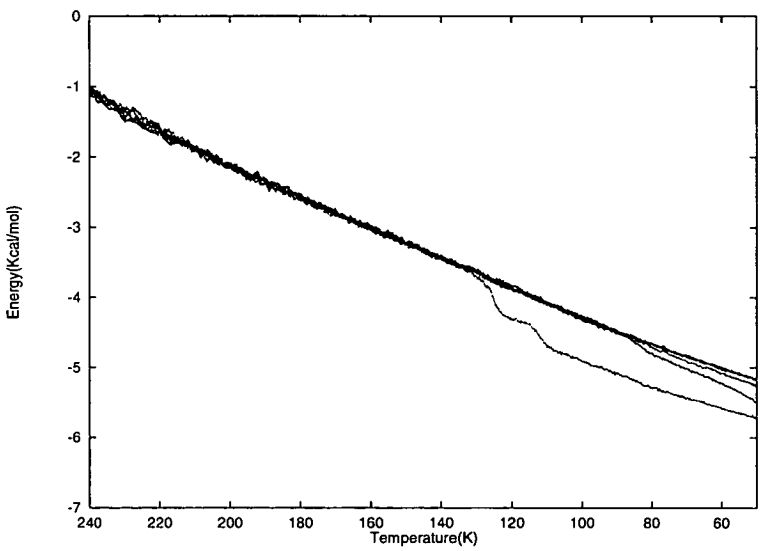

Figure 5.6: Coolings of 1024 molecule systems of SF_6 at a rate of 0.2K/ps from different initial configurations. The one with phase transitions at 110K and 125K in the figure is cooled at 0.1K/ps.

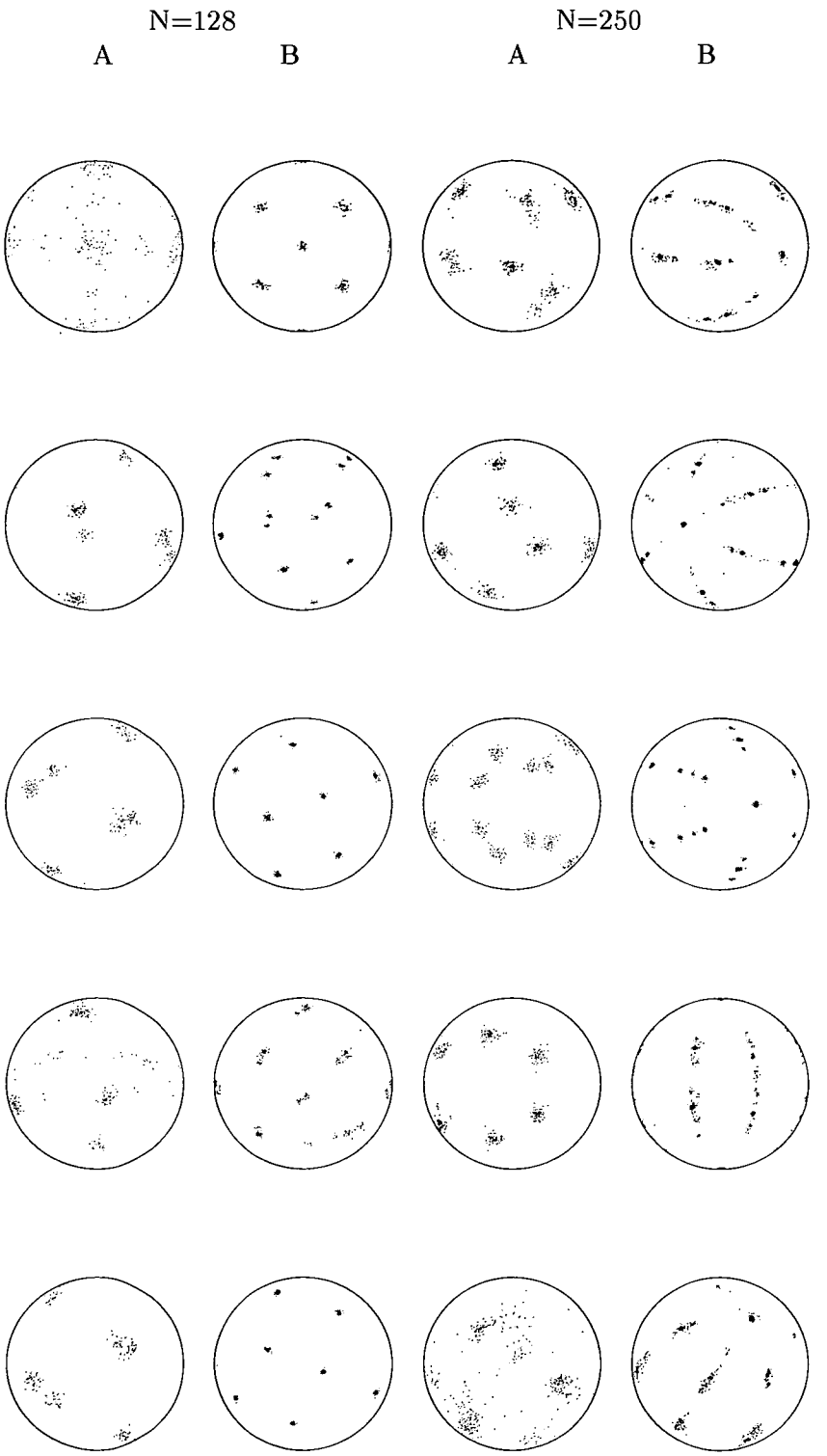

Figure 5.7: Dotplots of molecule orientations (A) and intermolecular directions to the neighbour molecules (B) for N=128 and 250 at 50K for 5 independent configurations for each size.

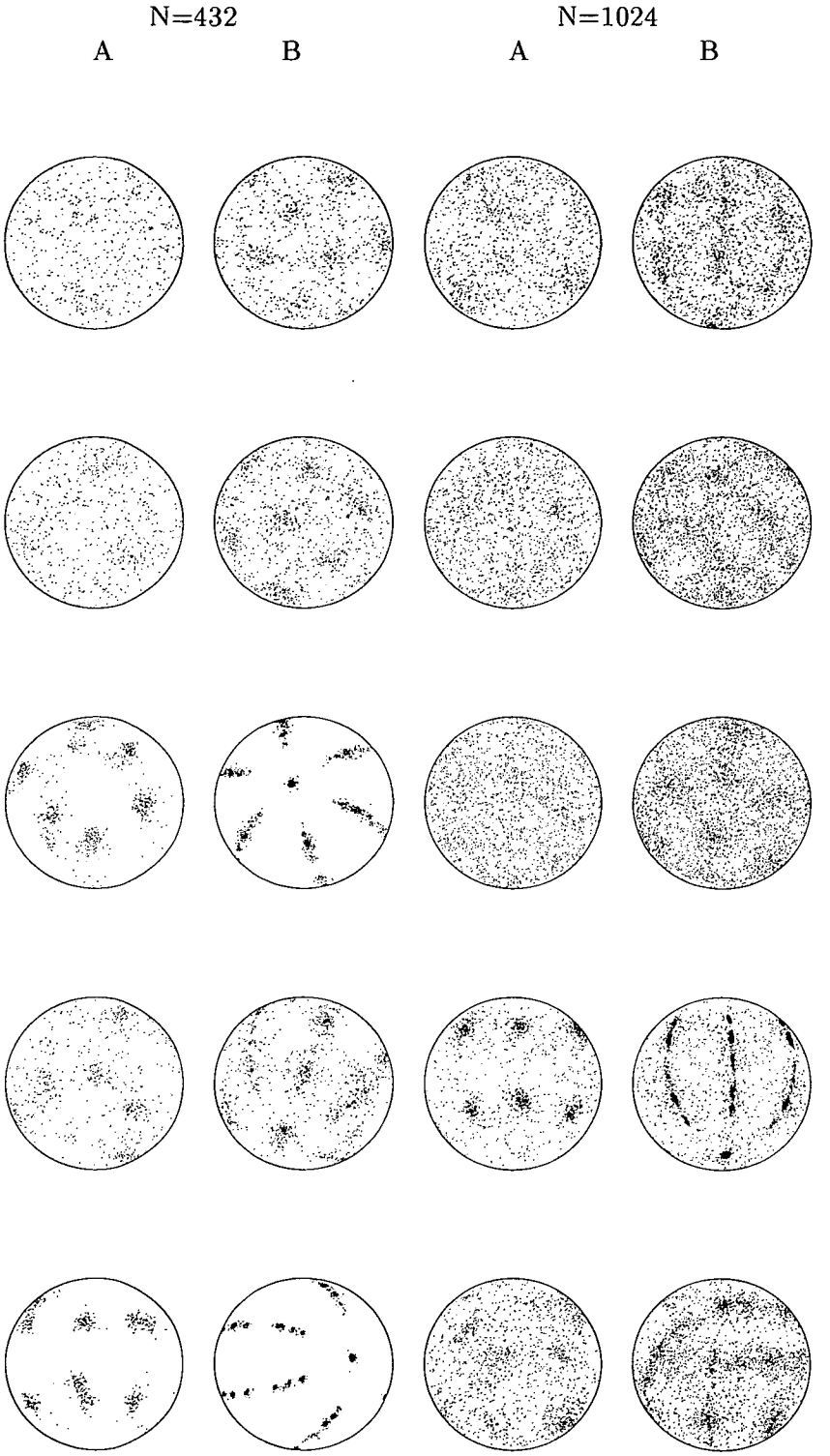

Figure 5.8: Dotplots of molecule orientations (A) and intermolecular directions to the neighbour molecules (B) for N=432 and 1024 at 50K.

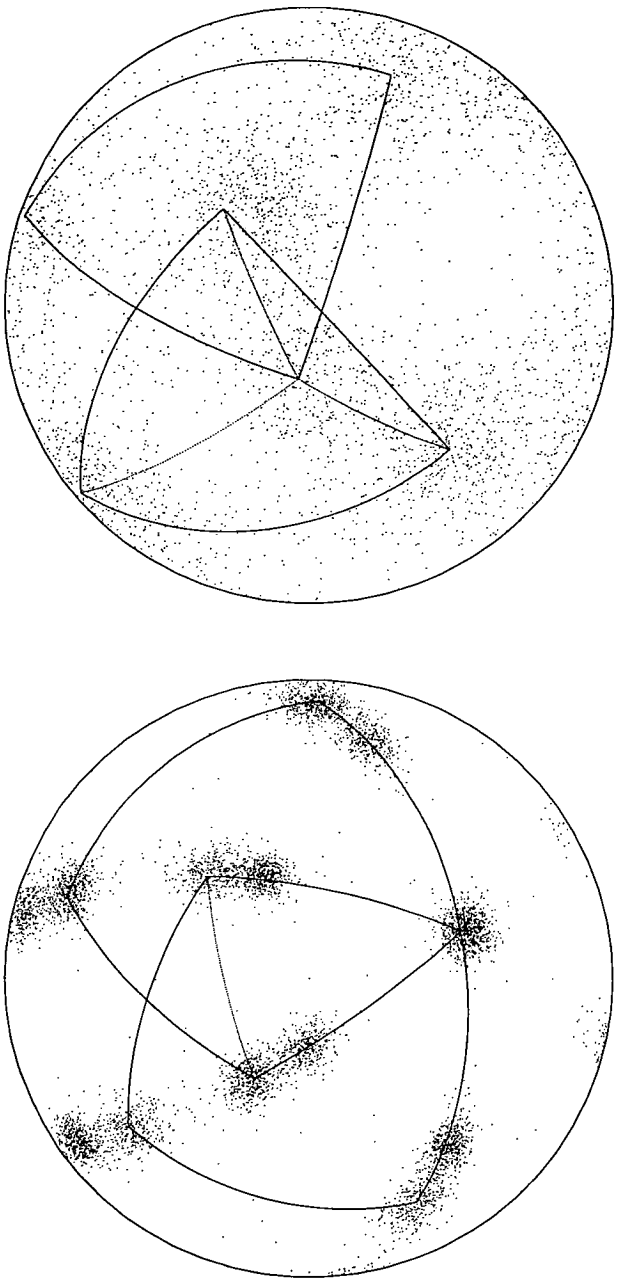

Figure 5.9: Dotplots of molecule orientations (Top) and intermolecular directions to the neighbour molecules (Bottom) frozen at 120K to the plastic crystalline phase. N=1024 and the cooling rate used is -0.1K/ps.

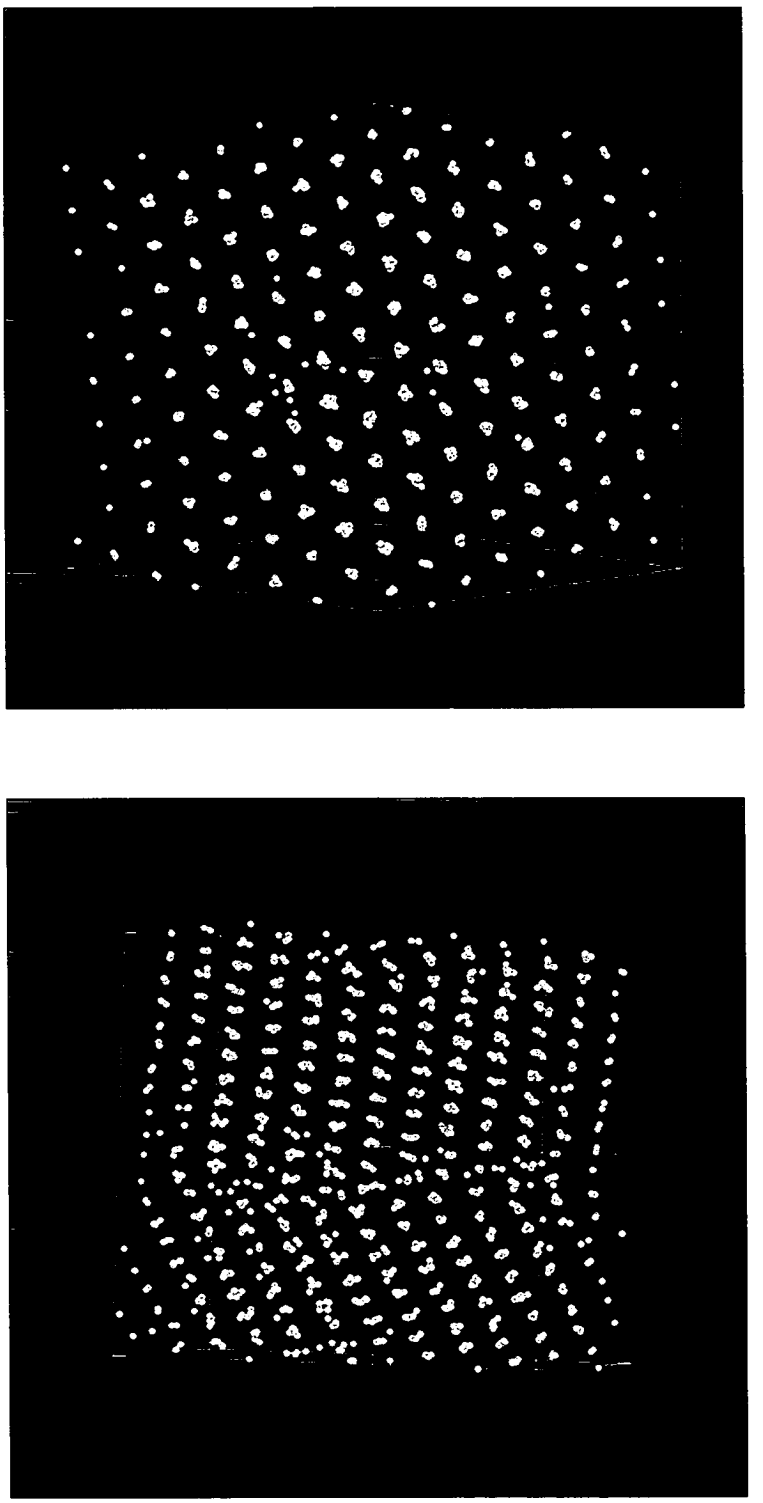

Figure 5.10: Graphical views of molecule centres from [111] direction (Top) and [331] direction (Bottom) for the same configuration frozen at 120K to plastic crystalline phase having the bcc lattice structure. The bottom figure shows two plastic crystalline regions divided horizontally. Axes shown in the figure are perpendicular to the sides of the MD cell.

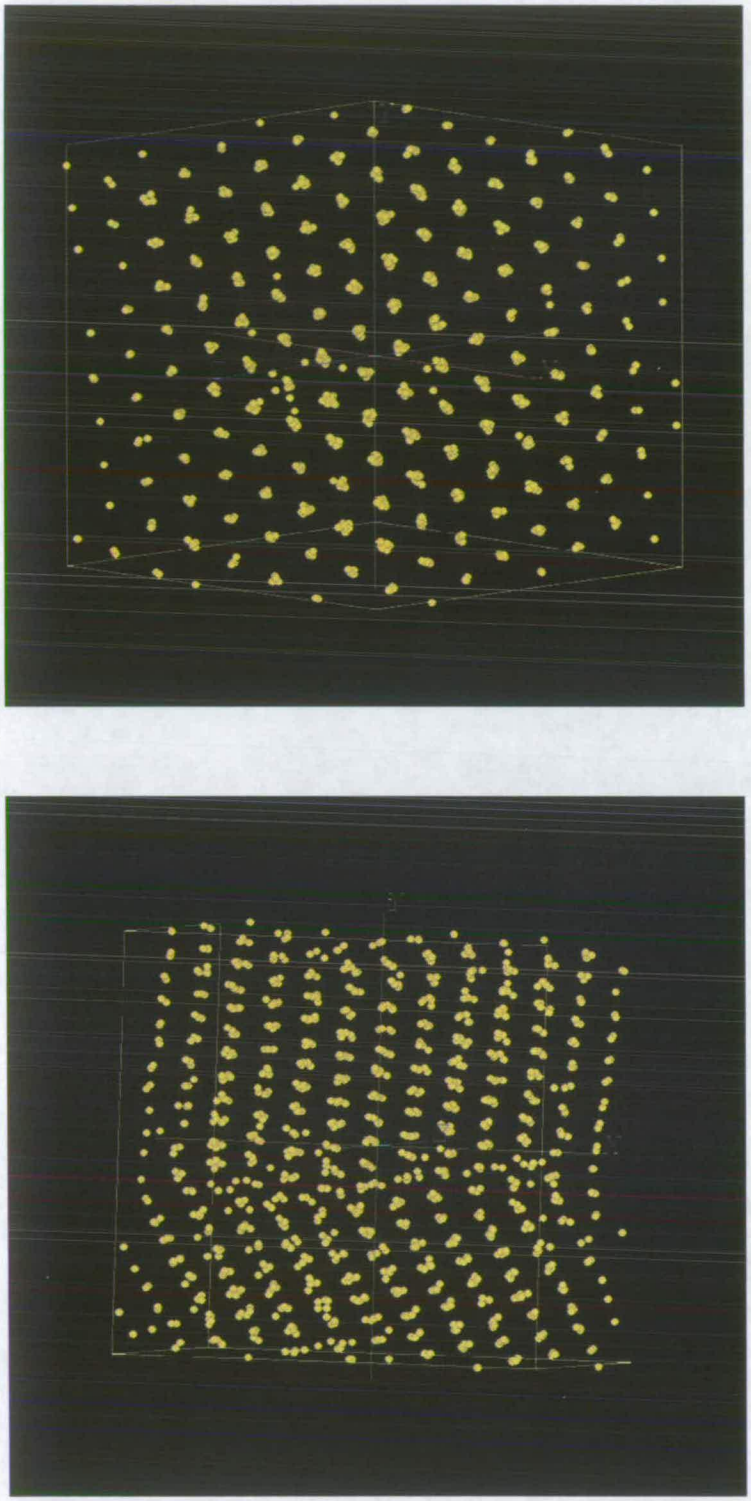

Figure 5.10: Graphical views of molecule centres from [111] direction (Top) and [331] direction (Bottom) for the same configuration frozen at 120K to plastic crystalline phase having the bcc lattice structure. The bottom figure shows two plastic crystalline regions divided horizontally. Axes shown in the figure are perpendicular to the sides of the MD cell.

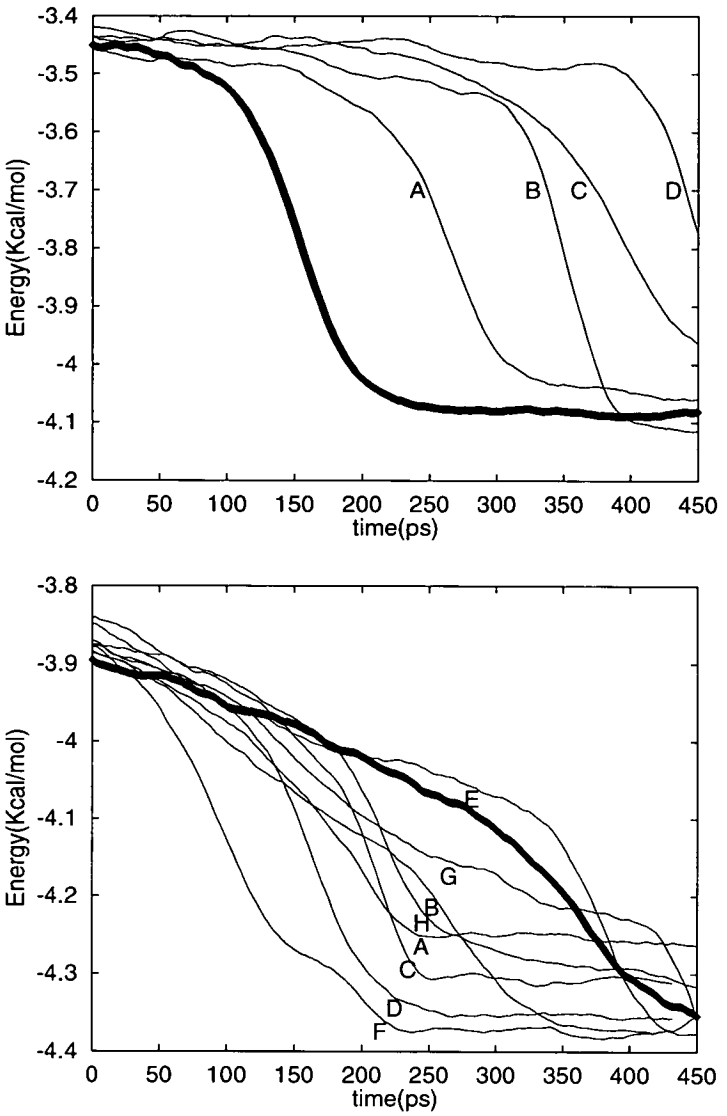

Figure 5.11: Transitions from liquid to plastic crystalline phase by shearing at 140K (top) and 120K (bottom) with the shear rate $\dot{\gamma}$=0.05 ps^{-1}. Thick solid line shows equilibration at the temperature without shearing whereas A, B, C, D, E, F, G, and H are equilibrations after shearings for 0.5ps, 1.0ps, 1.5ps, 2.0ps, 2.5ps, 3.0ps, 3.5ps, and 4.0ps respectively. Each line is averaged over 500 steps.

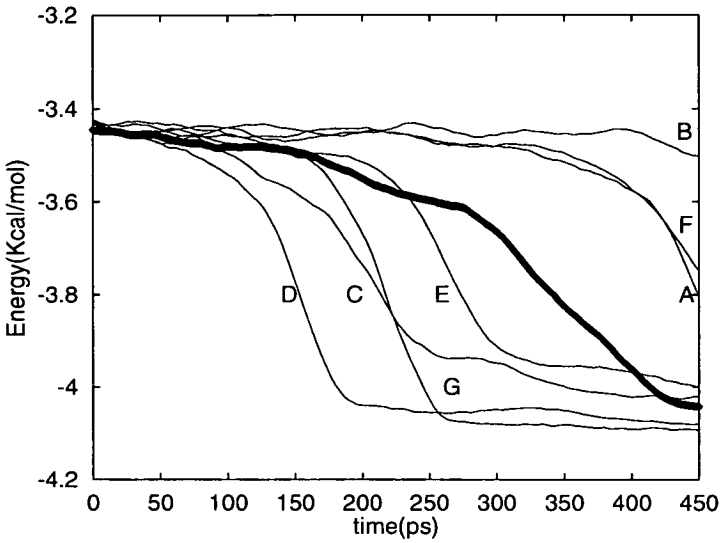

Figure 5.12: Transitions from liquid to plastic crystalline phase at 140K by giving an extra velocity component (0.01Å/ps) to a thin layer of the sample, 10 % of the molecules for short periods of time (10ps, 15ps, 20ps, 25ps, 30ps, 35ps, and 40ps which are A, B, C, D, E, F, and G respectively in the figure). The thick solid line is the transition by equilibration at the temperature. Each line is averaged over 100 steps.

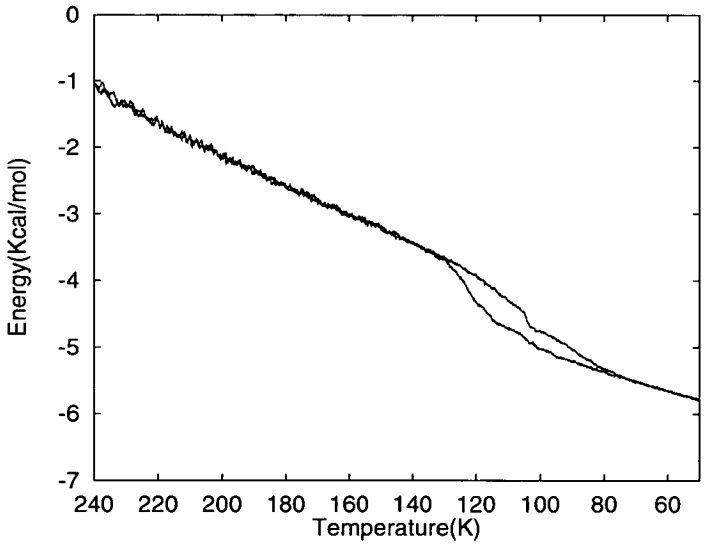

Figure 5.13: Cooling simulations of two systems, which include 8 linear defect molecules, from 240K to 50K at -0.1K/ps with different initial configurations.

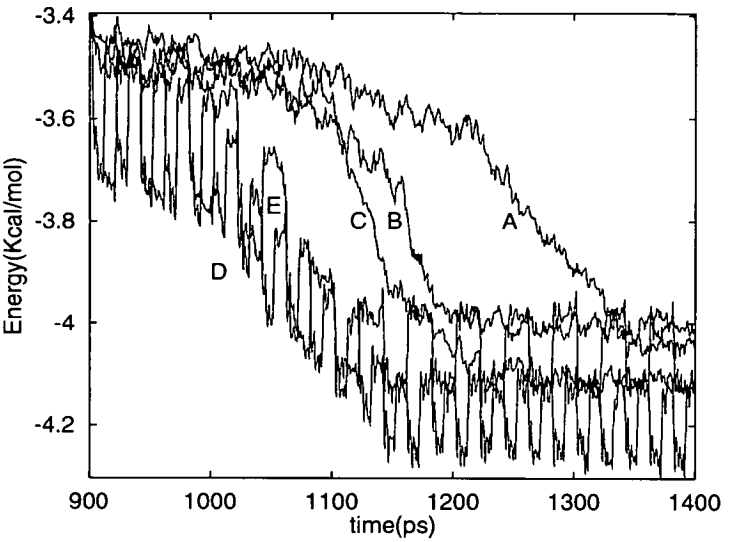

Figure 5.14: Liquid → plastic crystalline phase transitions at 140K by continuous pressure fluctuations with 0.01GPa (B & C) and 0.1GPa (D & E), with pulses of 10ps (B & D) and 20ps (C & E), compared with the transition by equilibration at the temperature (A).

which the only allowed crystal structures have cubic lattices. In the figure, the second system has split dot peaks in its translational dot-plot B and its molecular orientation resembles the results of the third and the fifth systems. Although it is a single crystal, its phase is not the one expected at the given temperature.

Unlike the systems of 128 molecules, the 250 molecule systems develop phases similar to each other. All the dot-plots of the intermolecular ordering show the same monoclinic crystalline phase with variation in the direction of lattice arrangement. They can be regarded as splitting of peaks of the dot-plot of bcc which is given in section 2.4. Based upon the dot-plot, one can envisage each dot peak split into two instead of being one as for bcc for all dot peaks (except for two dot peaks on left and right of the perimeter) along the great circles passing the two dot peaks on the perimeter. There are, however, variations in the crystalline phases developed. Some systems, the third one for example, have more than one crystallite giving a rather complicated pattern in the dot-plot. As we increase the system size to N=432 and N=1024, transitions to the

monoclinic crystalline phase are not apparent as for N=128 and N=250 systems. In 432 molecule systems as in figure 5.8, only two systems develop the crystalline phase with more than one local crystallite implying that more than one nucleus has grown into a crystal, whereas the rest have local crystallites developed within the system and most of molecules are still disordered. This implies that they are not affected greatly by the periodic boundary conditions while manifesting a localised ordering. In fact, some regions develop a crystalline phase which is not directly affected by its periodic image since there are layers of molecules between the phase and the images. In the systems of 1024 molecules, all five systems exhibit local crystallites within a glassy phase. One of the systems clearly show splittings of dot peaks in the crystallite which is in fact due to the result of the monoclinic ordering while it coexists with the disordered solid. It is noted that coexistence of various phases in a system can result from the fast cooling rates adopted.

5.3.2 Freezing Simulation

A system of 1024 molecules is cooled from 240K to 50K at -0.1K/ps which is two times slower than for the above simulations. The result is given in figure 5.6. It has two first order phase transitions, one from a liquid to a plastic phase at 125K and the other from the plastic phase to a solid phase at 110K. The dot-plots for the system just after the freezing to the plastic phase at 120K are shown in figure 5.9, where the top dot-plot shows molecular orientation and the bottom dot-plot shows intermolecular ordering. In the plastic phase, molecules are ordered on a bcc lattice and their orientations are disordered. Although the dot-plot of the molecular orientation has dense areas of dots as seen in the top figure, according to simulation results, molecules in fact flip over to a different orientation within somewhat less than a picosecond. Three vertices of each triangle in the top figure actually show directions to which fluorine atoms are positioned and connecting great circles of three vertices have 90° arcs. Figure 5.9 shows that the system at 120K has two bcc plastic crystallites coexisting within the system.

The bottom figure shows a number of dot peaks and some are denser, some are more compact than others. In the figure, two squares indicate the four diagonal corners 111 of bcc plastic crystallites. The group of dot peaks may represent one plastic crystallite whereas the rest of dot peaks is of the other plastic crystallite. A particular feature of the plastic crystalline structure is that where there are two crystallites they seem to be aligned towards one direction as seen from the bottom figure. One of directions of bcc cubic corners from one plastic crystallite shares a direction of cubic corners of the other plastic crystallite. This explanation becomes apparent when molecular positions are projected on a plane as they are given in figure 5.10. These pictorial views are produced by a visualisation tool called the advanced visualization system (AVS) by which one can view 3-dimensional images of the system from various directions. The axes in the figure are referenced to the MD cell. The top figure shows a view from [111] direction from which two plastic crystallites are ordered in almost perfect manner and the bottom view from [331] direction shows a boundary across the middle of the MD cell.

5.3.3 Shearing

In order to investigate transition by shearing, samples were prepared at two different temperatures, 140K and 120K. At each temperature, a sample was simply equilibrated to be a reference so that the result would be compared with those of later shear simulations. At 140K, shearings were done for a system for four different periods of time. Equilibration simulations were then followed to study the acceleration behaviour in the plastic phase transition. At 120K, shearings for eight different periods of time were done. They were again followed by the equilibration process.

Simulation results of shearing at 140K with a typical shear rate ($\dot{\gamma} = \frac{dv_x}{dr_y}$) 0.05 ps^{-1} are given at the top in figure 5.11. The figure shows first order phase transitions to the plastic phase. The energy of the system is presented as a function of time in picoseconds. The thick solid line shows the plastic phase transition by the equilibration

process. There are four other transition lines A, B, C, and D. The line A shows the transition by equilibration after shearing for 0.5ps whereas B was sheared for 1.0ps, C for 1.5ps, and D for 2.0ps. The figure shows that all four transitions to the plastic phase by shearing happened after the one by equilibration with no shear (thick solid line). In addition, as the period of the shearing gets longer the time taken for the phase transition is consistently delayed further. Particularly, at this temperature, there was no phase transition which happened earlier than the one by equilibration.

At 120K, the results are shown at the bottom in figure 5.11. For the sample, shearing was done for 0.5ps, 1.0ps, 1.5ps, 2.0ps, 2.5ps, 3.0ps, 3.5ps, and 4.0ps which are A, B, C, D, E, F, G, and H respectively. Most equilibration simulations after the shearings seem to exhibit that the transition times to the plastic phase are shortened. However, simulation result such as E for which shearing is done for 2.5ps did not show such acceleration. The shearing period is between those of simulations D and F in which transition times were shortened by half. There is no consistent dependence on the period of shearing. The resulting phases even after the transitions vary broadly. It suggests that there still exists a large translational disorder within each sample.

There is no clear evidence of acceleration that the time taken for the plastic phase transition is greatly reduced by the shearing method despite much attempts with the different shear rate ranging from 0.01 ps^{-1} to above 0.05 ps^{-1}. Simulation results showed that large shear rates seriously affect the estimation of the temperature of the sample. As seen in the comparison of both figures, the increase in energy at 120K just after the shearing at t=0 in the figure is larger than those at 140K. It is believed that at a low temperature molecules are rather closer each other than those at a higher temperature. Therefore, molecules experience higher potential energy changes during the shearing. It would then give rise to the kinetic energy. It is therefore difficult to assert if the results made would reliably be compared with those by equilibration especially when a sample is simulated at a low temperature with a high shear rate.

5.3.4 Accelerated Layer

In attempts of the shear method to induce an early plastic phase transition, it was found that temperature fluctuations due to the energy increase by shearing and its systematic removal was a major obstacle. Such a problem was alleviated by devising a method in which a thin layer of the sample, 10% of the molecules, was given an extra small velocity component for a short period of time at each MD time step. Therefore, there were introduced two shear interfaces through which the given small amount of energy to the molecules in the layer eventually diffused throughout the system where temperature was being regulated, the system behaving as a heat bath.

Figure 5.12 shows seven different simulations at 140K which are compared with the plastic transition result (thick solid line) by equilibration. An extra velocity component given to the thin layer of the sample is chosen to be 0.01Å/ps which is small enough compared to the velocity distribution of the system so that the system does not undergo sudden momentum changes. Although all simulations were begun with the same sample they were given different periods of time for the introduction of the extra velocity component, which ranged from 10ps to 40ps with 5ps step. The figure again shows no consistent reduction of the plastic phase transition time. The broad variation of transition times around thick solid line seem to be the result of what is regarded as transition by chance during thermal fluctuation of the system rather than by the introduction of the extra velocity component. Attempts with a rather small velocity component 0.001Å/ps were also found to be unsuccessful in encouraging an early nucleation. However, for the method to be studied completely, extensive combinations of possible parameters must be required.

5.3.5 Nucleation due to defects

Two samples of 1024 molecules with 8 linear defect molecules were prepared. In order for the defect molecules not to closely interact they were then positioned throughout

the system by shuffling all molecules randomly and analysing relative distances among defect molecules. The samples were then cooled from 240K to 50K at -0.1K/ps.

Figure 5.13 shows that each cooling simulation exhibits plastic crystalline phase transition at about 110K for the lower line and at about 100K for the upper line. These temperatures are even lower than the transition temperature of the previous cooling simulation at -0.1K/ps without defect molecules, which is about 120K as seen in figure 5.6 where the line with two transitions is of the cooling simulation at -0.1K/ps and the step at the higher temperature shows the plastic crystalline phase transition. Therefore, the inclusion of defect molecules in both samples again did not induce rapid nucleation.

5.3.6 Nucleation due to Pressure Fluctuation

Owing to the virtue of the current MD method in which hydrostatic pressure to the system can be given at any state, pressure fluctuation relevant to the nucleation behaviour can easily be investigated. In the very first stages of the present study, attempts were made to encourage nucleation by applying various hydrostatic pressures. All the samples under the static pressures showed no ordering behaviour despite many attempts. We then turned our attention to pressure fluctuations rather than static pressures. We then observed an indication of rapid nucleation with the pressure fluctuation method. Unlike the shear method, this method presents no difficulty in the measurement of temperature due to the fact that the increased energy of a system under hydrostatic pressure is equal to the energy decrease during the release of the pressure.

A supercooled sample of 1024 SF_6 molecules was chosen at 140K. It was then subjected to various short pulses of increased hydrostatic pressures. In figure 5.14, line A presents the plastic crystalline phase transition by equilibration whereas lines B, C, D, and E show the transitions in the presence of the pressure fluctuations. For the sample B, it was under the continual pulses of pressure fluctuation of 0.01GPa with 10ps intervals and showed definite reduction in the transition time which is about 150ps.

Table 5.3: Liquid → plastic crystalline phase transitions at 150K. All simulation results given in this table are examined for 1000ps except for the equilibration process which is monitored over 1500ps.

pressure	number of pulses	duration	result
0.0GPa	no pulse (equil.)	–	no transition
0.1GPa	4 pulses	10ps	no transition
0.1GPa	8 pulses	10ps	no transition
0.1GPa	continuous	10ps	after 450ps
0.05GPa	3 pulses	10ps	after 750ps
0.05GPa	3 pulses	20ps	after 300ps

Under the same pressure but with the longer interval of 20ps, the sample shows about 40ps earlier transition than the one with pulses in 10ps interval. With high pressure fluctuation of 0.1GPa, the transition time is shortened a further 50ps. Although samples D and E differ in the duration of pressure pulses no significant difference was found in transition time except for that the sample with pulses in 10ps interval resulted in a lower energy phase. In the figure, all the pressure fluctuation simulations resulted in rapid nucleation.

In order to investigate the dependence on the type of pressure fluctuations, three different pressure fluctuations were applied to the sample at 140K. They were single, triple and continual pressure pulses. Transition lines in the top figure of figure 5.15 are the results of 0.01GPa pressure pulses. It shows that a single pulse is enough to encourage nucleation. The nucleation time is reduced by 100ps from 1350ps which is the time taken by equilibration only (A in figure 5.14). Triple pressure pulses of 0.01GPa indeed reduced the transition time by a further 50ps. However, continual pulses did not show any further reduction but slightly increased the time taken to the transition.

In the bottom figure, the higher pressure pulses (0.1GPa) are applied to the sample. The high pressure pulses reduced the transition time by a further 50ps than those with 0.01GPa. Therefore, at this temperature, it is summarised that up to a certain number

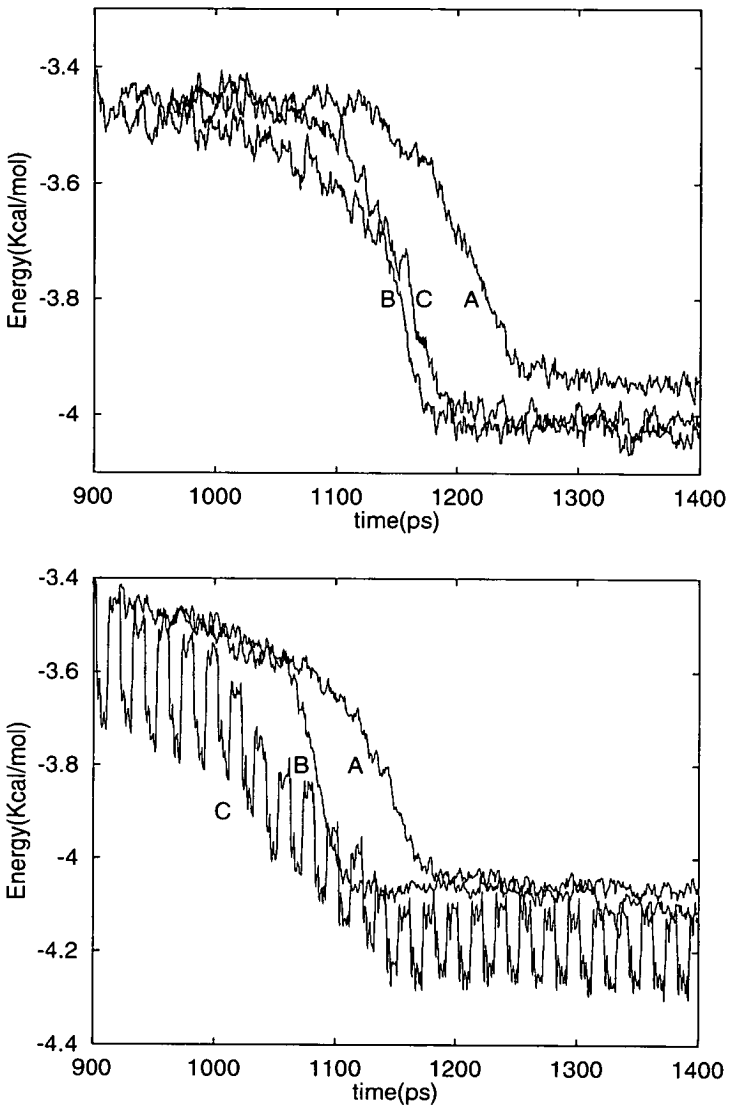

Figure 5.15: Liquid → plastic crystalline phase transitions at 140K by various pressure fluctuations (single, triple and continuous pulses which are referred as A, B, and C in the figure) with pressures of 0.01GPa (top) and 0.1GPa (bottom).

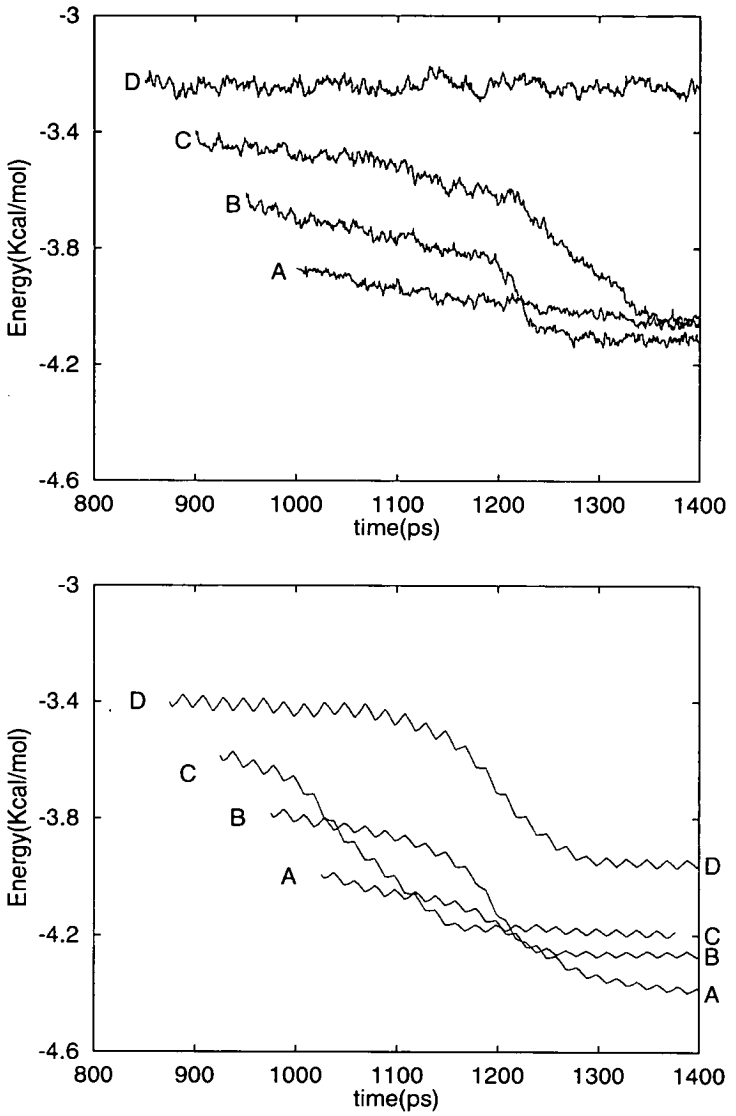

Figure 5.16: Liquid $\rightarrow$ plastic crystalline phase transitions at various temperatures (120K, 130K, 140K, and 150K which are A, B, C, and D in the figure) by equilibration (top) and by continuous pressure fluctuations, 0.1GPa (bottom) which are averaged over 50ps to avoid complication. The top figure shows no phase transition at 150K by equilibration.

of pressure pulses does encourage the nucleation and the higher pressure pulses do encourage the nucleation further. It must however be noticed that further simulation results showed that high pressure pulses give rise to energy fluctuations and if a system under such a high pressure fluctuation is at a high temperature close to the melting point, the system is unlikely to show any acceleration in nucleation.

Until now, all simulations with pressure fluctuations were done at the same temperature. In order to investigate temperature dependence, four supercooled samples were chosen at different temperatures which are 120K, 130K, 140K, and 150K. In figure 5.16, the top figure shows the plastic phase transition lines by equilibration at each temperature whereas the bottom figure show transitions by continuous pressure pulses at 0.1GPa. At 120K which is A, it shows a definite reduction in time taken for nucleation. Surprisingly, the pressure fluctuation also encouraged the sample to go through to a more ordered phase as can be seen in comparison of two resulting phases of A in the top and bottom figures. By equilibration, the energy of sample A became -4.05Kcal/mol whereas it became -4.4Kcal/mol by the pressure fluctuations. Such a phenomenon is also true for the sample B although its transition point hardly suggests any rapid nucleation. As temperature increases to 140K and 150K, the phase transitions definitely show rapid nucleation behaviour. In case of sample D which is at 150K, no transition was found in the simulation of equilibration which lasted over 1500ps as given in table 5.3. For the sample, the transition to the plastic phase by continuous pressure pulses happened after about 450ps. As seen in the table, at this temperature, lower pressure pulses have more possibility of inducing phase transition and longer duration of pulses tend to shorten the transition time. The results at 150K suggest that high pressure fluctuation causes high energy fluctuation and therefore may delay nucleation specially in a system at a high temperature.

5.4 Discussion

According to the report by Swope and Andersen [11], their 15000 particle system was enough not to be affected by the artifacts of periodic boundary conditions although it was not enough to exhibit all the features found from the 10^6 particle system. The system used in the present study is of 1024 SF_6 molecules and its size is roughly compared with half the size of 15000 particle system. We have found our system reliable not to exhibit any abnormality due to the artifacts of periodic boundary conditions. The system has shown general phase behaviour of SF_6 systems even in a solid phase system which is expected to be affected considerably by cubic periodic boundary conditions due to the lattice strain.

Our simulation study on small systems (N=128, 250) resulted in various abnormal formations which are not known for SF_6 bulk systems, for example, translational order aligning perfectly normal to the cubic MD cell with abnormal orientational order or formation of plastic phase at low temperature where it is expected to have monoclinic crystalline phase under the absence of the lattice strain. We regard such an abnormality as due to the artifacts of finite system size and periodic boundary conditions, and expect the abnormality to be eased by increasing system size.

Bartell group's successful report on freezing of SF_6 cluster and other chalcogen hexafluoride clusters which contrasts with the result reported by Fuchs et al. that freezing of SF_6 cluster was found to be unsuccessful gives rise to the question on the model systems used by both groups. However, under our speculative MD simulation study as given in the present work on freezing of SF_6 bulk system following the suggestion by Bartell's group that a slower cooling rate may be required, freezing simulations were found to have a successful liquid $\rightarrow$ plastic phase transition in a temperature regime where the plastic crystalline phase is expected. This result is in agreement with those of Bartell's group and therefore it alleviates concerns over the two model systems and also proves the effectiveness of our two parameter potential model in the MD simulation

study on SF_6 systems.

In the freezing simulation, the resulting plastic phase has shown that there are coexisting multiple crystallites. Each crystallite exhibits the proper phase behaviour expected from SF_6 systems while it coexists with another crystallite. Particularly, in the system in the plastic phase, lattice directions of two crystallites were found to be effectively aligned towards a certain direction. It is understood that each crystallite can grow fully until it interacts with another crystallite which has also grown fully. At this moment, there appears a grain boundary by which they align themselves to fit to the MD cell. However, this is not to be thought as artifacts of small size and periodic boundary condition since phases found from both coexisting crystallites coincide with phases found from previous simulations of SF_6 systems.

In a further long investigation in search of ways to have accelerated nucleation, various attempts such as by shearing, by accelerating a layer of molecules, and by including defect molecules, were found to be unsuccessful and did not show any sign of rapid nucleation. Although there are numerous reports of translational ordering by shear, the so-called the string phase in colloidal suspensions of spherical particles, and also, in both diatomic and triatomic molecule systems by Gray et al. [67] whose translational ordering did not disappear even after the shear was stopped, our shearing simulations show no sign of accelerated nucleation in which the string phase would have a major role. It was found in the shear method that despite the brief moment of shearing it severely affects the estimation of temperature of the system and distorts the comparison with the result made by equilibration. In the simulations of accelerated layer the problems in the estimation of temperature is somewhat alleviated. However, we again found no rapid nucleation although we did not investigate all possible parameter combinations.

The simulations including defect molecules were also an unsuccessful attempt to induce rapid nucleation and we have found moreover that such inclusions of defect

molecules do not minimise supercooling. Our defect simulation results are however confined by the particular molecule type, a linear molecule model. Therefore, there is room for the nucleation study by employing other types of defect molecules. After all, most nucleation found in nature is known to be heterogeneous in which foreign particles act a major role. The defect system used in this chapter will be studied extensively in chapter 6 in the interests of rotational diffusion of host and defect molecules.

In the last attempt by pressure fluctuations, we were not required to do any alteration to our program for the thermostating since the energy increase due to the applied hydrostatic pressure is equal to the energy decrease when the pressure is removed. The pressure fluctuation method was found to be very successful in inducing rapid nucleation [61] and no simulation result has shown the plastic phase transition happening later than the one by equilibration. It is therefore concluded that pressure fluctuation is likely to be the one which associates with nucleation rather than shear fluctuation and subject to a further in-depth study both in theory and experiment.

Chapter 6

Reorientation Motion in Binary Mixtures

6.1 Introduction

As previously discussed in chapter 2, rotational motion is an important part in dynamics of molecular systems and is influenced considerably by detailed intermolecular interactions. For the study of molecular reorientations, the orientational time-correlation function has been developed over decades [12, 13, 14] and understanding of this function based upon experimental spectroscopic measurements has been a major objective in the early stage of theoretical study on molecular rotation [14]. It measures in what degree one dynamic property is correlated to another as a function of time with respect to molecular reorientations, or simply how long some property of a system persists until it dies away by molecular motion. The theoretical foundation of the study of molecular reorientations was firmly established by Gordon [14]. In this work, two generalised models were presented, M-diffusion and J-diffusion models. In J-diffusion, the direction of the angular momentum of a molecule at every collision is randomised and the magnitude is distributed over a Boltzmann distribution whereas only the orientation of the angular momentum vector is randomised in M-diffusion. Further details of Gordon's diffusion models will be discussed in section 6.2 of this chapter. Following Gordon's diffusion models, these were investigated extensively and applied to various types of

molecules, symmetric and spherical top [15, 17].

There are numerous techniques in experiment for probing the dynamics of molecular reorientations, such as infra-red (IR) and Raman spectroscopy [72, 21, 73, 74, 75], nuclear magnetic resonance (NMR) [76, 22], electron spin resonance [77], dielectric spectroscopy [78], quasi-elastic neutron scattering technique [79, 80, 23, 81], and direct time-resolved measurement [82, 83, 84]. These experimental techniques have been used for a wide range of systems, small neutral and charged molecule systems [85], liquid crystals [74], supercritical fluids [84], supercooled glass formers [22], plastic solid phase [79], polar molecules [78], single fluorophore linked to a short DNA molecule [86]. Despite the fruitful results of experimental techniques in the study of rotational dynamics of molecules, no one technique can produce a full spectrum of information on molecular motions. Most experimental techniques used in probing rotational motion only yield the orientational relaxation time τ (defined as the time integral of the correlation function) rather than the full time-dependent correlation function. This orientational relaxation time is often related to hydrodynamic friction parameters through the Stokes-Einstein-Debye relation whereby

$$\tau = \frac{\xi}{6k_BT} \tag{6.1}$$

where ξ is a friction constant, k_B is the Boltzmann constant and T is the temperature.

There are certain spectroscopic methods notably line-shape analysis of infrared or Raman spectra which yield the full time-dependent correlation function obtained by Fourier analysis of spectral band shapes based on the methods developed independently by Bartoli and Litovitz [73] and Nafie and Peticolas [87]. The line-shape analysis technique also requires a delicate experimental method to isolate reorientational information from other sources of noise.

Experiments have been done which use tracer molecules (solute) to study the rotational dynamics of host (solvent) systems. Notable examples are inhomogeneous

rotational dynamics of a rodlike probe in 1-propanol using fluorescence depolarisation technique [88] and the use of single molecule tracer technique [86]. The use of a non-spherical tracer particle in a suspension of spheres was also investigated theoretically [19]. In the recent report of polarised Raman scattering study across the liquid-plastic phase transition regime by Edington et al. [75], a nonmonotonic temperature dependence was observed in the reorientation of linear CS_2 tracer solutes in cyclohexane (C_6H_{12}) solvent upon cooling into the plastic phase. This rotational behaviour of the tracer molecules was, in fact, in direct contrast with the previous nuclear magnetic resonance study (NMR) on the pure cyclohexane by O'Reilly et al. [76] in which a monotonic temperature dependence of the rotational correlation time of cyclohexane was observed. The observed non-monotonic temperature dependent reorientational motion of the tracer molecule (CS_2) as the host (cyclohexane) freezes into the plastic crystalline phase was explained by Edington et al. in their report as the result of an increase in the local free volume in the plastic crystal permitting more rapid "rattling" of the CS_2 molecules at short times than is possible in the liquid just prior to freezing. They argued that faster orientational relaxation over all time scales as expected to be observed in a perfectly spherical solute molecule does not apply to the case for a structurally anisotropic solute. Consequently, the discrepancy in rotational diffusions of two types of molecule requires to be further examined in detail. Stein and Fayer have previously reported observations of rotational inhomogeneity [89] and suggested that the difference in the time scales for spectral diffusion and solvation probably arises from the range of solvent orientational motions that is required for each process. Imeshev and Khundkar have regarded the similar observation [88] in their fluorescence depolarisation experiment in inhomogeneous rotational dynamics of a rodlike probe in 1-propanol as due to the local structure in solvents which may play an important role in observed solvent dynamics. Since it is not possible to completely rule out by experimental techniques why such behaviour occurs, computer simulations at various levels

of molecular detail may provide a considerable insight into the relaxational motions of such molecular systems.

Together with the theoretical and experimental study, research by molecular dynamics computer simulation method has been done over a decade in the study of reorientational molecular motion with various objectives, such as investigation of theoretical memory function model [24], rotational jumps between two different molecular orientations [26], plastic crystals [90, 91], and spherical nanocolloidal particles in solution at infinite dilution [25]. The use of computer simulation has been increasing dramatically owing to both its ability in extracting detailed molecular motion and the rapid development of computer technology. Therefore, molecular dynamics simulation is regarded as the one which not only fills the gap between experiment and theory but also has potential in furthering the study of molecular motion. In the present study, we will investigate molecular rotational motions of both the host and the tracer together by taking advantage of molecular dynamics in which orientations and angular momenta of all molecules of a system are available as a function of time.

Despite the wide use of tracer molecules in the study of host systems, a qualitative study of the details of relative dynamics between the tracer molecules and the host is still to be explored and there are no simulation studies available on both the tracer and the host molecules at the same time in the liquid-plastic transition regime. Therefore, in the present study, our aim is to provide the understanding of the relation between the tracer and the host across the plastic transition regime with particular attention to the contrasting results of the solute and solvent [76, 75]. For our purpose, the readiness of SF_6 molecule systems with linear defects as studied in chapter 5 and our background knowledge of the systems conveniently allow us to investigate the relative rotational dynamics of two molecular types in a binary mixture simultaneously.

6.2 Rotational Diffusion Model

It was originally a common assumption in solving rotational diffusion equations that the molecular reorientation takes place through small angular steps. This was also a reasonable basis for the analysis of early experimental techniques. Gordon [14] has generalised the rotational diffusion models by removing the restriction to small angles and allowing diffusion steps of arbitrary size leading to the M-diffusion and J-diffusion models. In this section, these two models are discussed. In the present work, we will only utilise the M-diffusion model for the study of the linear tracer molecule and the SF_6 host molecule since it is simpler than J-diffusion, thus can be conveniently manipulated for a variety of functions such as for a fitting process, and we have not found in the cases where we have done both that J-diffusion gives a definite improvement. The J-diffusion will be however briefly discussed.

Reorientational motion is usually described in terms of a time-dependent orientational correlation function $C(t)$ that measures the rate at which molecular orientational memory is lost. The correlation function is defined as

$$C(t) =< \hat{u}(0) \cdot \hat{u}(t) > \tag{6.2}$$

where $\hat{u}(t)$ represents the orientation of a bond vector of a molecule in the space-fixed reference frame, and $< \hat{u}(0) \cdot \hat{u}(t) >$ is the statistical average of correlations over time t.

In Gordon's M-diffusion model, the correlation function is a Boltzmann average over contributions, each of which involves a specific value of ω, the angular velocity of a molecule between successive collisions. In equation (6.2), without any collisions in time t, $\hat{u}(0) \cdot \hat{u}(t) = \cos\omega t$. If there is one collision in time t, say at t',

$$\hat{u}(0) \cdot \hat{u}(t) = \cos\omega t' \cos\omega(t - t') - \cos\alpha \sin\omega t' \sin\omega(t - t') \quad , \tag{6.3}$$

where α is the angle between the two angular momentum vectors. Gordon argues that as α is random, $< \cos\alpha >= 0$, and the second term in equation (6.3) averages to zero, and can therefore be neglected. This argument is then used for multiple collisions in the time interval t, and then using the Poisson distribution for the number n of collisions in t, and the Boltzmann averaging, the correlation function can be written

$$C(t) = \int_0^\infty \omega e^{-\frac{1}{2}\omega^2} d\omega \times e^{-\frac{t}{\tau}} \sum_{n=0}^{\infty} \tau^{-n} I_n(t) \quad , \tag{6.4}$$

where τ is the mean time between collisions, and $I_n(t)$ is a multiple integral,

$$I_n(t) = \int_0^t f(\omega[t-t'])I_{n-1}(t')dt' \quad ,$$

$$I_0(t) = f(\omega t) = \cos(\omega t) \quad .$$

For a linear molecule which is used in the present study as a defect molecule, $\hat{u}(t)$ is regarded as a unit bond vector along the linear molecule. We use a similar argument later for the spherical top function. More general extensions are available [18].

6.2.1 M-diffusion for spherical top

Gordon's equation for M-diffusion of a linear molecule makes repeated use of $\cos(\omega t)$ where the axis for the angular velocity ω is always taken at right angles to the length of the molecule. The end of the molecule vector therefore sweeps out arcs $\Omega = \omega t$ which are great circles in spherical geometry. When we have spherical top symmetry, the chosen vector for the correlation function is rarely equatorial, that is to say at right angles to the angular velocity vector, and the arc it describes is usually a small circle.

In the figure let AB be the equatorial arc Ω for one motion step, and CDE the small circle described by a general position of the chosen vector during this step, where ZOC is the azimuthal angle ϕ. PQ is the great circle through C and E, and we need the angle CE in this great circle, θ, which is

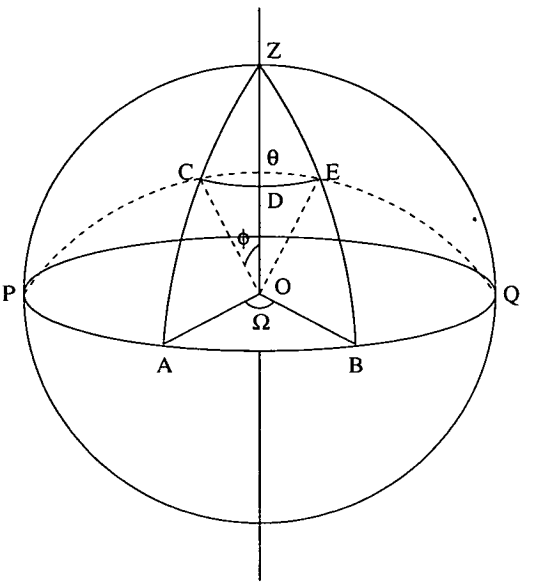

Figure 6.1:

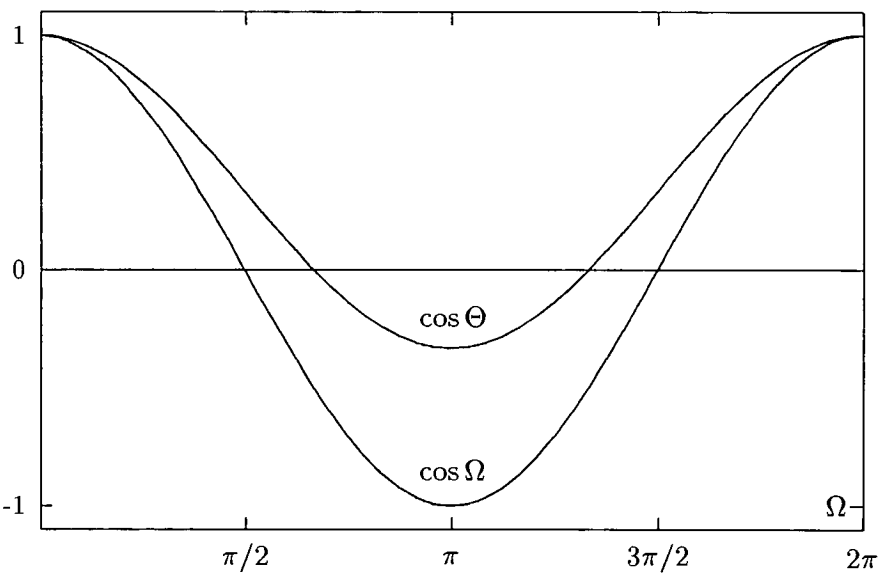

Figure 6.2: A comparison of $\cos\Theta$ and $\cos\Omega$ as a function of Ω.

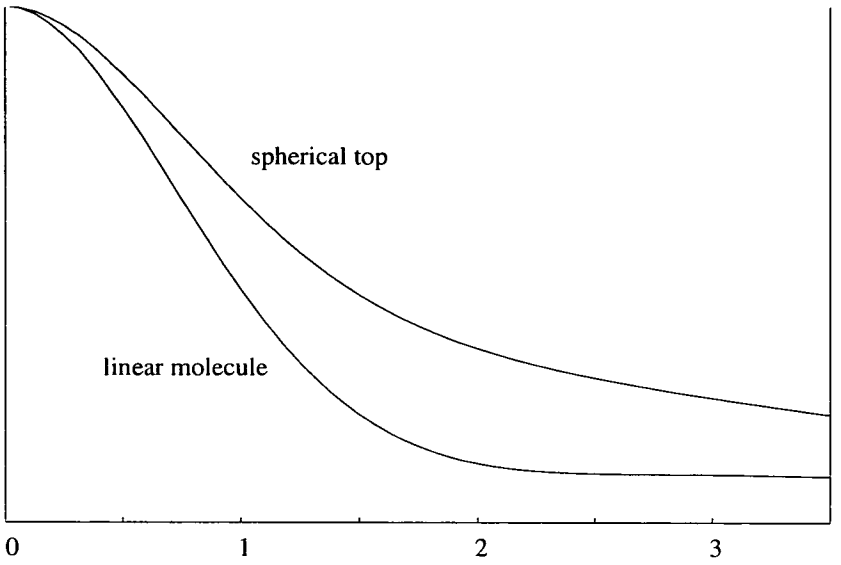

Figure 6.3: Comparison of correlation functions of linear and spherical top molecules for τ=1, in reduced time scale.

$$\theta = 2\sin^{-1}[\sin(\Omega/2)\sin(\phi)] \quad . \tag{6.5}$$

The cosine of this can then be averaged over the whole sphere to give a value $\cos\Theta$,

$$\cos\Theta = \int_0^{\pi/2} \cos\theta \sin\phi d\phi \quad , \tag{6.6}$$

which replaces $\cos\Omega$ in Gordon's expressions for the linear molecule to give the correlation function for the spherical top. This is easily obtained accurately numerically, $\cos\Theta$ being presented in figure 6.2 as a function of Ω, along with $\cos\Omega$.

The correlation functions in figure 6.3 are both for $\tau = 1$ for reduced time t^* up to 3.5, $t^* = t\sqrt{k_B T/I}$ where t is the MD time in ps, k_B is the Boltzmann constant, and T is the temperature. The figure shows the difference between the M-diffusion model

result with Gordon's linear molecule function and with our Θ-function for spherical top symmetry.

6.2.2 Numerical integration of M-diffusion for linear molecules

Let us take T as the total time interval for an integral where t is the integration variable. This is different from Gordon, chosen here as we have to reduce all computations to simple integrals of one variable.

When $n = 0$ there are no collisions and we need $I_0(T) = \cos(\omega T)$, the first in the series $I_n(T)$ that we need. Note that for $n > 0$, $I_n(T)$ is an integral, but is a simple expression for $n = 0$. For one collision, $n = 1$, we have

$$I_1(T) = \int_0^T \cos(\omega[T-t])\cos(\omega t)dt = \frac{T}{2}\cos(\omega T) + \frac{\sin \omega T}{2\omega} \quad . \tag{6.7}$$

For two collisions, $n = 2$, we have, partly using Gordon's notation temporarily,

$$I_2(T) = \int_0^T dt_2 \cos(\omega[T-t_2]) \int_0^{t_2} dt_1 \cos(\omega[t_2-t_1])\cos(\omega t_1) \tag{6.8}$$

$$= \int_0^T \cos(\omega[T-t])I_1(t)dt \quad . \tag{6.9}$$

Let us use the simple trapezium rule for numerical integration. Although this may not be the most accurate method, we will easily be able to test accuracy when the program is written. Integrals are all over the range T, which is divided into m steps, and we need to add $m+1$ values of the function, the first and last involving a factor 1/2. Thus setting $T = m\Delta$,

$$I_2(T) = \Delta\left[\frac{0}{2} + I_1(\Delta)\cos(\omega[m-1]\Delta) + I_1(2\Delta)\cos(\omega[m-2]\Delta) + \ldots + \frac{I_1(T)}{2}\right]$$

where we have used $I_1(0) = 0$ in the first end term and $\cos(0) = 1$ in the last. We will be able to do the same at each stage of integration as $I_n(0) = 0$ for all n, thus

$$I_2(T) = \int_0^T \cos(\omega[T-t]) I_1(t) dt \quad , \tag{6.10}$$

$$I_3(T) = \int_0^T \cos(\omega[T-t]) I_2(t) dt \quad , \tag{6.11}$$

and therefore we can write generally

$$I_n(T) = \Delta \left[\frac{I_{n-1}(T)}{2} + \sum_{k=1}^{m-1} I_{n-1}(k\Delta) \cos(\omega[m-k]\Delta) \right] \quad . \tag{6.12}$$

This is probably what Gordon referred to in his comment that the successive convolution integrations become simply matrix multiplication. The summation involving τ^{-n}, the involvement of $\exp(-T/\tau)$ and integrations over ω given in equation 6.4 are now straightforward. Note that in the formulation above it is not necessary to use an analytic integral for I_1, but it does improve accuracy. We could have used numerical integration throughout using

$$I_1(T) = \int_0^T \cos(\omega[T-t]) I_0(t) dt \tag{6.13}$$

where $I_0(T) = \cos(\omega T)$, the basic function in the M-diffusion model.

6.2.3 J-diffusion for linear molecule

For J-diffusion we must use numerical integration throughout, and to get accuracy the first integration is best done with a finer time step. The expression for the basic function, $F_0(T)$, which replaces $I_0(T)$ in the M-diffusion expression, is

$$F_0(T) = \sum_{m=0}^{\infty} (-1)^m \frac{T^{2m} 2^m m!}{(2m)!} = \sum_{m=0}^{\infty} f_m(T) \quad . \tag{6.14}$$

We can express this rather more conveniently for computation by observing that

$$f_0(T) = 1 \quad \text{and} \quad f_m(T) = -\frac{T^2}{2m-1} f_{m-1}(T) \quad . \tag{6.15}$$

The expression for the integrals is therefore

$$I_n(T) = \Delta \left[\frac{I_{n-1}(T)}{2} + \sum_{k=1}^{m-1} I_{n-1}(k\Delta) F_0([m-k]\Delta) \right] \quad . \tag{6.16}$$

The summation involving τ^{-n} and the involvement of $\exp(-T/\tau)$ as given in equation 6.4 are again straightforward.

6.3 Analysis

6.3.1 Reorientational correlation function

The reorientational correlation function $C(t)$ is defined as in equation 6.2. For SF_6 host molecule, the orientation of the molecule is represented as quaternions (refer to section 2.6) and therefore reorientational correlation function is then defined as

$$C(t) = < \mathbf{q}(0) \cdot \mathbf{q}(t) >$$

where $\mathbf{q}(t)$ is the unit quaternion of a molecule at time t.

We simulate a sample of 1024 SF_6 host molecules in which about 1% of defect molecules is included. The correlation function of defect molecules will therefore have poorer statistics due to the lack of configuration number while the analysis for the host does not. Statistics for the defect correlation function can be improved by accumulating the correlation function over a sufficient time.

If we let $\hat{u}(0)$ be the unit vector which is parallel to the bond vector of the linear defect molecule at $t = 0$ and $\hat{u}(\Delta)$ at a time Δ later, the correlation function for the linear defect molecule is defined as

$$C(\Delta) = < \hat{u}(0) \cdot \hat{u}(\Delta) >$$

where Δ may be a MD time step or its multiples at which orientations of molecules are sampled. If the correlation functions are accumulated over m times for each correlation time (1Δ, 2Δ, ..., $N\Delta$), they are then written as expansion forms,

$$F(\Delta) = \hat{u}(0)\cdot\hat{u}(\Delta) + \hat{u}(\Delta)\cdot\hat{u}(2\Delta) + \ldots + \hat{u}((m-1)\Delta)\cdot\hat{u}(m\Delta) \quad ,$$

$$F(2\Delta) = \hat{u}(0)\cdot\hat{u}(2\Delta) + \hat{u}(\Delta)\cdot\hat{u}(3\Delta) + \ldots + \hat{u}((m-1)\Delta)\cdot\hat{u}((m+1)\Delta) \quad ,$$

$$F(3\Delta) = \hat{u}(0)\cdot\hat{u}(3\Delta) + \hat{u}(\Delta)\cdot\hat{u}(4\Delta) + \ldots + \hat{u}((m-1)\Delta)\cdot\hat{u}((m+2)\Delta) \quad ,$$

$$\vdots \qquad\qquad \vdots$$

$$F(m\Delta) = \hat{u}(0)\cdot\hat{u}(N\Delta) + \hat{u}(\Delta)\cdot\hat{u}((N+1)\Delta) + \ldots + \hat{u}((m-1)\Delta)\cdot\hat{u}((m+N-1)\Delta) \quad .$$

They can be simplified as,

$$F(k\Delta) = \sum_{i=1}^{m} C(k\Delta)_i = \sum_{i=1}^{m} \hat{u}((i-1)\Delta)\cdot\hat{u}((i+k-1)\Delta)$$

where $k = 1, 2, ..., N$. Since the distribution of individual correlation function values is not a normal distribution and the individual terms in these summations will not be statistically independent, the statistical average and its standard deviation are calculated by the central limit theorem, stating that the average over means of a discrete number of data sets converges. We let $\bar{C}_{kK}$ be the mean for a discrete set $K(= 1, 2, \ldots, l)$ assuming that there are l discrete sets within m data and j is the number of data for each discrete set, and let $C_{k\Delta}$ be the average over the means. The average is defined as

$$\begin{aligned} C_{k\Delta} &= \frac{1}{l}\left[\frac{1}{j}\sum_{i=1}^{j} C(k\Delta)_i + \frac{1}{j}\sum_{i=j+1}^{2j} C(k\Delta)_i + , \ldots , + \frac{1}{j}\sum_{i=m-j+1}^{m} C(k\Delta)_i\right] \quad , \\ &= \frac{1}{l}\sum_{K=1}^{l}\frac{1}{j}\left[\sum_{i=(K-1)j+1}^{Kj} C(k\Delta)_i\right] \quad , \end{aligned}$$

$$= \frac{1}{l}\sum_{K=1}^{l} \bar{C}_{kK}$$

where $l = m/j$. Therefore, the variance $var(k)$ is then defined as

$$var(k) = \frac{1}{l}\sum_{K=1}^{l} [\bar{C}_{kK} - C_{k\Delta}]^2 \quad , \tag{6.17}$$

and the standard deviation σ_k is defined as

$$\sigma_k = \sqrt{var(k)} \quad .$$

Increase in the number of data j in each discrete set will give better statistics for the defect correlation function due to the assumptions of the central limit theorem. The standard deviation however will be affected by the lack of statistical independence.

6.3.2 Fitting of correlation function

The correlation function derived from the simulated data can be fitted to Gordon's diffusion models, preferably the M-diffusion model as discussed before. In the fitting program, the maximum likelihood estimation of the model parameter τ is calculated by minimising the quantity χ^2, one of the so-called *least-squares*, within the iteration loop, where χ^2 is defined [92] as

$$\chi^2 \equiv \sum_{k=1}^{N} \left(\frac{C(t_k) - f(t_k : \tau)}{\sigma_k} \right)^2$$

where $C(t_k)$ is the autocorrelation function data at time t_k $(= k\Delta)$, $f(t_k : \tau)$ is a model function with a decay coefficient τ at time t_k, and σ_k is the standard deviation of the data which gives weight to each point. Since the model functions use a reduced time unit $t^* = t\sqrt{k_B T/I}$ where k_B $(= 0.83147124$ amuÅ^{2}ps^{-2}K$^{-1})$ is the Boltzmann constant, T the temperature in Kelvin and I $(= 186.11$ amuÅ$^2)$ the moment of inertia of the defect linear molecule, the MD time for defect correlation functions must be changed to the reduced time unit.

During the iteration loop the value of τ changes by $\Delta\tau$ with a bisection method in which the sign of $\Delta\tau$ is changed when χ^2 increases and its value is halved when the sign of $\Delta\chi^2$ ($= \chi^2_{new} - \chi^2_{old}$) changes in order for the model function to converge to the data. Calculating the recursive routines of the model function at discrete times and interpolating them before the iterations can considerably reduce the time taken for the fitting process.

Goodness-of-fit is tested by the incomplete gamma function $\gamma(a, b)$ [92] which is defined for the *least-squares* fitting method as

$$Q = \gamma\left(\frac{N-2}{2}, \frac{\chi^2}{2}\right)$$

where the value Q represents fitting quality. In order for the goodness-of-fit to be believable, Q must be larger than 0.1. However, a simple measurement of the root-mean-square deviation, r.m.s.=$\sqrt{\langle\chi^2\rangle}$, will give a reasonable estimation of the fitting quality.

6.3.3 Space diffusion function

In order to observe the displacement of a molecule during the simulation, a function which analyses the displacement of the molecule from a reference position can be devised as a function of time. It is defined simply as a distance at t from an initial position $\vec{r}(0)$ at $t = 0$ and we shall call this the space diffusion function. If we let the initial position be zero, the function $r(t)$ is defined as

$$r(t) = \sqrt{|\vec{r}(t)|^2} \quad .$$

The function enables us to study translational diffusion of a molecule from its reference position at t=0. If there was a sudden increase in the function over a short time, it would mean that the molecule has displaced by a significant distance during the time.

6.4 Simulation Detail

In order to investigate reorientational motions, a system is prepared with SF_6 host molecules of spherical top symmetry within which a small number of defect solute linear molecules are included. The system is set up to display the relevant physical phenomena of molecular reorientational motions rather than being a representation of a particular system in detail. As studied previously, the defect simulation program used in chapter 5 requires a little modification for the present study, mainly for recording orientational data as a function of time for both the host and the defect. In the simulation program of SF_6 molecule system developed for chapter 5, it is simply a time recording of quaternions of a specific set of molecules.

Since the system is found to be easily supercooled in computer simulation, it is therefore best to warm up the system from the crystalline phase to the liquid through the plastic crystalline phase rather than to freeze from the liquid to the plastic crystal. The system of 1024 SF_6 molecules with eight linear defects is prepared at 100K as a perfect bcc lattice with a given molecular number density ($Å^{-3}$) according to table 5.2. Only a small number of defects are included in the host system so that interaction between defect molecules is minimised. The description for the linear defect molecule is available in the previous chapter. Defects are chosen at random sites and the distances between defects are monitored to ensure they are well distributed and not too close. The system is equilibrated at 100K and warmed up to 230K at the rate of 0.2K/ps. At every 10K temperature step, a sample is taken to equilibrate at that temperature for 400ps and simulated for a further 400ps (which is equal to 40000 MD steps since 1 MD step used in the present study is again 0.01ps). Molecular orientations are recorded as a function of time at every two MD steps.

Table 6.1: Comparisons of the classical model $C_c(t)$ (second moments only), Gordon's M-diffusion model, and the simulation results at various correlation times t=0.1ps, 0.2ps, and 0.4ps for three different temperatures, 100K for the crystal, 170K for the plastic crystal, and 230K for the liquid. $C_c(t)$ is calculated with I=186.1411 amu Å^2 and k_B=0.83147124 amu Å^2 ps^{-2} K^{-1}.

t	T	$C_c(t)$	M-diffusion model	simulation results
0.1ps	100K	0.995(5)	0.995(5)	0.996(0)
	170K	0.992(4)	0.992(2)	0.992(9)
	230K	0.989(7)	0.989(6)	0.990(0)
0.2ps	100K	0.982(1)	0.982(2)	0.984(5)
	170K	0.969(6)	0.969(9)	0.973(7)
	230K	0.958(9)	0.959(5)	0.963(1)
0.4ps	100K	0.928(5)	0.930(2)	0.953(2)
	170K	0.878(5)	0.883(3)	0.917(9)
	230K	0.835(6)	0.844(3)	0.882(6)

6.5 Results

6.5.1 Very short time regime

The dipole correlation function of a classical linear molecule is given [93] in a power series as

$$C_c(t) = \langle \hat{u}(0) \cdot \hat{u}(t) \rangle = 1 - \left(\frac{k_B T}{I}\right) t^2 + \left[\frac{1}{3}\left(\frac{k_B T}{I}\right)^2 + \frac{1}{24 I^2}\langle (O\Phi)^2 \rangle\right] t^4 + \cdots$$

where $\hat{u}(t)$ is the unit vector of the molecule, k_B is the Boltzmann constant, T is the temperature, I is the moment of inertia of the molecule, and $\langle (O\Phi)^2 \rangle$ is the equilibrium averages of the mean square torque on a molecule due to its neighbours where Φ is the potential. The form of the correlation function for small t is mainly affected by the second term on the right (second moment) which only depends on the temperature and the molecular moment of inertia. The classical invariance of the second moment provides a method to test if the spectral distribution was measured over a sufficiently wide range of frequencies.

The dipole correlation function $C_c(t)$ of a classical linear molecule with only the first and second terms is compared with simulation results of defects together with Gordon's

M-diffusion model of the free linear rotor in tables 6.1. Three independent correlation functions at each temperature show little variation at short correlation time t=0.1ps. As the time increases to 0.2ps and 0.4ps correlation functions of the M-diffusion model and the simulation result deviate and both lie above the classical model. This result shows Gordon's M-diffusion model function is properly analysed and our simulation result is promising. Since intermolecular interactions come into play with the t^4 term (fourth moments) and have the effect of decreasing the decay of $C_c(t)$ with time, the reorientational correlation function for interacting molecules initially will lie above that for free molecules.

Correlation functions of SF_6 host molecules as a function of reduced time scale $t^* = t\sqrt{k_B T/I}$ where t is the MD time in ps, k_B is the Boltzmann constant, and T is the temperature, analysed from the simulation results are presented in figure 6.4 for various temperatures from 100K (top) to 230K (bottom) at 10K increments. The reduced time equals MD time at about T=224K. All the correlation functions in the figure are drawn with enough statistics. They show monotonic temperature dependence as expected; correlation functions of SF_6 molecules decrease as the temperature increases. This result is consistent with the previous experimental NMR measurements for a pure cyclohexane sample by O'Reilly et al. [76] in which monotonic temperature dependence of the rotational correlation time of cyclohexane was observed. There are two large gaps in between 120K and 130K, and between 210K and 220K where the crystal $\rightarrow$ plastic crystal and the plastic crystal $\rightarrow$ liquid phase transitions occur respectively. Host correlation functions therefore clearly identify the two phase transition temperatures. It is noted from the figure that the correlation function at 150K is close to that of 160K.

In order to analyse the correlation functions of the simulation results, they are fitted with our modified M-diffusion functions for the spherical top molecule by least-squares after the calculation of a set of Θ-functions for steps of τ. The fitting results for τ are given in table 6.2 for the 14 temperatures with root-mean-square deviations. The fact

that the initial curve of all correlation functions depends only on the kinetic motion of molecules rather than intermolecular interactions, the small statistical errors in the short time scale will result in an excessive weight on initial data points. In the fitting process therefore, each data point was equally weighted to investigate overall features of the correlation function.

At the lowest temperature, where molecules are closest together, τ^{-1} suggests around 144±12 collisions in the reduced time of 3.5, and therefore n in equation 6.4 has to be about 200 for the theoretical functions to be accurate. As the minimum required for n increases with the length of the time span the Θ-function accuracy diminishes with reduced time t^*, resulting in a systematic reduction of $C(t)$ with t. To minimise this systematic error the fitting is terminated at t^*=1.5. The fitting results show that the best fits are obtained for the plastic phase in the higher temperature range. Comparisons of our model function of the spherical top molecule with the MD simulation results are given in figure 6.5 for three different phases, the crystal at 110K, the plastic crystal at 170K, and the liquid at 230K. As shown in the figure, fittings of the MD results are very satisfying for the crystal and the plastic crystal. In both cases, the fitted model function starts above the simulation result and ends below at t^*=1.5. This is consistent with the trend of systematic error in the theoretical function and shows that the τ values might be estimated slightly too low. However for the liquid phase the Θ-function starts below the MD result and ends above at t^*=1.5, and is in a range of τ for which the Θ-function is unlikely to be inaccurate. This suggests that the fit is sufficiently poor that the M-diffusion model would need some modification for this phase. In a further analysis with the J-diffusion model, we have found no advantage over M-diffusion.

6.5.2 Correlation function anomalies at the transitions

Plots of defect correlation functions at various temperatures from 100K to 230K as a function of reduced time are presented in figure 6.6 from the top to the bottom with

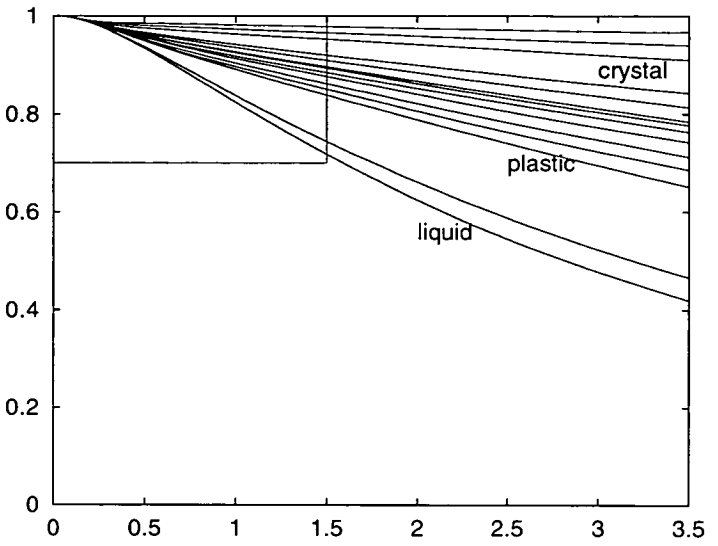

Figure 6.4: Correlation functions of SF_6 host molecules as a function of reduced time scale t^* analysed from the simulation results. The uppermost curve is of 100K and the temperature increases by 10K as it goes down.

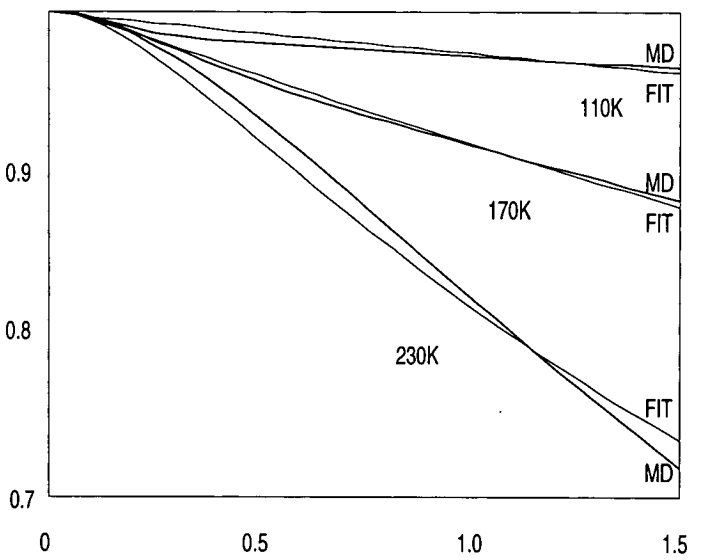

Figure 6.5: Correlation functions of SF_6 host molecules as a function of reduced time scale t^* taken from figure 6.4 (small box in the figure) at 110K, 170K, and 230K for the crystal, the plastic crystal, and the liquid respectively. In the figure, MD stands for the correlation function analysed from the simulation results and FIT stands for the fitting results.

a temperature step of 10K. The box within the figure is presented in figure 6.7. It is expected that as the temperature increases, the reorientational correlation function decreases. In the figure however, rotational diffusion appears to be nonmonotonic temperature dependent. Molecular reorientational motion at 140K surprisingly decreases below that at T=130K after the system has entered the plastic crystalline phase from the crystal. The correlation function at 130K starts above that of 140K as expected, and crosses over to below at about t=0.24ps. It then again crosses over to above the correlation function at 140K at about t=3.62ps and continues beyond t = 3.62ps in a manner closely similar to the other functions in the crystal regime. It suggests that even after the transition to the plastic phase has happened, some defect molecules are caught again in certain orientations which slow down reorientational motion at 140K causing the correlation function at 140K to lie above the correlation function at 130K within the time regime t <3.62ps. The crossover between these two correlation functions at 130K and 140K suggests that they follow different reorientational diffusion motions. It is noted that the correlation function at 130K is similar to those at 100K, 110K, and 120K which are in the crystalline phase. When just plastic, 140K, there is a range of t (0.24–3.62ps) where the correlation function at 140K is higher than that at 130K, but it does fall off at t >3.62ps more than the crystal correlation function, and is consistent with those plastic phase correlation functions at 150K and over. We note that for very short time regime the intermolecular interactions are not so important, and all the correlation curves are in the expected order due to the fact that reorientation motion is dominated by only the temperature and the moment of inertia of molecules. Therefore, it is believed that the behaviour of the correlation curve at 140K in the time regime (0.24ps < t < 3.62ps) is deeply related to the interactions with host molecules, and the greater freedom of the host molecules at higher temperatures tends to reduce the extra space enjoyed by the smaller defect molecules, which are substitutional, but for longer times (t > 3.62ps) the extra host motion does cause greater decorrelation for

the defects.

A rapid reorientational diffusion occurs again as the system melts at about 220K. The correlation function at 210K appears to be starting above that of 220K and then crosses over the correlation function of 220K at about t=1.95ps. It then again crosses over that of 220K at about t=3.0ps. It shows that a lower temperature plastic crystalline phase (210K) has more reorientational diffusion motions at a short time regime ($t <$ 3.0ps) than a higher temperature liquid (220K). The argument made for the anomaly at 140K is again possible for the anomaly at 210K that the time regime 1.95ps $< t <$ 3.0ps shows significance of interactions of defect molecules with host molecules. Long time reorientational diffusion motion of defects is limited by host motion resulting in overall increase of correlation function. This phenomenon is consistent with the experimental observations (reproduced in figures 6.8 and 6.9) reported by Edington et al. [75] from the Raman scattering measurement of CS_2 tracer solution within cyclohexane molecule system. In the experimental results, CS_2 tracer molecules show rapid reorientational diffusion at short time regime as the system is cooled down to the plastic crystalline phase from the liquid, showing a nonmonotonic temperature dependence. It is noted from the experimental results that the correlation functions of CS_2 molecule show a more rapid decrease than those of the MD results due to the fact that CS_2 tracer molecule is relatively much lighter than our model defect molecule.

It is observed in the very short time regime $t <$ 0.25ps that defect correlation functions at various temperatures show a monotonic temperature dependence. This result agrees with the analysis of the second moment of the classical model which is characterised only by temperature and moment of inertia as discussed at the beginning of this section giving a continuous decrease of correlation functions with increasing temperature. In the long time regime $t >$ 3.6ps observed up to t=5.0ps, the correlation functions show again a monotonic temperature dependence except for the correlation function at 160K (see section 6.5.3). There is similarity of all "crystal curves", all

Table 6.2: The MD simulation results are fitted by least-squares with the Gordon's M-diffusion model for SF_6 host and defect molecules for the 14 temperatures. The fitted values τ are presented with the r.m.s. deviation.

phase	T(K)	$\tau(SF_6)$	rms	τ(tracer)	rms
liquid	230	0.201	0.0133	0.346	0.0043
	220	0.176	0.0107	0.284	0.0043
plastic	210	0.101	0.0016	0.286	0.0033
	200	0.094	0.0011	0.282	0.0030
	190	0.086	0.0023	0.273	0.0045
	180	0.076	0.0029	0.250	0.0038
	170	0.071	0.0029	0.232	0.0047
	160	0.065	0.0044	0.248	0.0049
	150	0.062	0.0039	0.215	0.0056
	140	0.054	0.0049	0.176	0.0047
	130	0.050	0.0057	0.193	0.0074
crystal	120	0.034	0.0074	0.152	0.0097
	110	0.028	0.0036	0.128	0.0123
	100	0.023	0.0052	0.104	0.0135

"plastic" are consistent, all "liquid" are similar, but all three groups are different for long t^*. Eventually, the defect correlation functions are expected to approach zero since the correlation values are distributed between +1 and -1 and the average of the values over a long period of time would converge to zero. The correlation functions in the liquid would approach zero more rapidly than those in the plastic crystal due to random reorientational motions of defect molecules.

Fittings of reorientational correlation functions by Gordon's M-diffusion model for the defect are presented as "tracer" in table 6.2. In the table, the best fits are in general obtained in higher temperature range of the plastic phase which are consistent with the fitting results of the host molecule. Poorer fitting results are however found in the crystal regime rather than the liquid. There also appear nonmonotonic increases of τ as the temperature increases, especially at 130K, 160K, and 210K. They are plotted in figure 6.10 to show more clearly. The figure shows clear decreases of the r.m.s. deviation as the temperature increases and also three different temperatures within the plastic

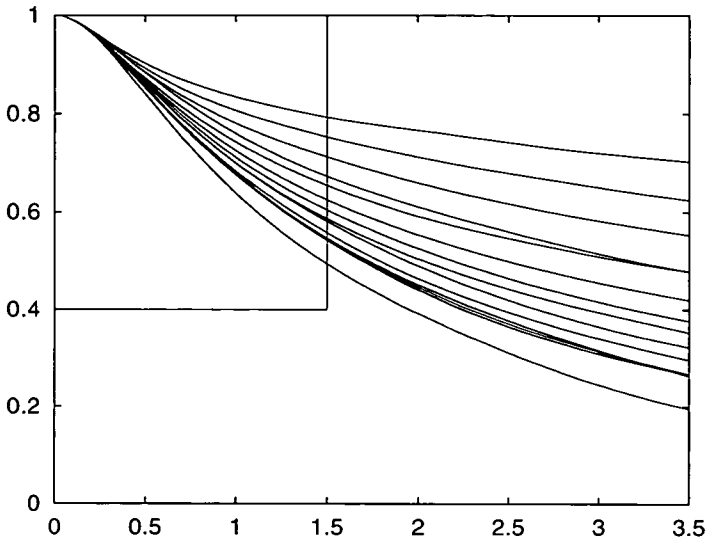

Figure 6.6: Correlation functions of the linear defect molecules as a function of reduced time t^*. From top to bottom at t^*=2.5 the temperatures are 100K, 110K, 120K, 140K, 130K, 150K, 170K, 160K, 180K, 190K, 220K, 200K, 210K, and 230K.

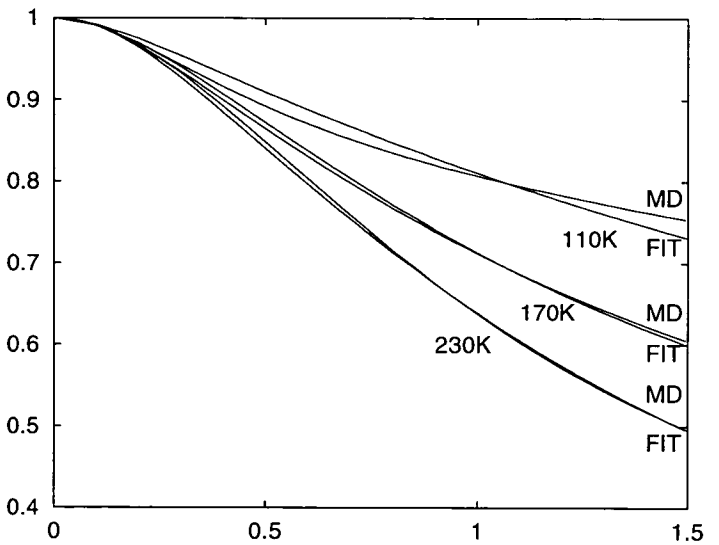

Figure 6.7: Correlation functions of defect molecules as a function of reduced time scale t^* taken from figure 6.6 at 110K, 170K, and 230K for the crystal, the plastic crystal, and the liquid respectively. They are fitted by Gordon's M-diffusion model. In the figure, MD stands for the correlation function analysed from the simulation results and FIT stands for the fitting results by the model function.

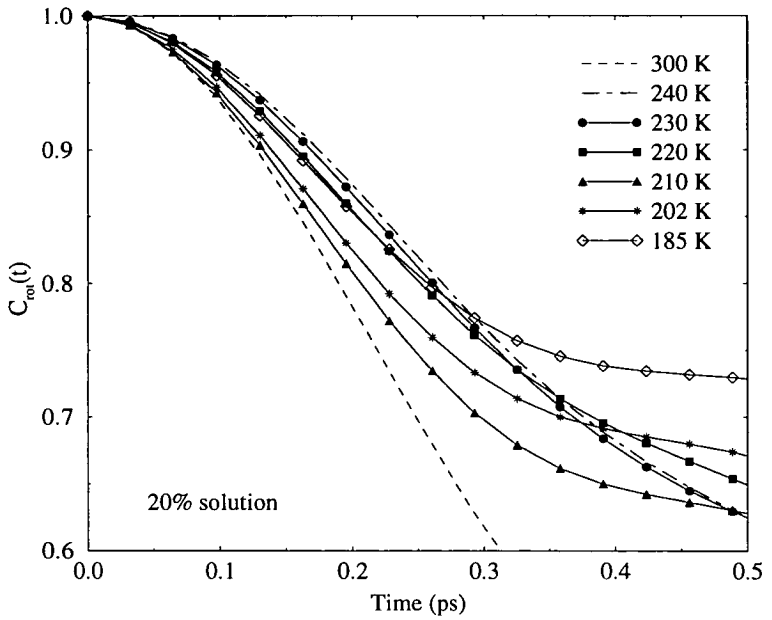

Figure 6.8: In the short time ($t < 0.5$ps) regime, the reorientational correlation functions $C_{rot}(t)$ for a 20% solution of CS_2 in cyclohexane.

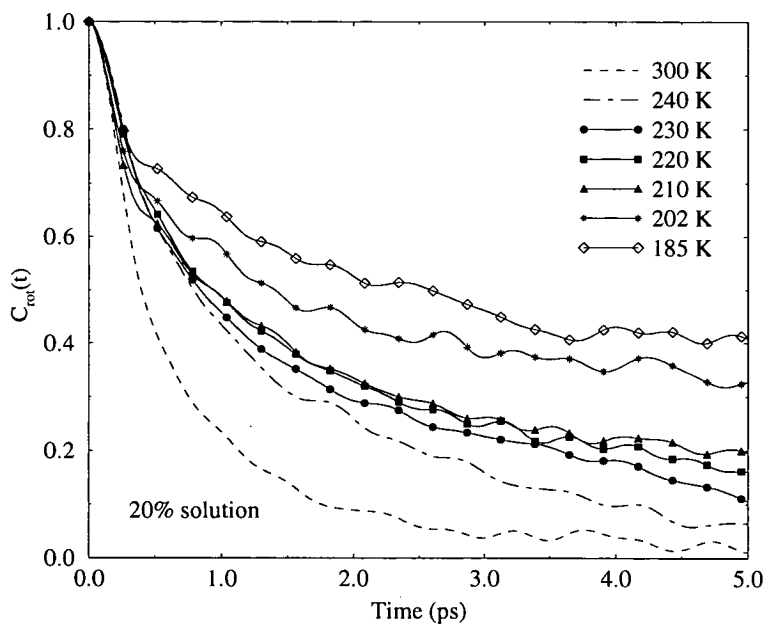

Figure 6.9: In the long time ($t \gtrsim 0.5$ps) regime, the reorientational correlation functions $C_{rot}(t)$ for the same system as figure 6.8. (Figures 6.8 and 6.9 are reproduced from the experimental report by Edington et al. [75] with permission).

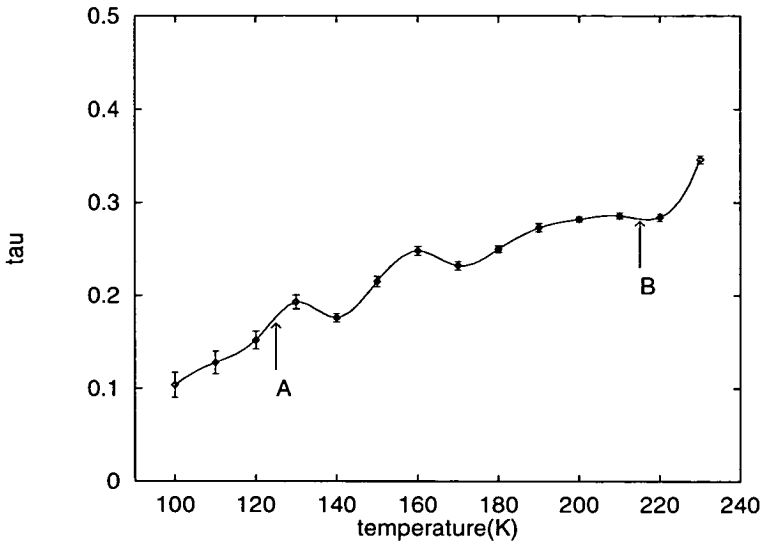

Figure 6.10: Fitted tau values with errorbars as a function of temperature. They are fitted by the spline-fit and plotted with rms as errorbars. Two arrows A and B show two transition points, crystal $\rightarrow$ plastic crystal and plastic crystal $\rightarrow$ liquid respectively.

crystalline phase showing high increases of τ. Fitted M-diffusion functions (FIT) are plotted with the MD simulation results (MD) in figure 6.7 for three different phases at 110K for the crystal, 170K for the plastic crystal, and 230K for the liquid. The figure shows good approximations for the plastic crystal and the liquid. In the figure, all three fitted theoretical model functions start below the MD results in short time scale and end above at t^*=1.5 showing that the τ values might again be estimated slightly too high. Although the fitting results are poorer in the crystalline phase, the theoretical model function, in general, shows a good agreement with the MD results.

Comparison of correlation functions are made for the stable plastic crystalline phase and the metastable phase (liquid) at the same temperature where the correlation function of a metastable liquid is produced by supercooling the liquid at 210K. Two correlation functions are presented together in figure 6.11 where the top figure is the comparison of the defect and the bottom is for the host. In the comparison of two phases of the host molecule, the liquid (meta-stable) shows an overall speeding up of

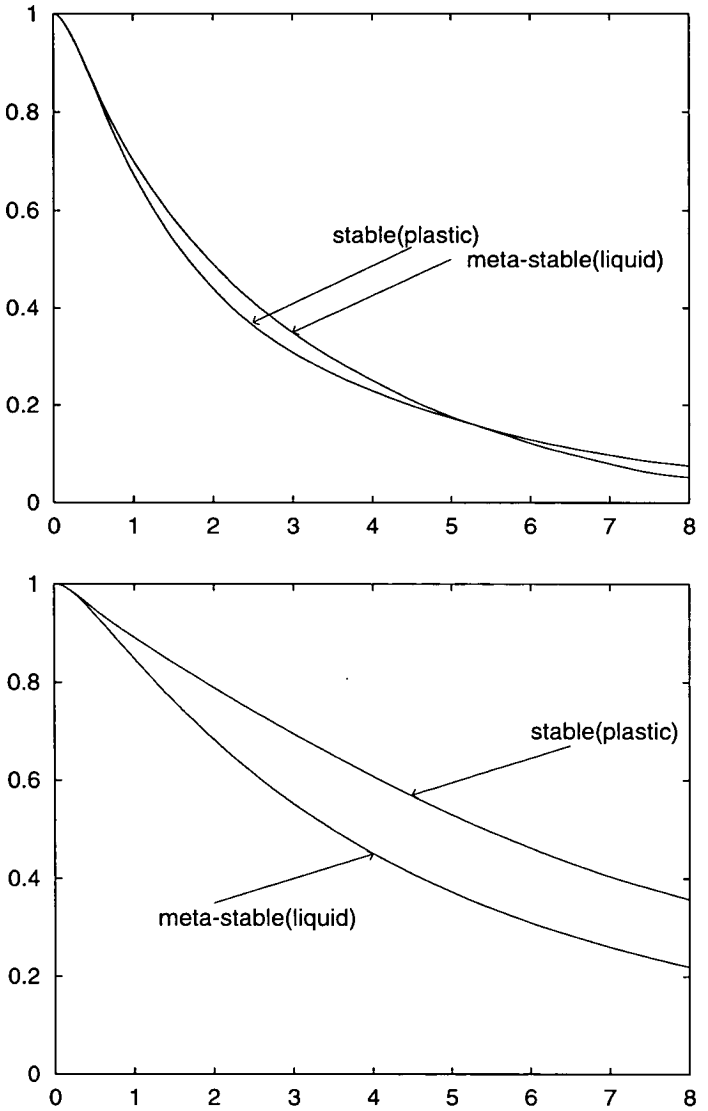

Figure 6.11: Comparison between two correlation functions of the stable (plastic) and the meta-stable (liquid) phases at the same temperature 210K as a function of reduced time t^* for the defect molecule (top) and the host (bottom).

reorientational diffusion motion against the plastic crystalline phase (stable). This is an expected result since the disordered liquid phase has more local free volume. Referring to molecular number densities analysed, ρ_s=9.54451×10^{-3} Å^{-3} for the system in the stable plastic phase and ρ_m=7.77519×10^{-3} Å^{-3} for the metastable liquid, this extra free volume allows molecules to rotate more freely in the liquid phase than in the ordered plastic phase. However, it is not always the case for the linear defect molecules as shown in the top of figure 6.11. There is a rapid reorientational diffusion in the correlation function of defects in the stable plastic crystalline phase in the time regime up to t^*=5.2. Beyond this regime, the correlation function lies above the meta-stable liquid curve. Host motion seems to hinder long time reorientational diffusion of defects in the stable plastic phase. It suggests that there are short time scale reorientational motions for the linear defects possibly by rapid kicking by neighbouring host molecules.

6.5.3 The 160K anomaly

There is apparent anomaly in the reorientational diffusion motion within the plastic crystalline phase. According to figure 6.6, the defect correlation curve at 170K appears to be above the 160K curve. The correlation function at T=160K seems to be staying below the curve at T=170K even beyond $t^* = 3.5$, unlike those found at the two transition temperatures. It is also noticed that overall shapes of both defect correlation functions at 160K and 170K are almost the same as each other, as expected since they follow a similar reorientational diffusion motion. The anomaly is therefore assumed to be different from those in the other two regimes.

In order to see more clearly, the values of the correlation functions for all temperatures at $t^* = 3.5$ in figure 6.6 are plotted as a function of temperature and fitted by the spline-fit as given in figure 6.12. The figure shows a clear non-monotonic temperature dependence. Within the plastic crystalline regime (130K $\sim$ 210K), there is a very noticeable depression at about 160K followed by a hump at 170K. It coincides with the speeding up of reorientational motion at 160K as seen in figure 6.6 and suggests that

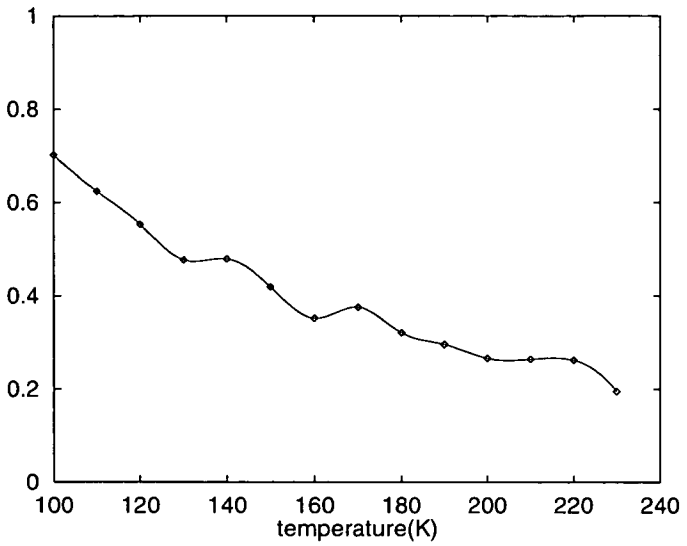

Figure 6.12: The values of the correlation functions of the defect taken from figure 6.6 at t^*=3.5 as a function of temperature. They are fitted by the spline-fit. There are transition temperatures in between 120K and 130K, 210K and 220K for the crystal → plastic crystal and the plastic crystal → liquid respectively.

there exists a definite physical phenomenon around this temperature.

Average molecular number densities are plotted in figure 6.13 at various temperatures in order to investigate whether or not changes of local free volume can be identified by density. The figure clearly identifies two first order phase transitions in between 120K and 130K for the crystal → plastic crystal, 210K and 220K for the plastic crystal → liquid. Within the plastic crystalline temperature regime, the density decreases gradually as temperature increases. However, there is no sign of density change around 160K where an abnormal rapid reorientational diffusion was observed.

Standard deviations estimated from the root-mean-square average over 100ps of molecular number densities are given at various temperatures in figure 6.14. The figure represents statistical variations of densities. Points of standard deviations plotted in the figure are fitted by the spline-fit. It shows that active volume fluctuations will result in high statistical variations. The figure therefore allows us to examine if there exist such activities in the system. At T=130K, there is a high increase of such volume

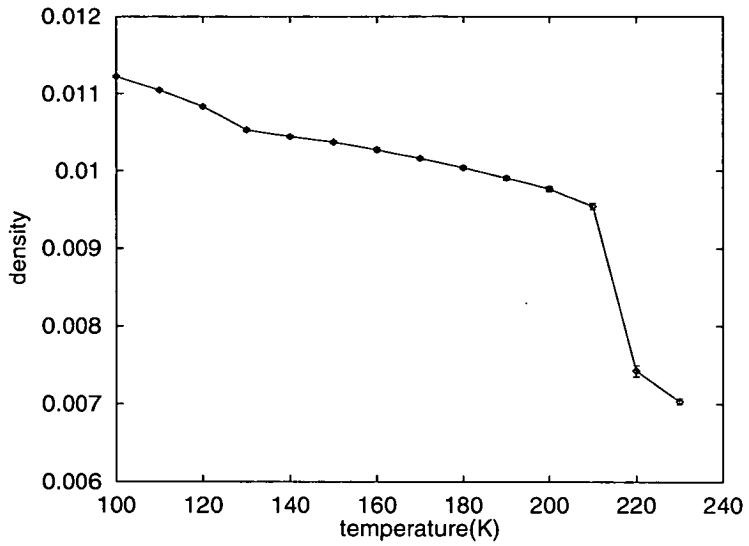

Figure 6.13: The root-mean-square average of molecular number density ($Å^{-3}$) over 100ps. There are two first order phase transitions; one between 120K and 130K for the crystal $\rightarrow$ plastic crystal phase transition, the other between 210K and 220K for the plastic crystal $\rightarrow$ liquid.

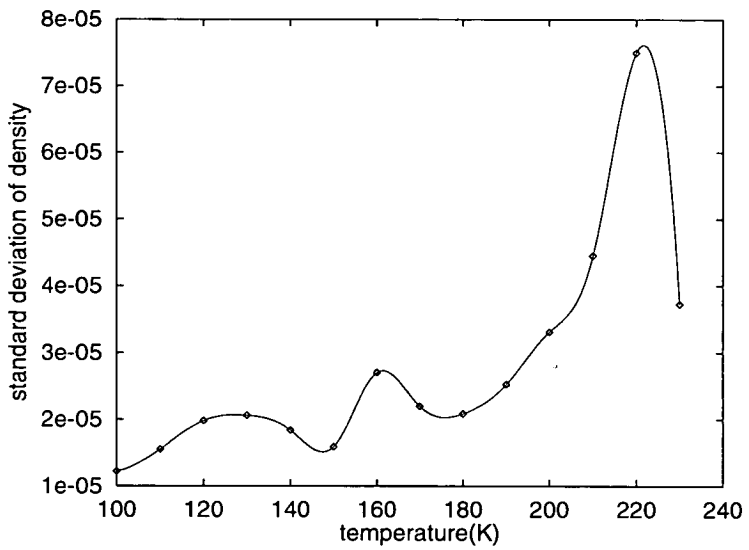

Figure 6.14: Standard deviation estimated from the root-mean-square average of the molecule number density over 100ps. They are fitted by the spline-fit.

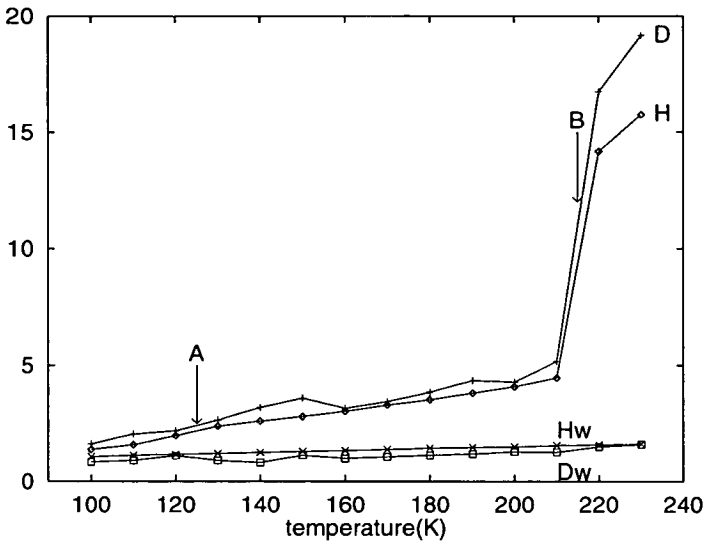

Figure 6.15: Average space diffusion in units of Å of defect (D) and host (H) after 100ps together with average angular velocities in units of ps^{-1} of defect (Dw) and host (Hw). A and B mark two phase transition temperatures; the crystal $\rightarrow$ plastic crystal (A) and the plastic crystal $\rightarrow$ liquid.

fluctuations. This is the temperature where the system enters the plastic crystalline phase in which SF_6 molecules become orientationally disordered whereas they are translationally ordered. Therefore, the increase in volume fluctuations is assumed to be a result from the orientational disorder of host molecules. Such high volume fluctuations increase dramatically at about 220K where the system melts. As previously observed in figure 6.12, there is again a high increase of volume fluctuation activity at 160K within the plastic crystalline phase. Such volume fluctuations are direct evidence of high reorientational motion.

The average space diffusion for periods of 100ps are given in figure 6.15 for the defect and the host marked in the figure as D and H respectively. In the figure, two phase transition temperatures are marked as A and B for the crystal $\rightarrow$ plastic crystal and the plastic crystal $\rightarrow$ liquid respectively. Within the plastic phase, the host space diffusion increases monotonically with increasing temperature whereas the defect space diffusion changes nonmonotonically. The host space diffusion line (H) in figure 6.15 is

inversely proportional to the density line in figure 6.13 showing consistency between the volume expansion and the host space diffusion. The root-mean-square deviations in the average defect space diffusion, however, are found to be statistically very unreliable due to the small configuration number of defect molecules. The humps of the average defect space diffusion do not coincide with the abnormality at 160K and 170K, and are within statistical errors. It suggests that the abnormality within the plastic crystalline phase is not involved either with the space diffusion of host or with of defect. Average angular velocities at various temperatures are also given in the same figure showing monotonic increase with increasing temperature, consistent with the rotational kinetic energy increasing monotonically as temperature increases. It is noted that volume increase of the system is closely proportional to the increase of reorientational rate of SF_6 showing a monotonic increase with increasing temperature (G. S. Pawley private communication). Therefore, the anomaly at 160K is irrelevant to the reorientational rate of host molecules. In the figure no abnormality is identified within the plastic crystal regime. Defect average angular velocities again show poor statistics due to the lack of configuration number, and do not help in the understanding of the abnormality at 160K.

In figure 6.16, 6.17, and 6.18, continuous defect orientations are plotted for 100ps at every two MD steps at various temperatures by the dotplot representation (refer to section 2.10.2) to show time evolution of defect reorientations. Throughout the three figures, the eight defects numbered from 1 to 8 are placed in columns with increasing temperature from left to right.

The crystalline phase between 100K and 120K in figure 6.16 shows multiple sites of localised reorientational motion. Typical examples are found from defect #2 and #5. In this phase, there are also a few molecules showing a very localised reorientational motion about a particular orientation such as defect #1, #7, and #8. Although a number of defects show a certain degree of active reorientational motion, in general

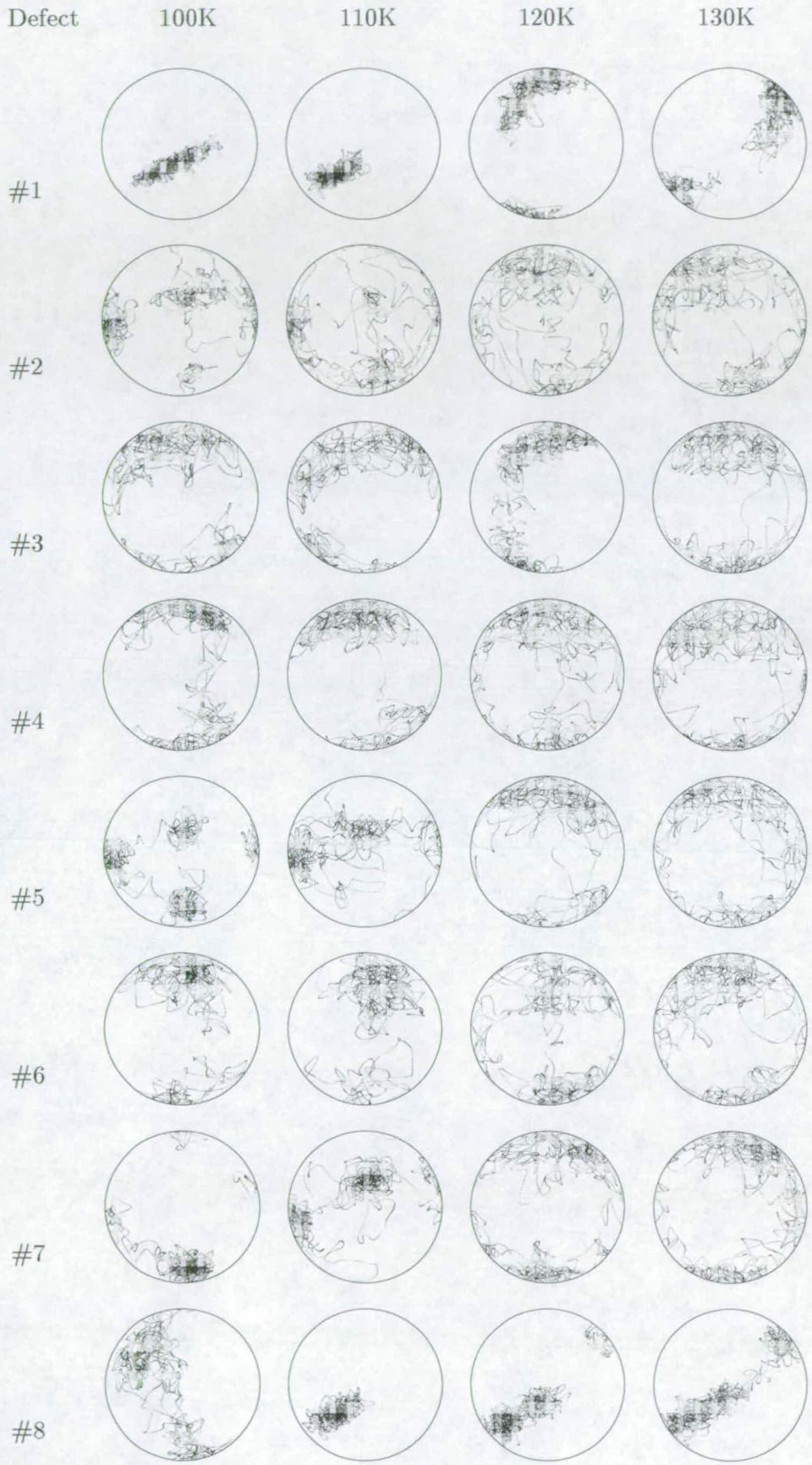

Figure 6.16: Dotplots of eight defects for 100ps. There is a crystal → plastic crystal phase transition in between 120K and 130K.

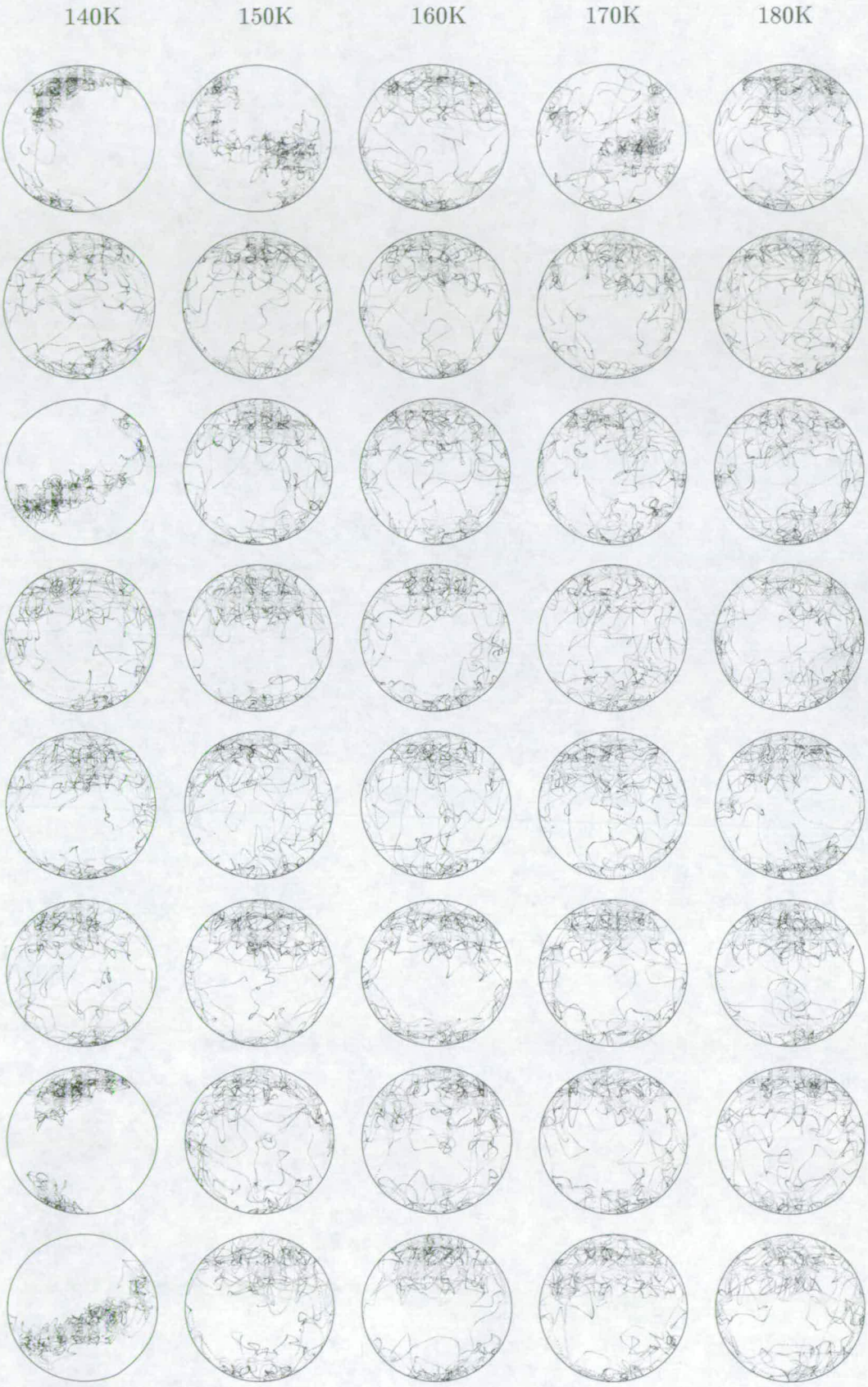

Figure 6.17: Dotplots of eight defects for 100ps in the plastic crystalline phase.

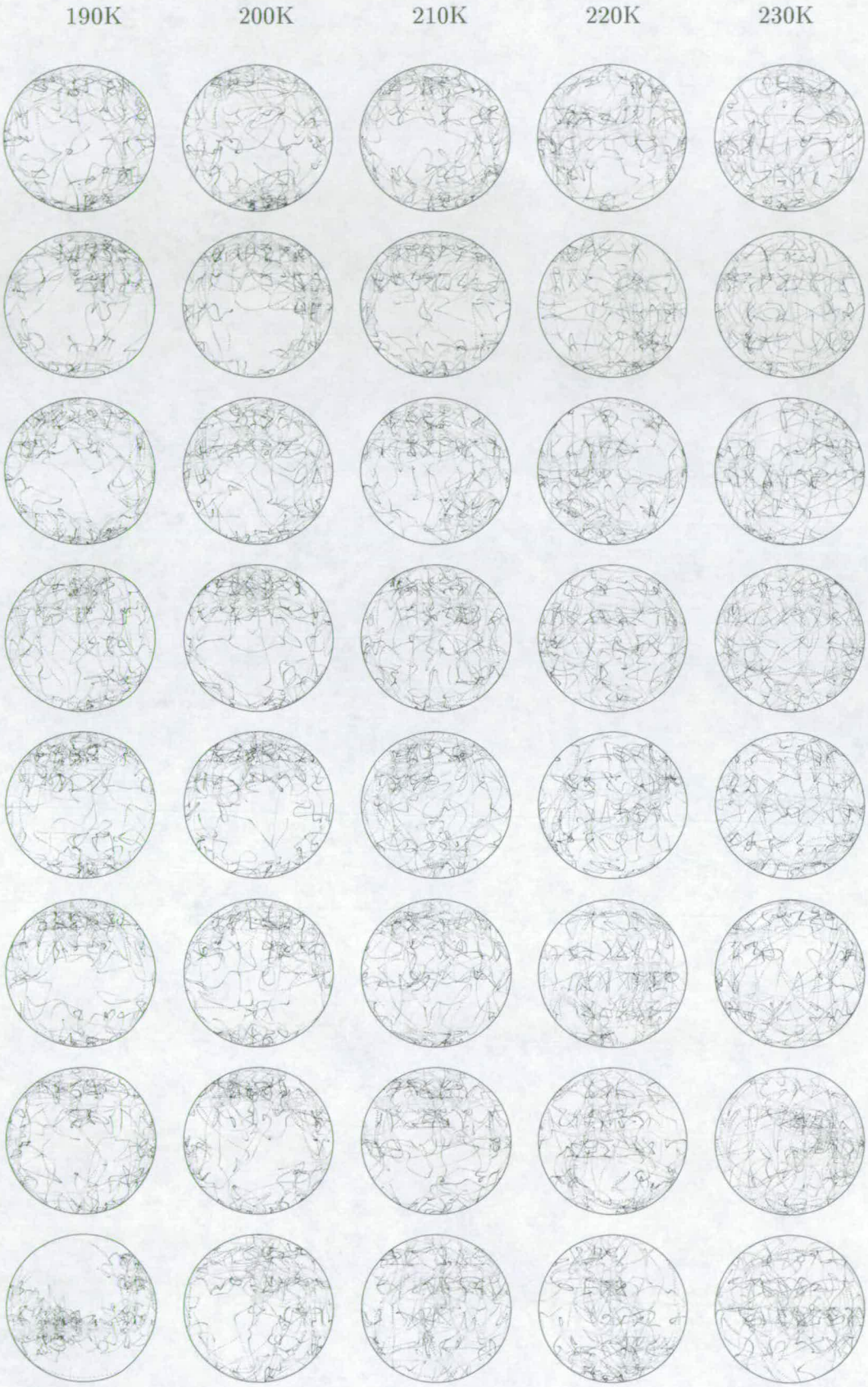

Figure 6.18: Dotplots of eight defects for 100ps. There is a plastic crystal → liquid phase transition in between 210K and 220K.

they exhibit a large "exclusion zone" which is not visited by defects.

As the system enters the plastic crystalline phase, the multiple sites of localised reorientational motion as found in the crystal clearly disappear. There are a few defects which still persist with very localised reorientational motion even after the phase transition to the plastic crystal. However, their reorientational motion in general differs from those found in the crystal by the extent of local sites. Overall areas of the exclusion zone are smaller than those found in the crystal but are still in evidence. The localised motion in the plastic crystal is assumed to be due to the reorientational motion of host molecules which is characterised by jumps to other orientational sites in the time scale $\sim$1ps. Between these orientational jumps of host molecules, defects have a certain degree of probability of being in a particular orientational site although it is less defined compared to that in the crystal due to the orientational disorder of the host molecules. Those localised motions disappear mostly at about 160K.

However, a local site for defect #1 reappears at 170K. This corresponds to the observation of abnormality at 170K where the defect correlation function at 170K was found to be above that at 160K. It differs from the crossovers between correlation functions which happened in the two phase transition regimes within short time regime. It is believed according to dotplots of defect #1 at 150K, 160K, and 170K that the abnormality at 160K is statistically insignificant due to the fact that the defect correlation functions are statistically averaged over a long period of time rather than a large number of defect molecules, during which defect #1 would have given a large contribution to the correlation function at 170K by remaining in a site significantly more constant than the average site.

In the liquid as shown in figure 6.18 at 220K and 230K, dotplots show random reorientational motions as expected for the liquid. There are no orientational excluded zones in the dotplots as distinct from those in the plastic crystal where a certain degree of orientational exclusion still exists ever close to the liquid phase.

6.6 Discussion

In the fitting analysis, Gordon's diffusion models, particularly M-diffusion, were found to be very useful for systematic analysis of correlation functions although the models would need some modifications for certain phases, such as the liquid for the spherical top analysis and the crystalline for the linear top.

It was found that the anomaly between 160K and 170K was different from those found at the two phase transitions. We ascribe this anomaly to poor statistics, this 170K result being skewed as one of the defect molecules was in a site which remained significantly more constant than the average site. Space diffusion, volume change, and reorientational rate of host molecules with increasing temperature were proven to have had no connection with this apparent anomaly.

From the simulation study on binary mixtures of SF_6 host molecules and linear defects, it was found that reorientational motion of the host increases as the temperature of the system increases showing monotonic temperature dependent lowering of host correlation functions. In the direct comparison of two different phases of the host system at the same temperature of 210K, at which metastable liquid phase obtained by supercooling was compared with the stable plastic crystalline phase, it was also observed that the reorientational correlation function of the stable phase of the host lies above the metastable liquid as expected. These results are consistent with previous experimental observations based on NMR and optical spectroscopic measurements in which orientational relaxation times exhibited a continuous monotonic increase across the liquid $\rightarrow$ plastic phase transition regime [76, 94].

Comparison of defect correlation functions of the stable plastic phase and the metastable liquid showed that there was a rapid reorientational diffusion motion in the stable plastic phase below the metastable liquid. We also found that defect correlation functions at various temperatures show nonmonotonic temperature dependence. Particularly, the correlation function at 210K in the plastic crystalline phase decays

more rapidly below that of 220K in the liquid in the short time regime whereas it stays above in the long time regime. These results agree with the observation of a strange reorientational diffusion behaviour of solute tracer molecule in the liquid → plastic crystal phase transition regime from Raman scattering measurement by Edington et al. [75] in which correlation functions of CS_2 solute molecule were found to be nonmonotonic temperature dependent. The same feature was found at 130K immediately after the phase transition to the plastic crystal showing rapid reorientational diffusion motion in the short time regime. The behaviours in the short time regime observed at the two phase transitions are believed to be that interactions with host molecules are important in the plastic crystalline phase which have resulted in increase of short time reorientational motion while long time diffusions are hindered by host motion.

In the plastic phase the host molecules tend to undergo orientational "jumps" between orientations that are symmetry related. A defect molecule is assumed to be surrounded by host molecules which therefore form a "site". This site does not change when a host molecule jumps, except during the brief time of the jump. During this brief time the defect molecule might be disturbed by more than the usual thermal motion, becoming decorrelated more quickly than would be expected for a liquid for that temperature. This is on a time-scale determined by the jump time (~1ps) and the jump probability. The site for the defect does persist for a time much longer than the jump time because the host molecules forming the site tend to return to the same orientations after jumps. This means that there are orientations for the defect in any particular site which are not visited as often as they would be if the host system were liquid, and therefore the defect correlation function, although falling more rapidly than the liquid in the short time regime, falls less rapidly over a long time, this "long time" being determined by the constancy of the site. Site constancy can be seen in the long period connected defect dotplots.

6.7 Conclusion

Gordon's theoretical diffusion model for the linear top molecule is found to have best fits in the plastic crystalline phase and the liquid whereas the MD result showed some degree of discrepancy in the crystalline phase with the model function. The extended version of the theoretical model developed for the spherical top molecule is found to have shown best fits in the crystalline phase and the plastic crystalline whereas the MD result fits rather poorly in the liquid. Therefore, each model function is not fully compatible with all the three phases and would need modification.

It is concluded that jump reorientational motions of host molecules are responsible for the rapid defect reorientational diffusion in the short time regime. The site does not change as a result of a host molecule jump. This therefore results in hindrance of long time reorientational diffusion of defects as shown by the defect correlation function.

In the present study, we have simulated a system in which a small number of linear defect molecules are included in SF_6 host system in order to investigate reorientational diffusion motion for both molecules to investigate strange reorientational diffusion motion of CS_2 solutes with cyclohexane observed from Raman scattering measurements by Edington et al. [75] in comparison with the previous NMR experimental measurements on a pure cyclohexane solvent sample by O'Reilly et al. [76]. We found that the simulated system accounts for all the major features of the experimental observations, such as an increase in the tracer molecule short-time reorientational relaxation rate at the liquid to plastic transition, and the presence of a long-time regime where the liquid state relaxation rate becomes faster than that in the plastic phase.

Today, a simple computer simulation can run on a small personal computer though it was once a challenge even a decade ago. The computer simulation technique is found to be very successful in various scientific areas and the computer itself is now ever more powerful and will develop even more in the future. Although the present study of molecular reorientational motion was done for a rather simple model, more detailed

models of very complex systems can easily be studied in the near future. These studies demanding computing power in both simulation and analysis will yield a considerable benefit for understanding of experiment.

Sulphur Hexafluoride (SF_6)

The sulphurhexafluoride molecule has an octahedral arrangement and there are six fluorine atoms placed at each vertex and one sulphur atom at its centre. The bond length between the sulphur and fluorine atom is given as a=1.565Å [50] and the coordinates of six atoms are $(\pm a, 0, 0)$,$(0, \pm a, 0)$, and $(0, 0, \pm a)$. The mass of the molecule is in total 146 amu since the fluorine atom is 19 amu and the sulphur atom is 32 amu.

The inertia tensor is derived as follows,

$$\tilde{I} = \sum_i m_i \begin{pmatrix} y_i^2 + z_i^2 & -x_i \cdot y_i & -x_i \cdot z_i \\ -y_i \cdot x_i & x_i^2 + z_i^2 & -y_i \cdot z_i \\ -z_i \cdot x_i & -z_i \cdot y_i & x_i^2 + y_i^2 \end{pmatrix}$$

where m_i is the mass of atom i and x_i, y_i and z_i are the atomic co-ordinates relative to the molecule centre. The inertia tensor of sulphur hexafluoride is, therefore,

$$\tilde{I} = \begin{pmatrix} 186.1411 & 0.0 & 0.0 \\ 0.0 & 186.1411 & 0.0 \\ 0.0 & 0.0 & 186.1411 \end{pmatrix}.$$

Conversion factors used in simulations

UNITS

Quantity	Name	Symbol	Definition(SI)
Length	ångström	Å	$10^{-10}m$
Time	picosecond	ps	$10^{-12}sec$
Mass	atomic mass unit	amu	$1.6605 \times 10^{-27}kg$

CONVERSION FACTORS

$k_B = 0.83147124$ amu Å^2 ps^{-2} K^{-1}

1 Kcal Mol^{-1} = 418.674 amu Å^2 ps^{-2}

1 GPa = 60.22282 amu Å^{-1} ps^{-2} $\simeq 1 \times 10^4$ bar

Bibliography

[1] Becker, R. and W. Döring. Ann. d. Phys. **24** 719 (1935).

[2] Turnbull, D. and J. C. Fisher. J. Chem. Phys. **17** 71 (1949).

[3] Glasstone, S., K. J. Laidler, and H. Eyring (eds.). The Theory of Rate Processes. McGraw-Hill Book Company, Inc., New York (1941).

[4] Harrowell, P. and D. W. Oxtoby. J. Chem. Phys. **80** 1639 (1984).

[5] Oxtoby, D. W. J. Phys.,Condens. Matter **4** 7627 (1992).

[6] Oxtoby, D. W. Adv. Chem. Phys. **70** 263 (1988).

[7] Mandell, M. J., J. P. McTague, and A. Rahman. J. Chem. Phys. **64** 3699 (1976).

[8] Mandell, M. J., J. P. McTague, and A. Rahman. J. Chem. Phys. **66** 3070 (1977).

[9] Hsu, C. S. and A. Rahman. J. Chem. Phys. **70** 5234 (1979).

[10] Cape, J. N., J. L. Finney, and L. V. Woodcock. J. Chem. Phys. **75** 2366 (1981).

[11] Swope, W. C. and H. C. Andersen. Phys. Rev. B **41** 7042 (1990).

[12] Steele, W. A. J. Chem. Phys. **38** 2404 (1963).

[13] Steele, W. A. J. Chem. Phys. **38** 2411 (1963).

[14] Gordon, R. G. J. Chem. Phys. **44** 1830 (1966).

[15] Fixman, M. and K. Rider. J. Chem. Phys. **51** 2425 (1969).

[16] Pierre, A. G. S. and W. A. Steele. Phys. Rev. **184** 172 (1969).

[17] McClung, R. E. D. J. Chem. Phys. **57** 5478 (1972).

[18] Pierre, A. G. S. and W. A. Steele. J. Chem. Phys. **57** 4638 (1972).

[19] Hernández-Contreras, M. and M. Medina-Noyola. Phys. Rev. E **54** 6586 (1996).

[20] Coffey, W. T., P. M. Déjardin, and M. E. Walsh. J. Chem. Phys. **110** 5300 (1999).

[21] Rothschild, W. G. J. Chem. Phys. **57** 991 (1972).

[22] Fujara, F., B. Geil, H. Sillescu, and G. Fleischer. Z. Phys. B, Cond. Matter **88** 195 (1992).

[23] Jones, M. J., F. Guillaume, K. D. M. Harris, A. E. Aliev, P. Girard, and A.-J. Dianoux. Mol. Phys. **93** 545 (1998).

[24] Dreyfus, C. and C. Breuillard. Mol. Phys. **62** 1275 (1987).

[25] Heyes, D. M., M. J. Nuevo, J. J. Morales, and A. C. Bránka. J. Phys. Cond. Matter **10** 10159 (1998).

[26] Meyer, M., C. Marhic, and G. Ciccotti. Mol. Phys. **58** 723 (1986).

[27] Alder, B. J. and T. E. Wainwright. J. Chem. Phys. **27** 1208 (1957).

[28] Rahman, A. Phys. Rev. **136** 405 (1964).

[29] Lennard-Jones, J. E. Proc. Roy. Soc. (London) **A** 463 (1924).

[30] Verlet, L. Phys. Rev. **159** 98 (1967).

[31] Beeman, D. J. Comp. Phys. **20** 130 (1976).

[32] Evans, D. J. Mol. Phys. **34** 317 (1977).

[33] Parrinello, M. and A. Rahman. Phys. Rev. Lett. **45** 1196 (1980).

[34] Lees, A. W. and S. F. Edwards. J. Phys. C, Solid State Physics **5** 1921 (1972).

[35] Andersen, H. C. J. Chem. Phys. **72** 2384 (1980).

[36] Evans, D. J. and G. P. Morriss. Chem. Phys. **77** 63 (1983).

[37] Hoover, W. G. Phys. Rev. A **31** 1695 (1985).

[38] Schröder, T., R. Schinke, R. Krohne, and U. Buck. J. Chem. Phys. **106** 9067 (1997).

[39] Beck, T. L. and T. L. M. II. J. Chem. Phys. **93** 1347 (1990).

[40] Shimamura, S., S. N. Khanna, and P. Jena. Phys. Rev. B **40** 2459 (1989).

[41] Greig, D. W. and G. S. Pawley. Mol. Phys. **89** 447 (1996).

[42] Kittel, C. Introduction to solid state physics. John Wiley, New York (1971).

[43] Cohen, E. R. The physics quick reference guide. American Institute of Physics, Woodbury, New York (1996).

[44] Tanemura, M., Y. Hiwatari, H. Matsuda, T. Ogawa, N. Ogita, and A. Ueda. Prog. Theor. Phys. **58** 1079 (1977).

[45] Allpress, J. G. and J. V. Sanders. Aust. J. Phys. **23** 23 (1970).

[46] van de Waal, B. W. J. Chem. Phys. **98** 4909 (1993).

[47] van de Waal, B. W. Phys. Rev. Lett. **76** 1083 (1996).

[48] Farges, J., B. Raoult, and G. Torchet. J. Chem. Phys. **59** 3454 (1973).

[49] Fukano, Y. and C. M. Wayman. J. Appl. Phys. **40** 1656 (1969).

[50] Pawley, G. S. Mol. Phys. **43** 1321 (1981).

[51] Bartell, L. S. J. Phys. Chem. **99** 1080 (1995).

[52] Kinney, K. E., S. Xu, and L. S. Bartell. J. Phys. Chem. **100** 6935 (1996).

[53] Dove, M. T., G. S. Pawley, G. Dolling, and B. M. Powell. Mol. Phys. **57** 865 (1986).

[54] Powell, B. M., M. T. Dove, G. S. Pawley, and L. S. Bartell. Mol. Phys. **62** 1127 (1987).

[55] Dove, M. T., B. M. Powell, G. S. Pawley, and L. S. Bartell. Mol. Phys. **65** 353 (1988).

[56] Pawley, G. S. and G. W. Thomas. Phys. Rev. Lett. **48** 410 (1982).

[57] Dove, M. T. and G. S. Pawley. J. Phys. C, Solid State Phys. **16** 5969 (1983).

[58] Dove, M. T. and G. S. Pawley. J. Phys. C, Solid State Phys. **17** 6581 (1984).

[59] Hua, L. and G. S. Pawley. Z. Krist **202** 177 (1992).

[60] Fuchs, A. H. and G. S. Pawley. J. Physique **49** 41 (1988).

[61] Moon, C. and G. S. Pawley. J. Mol. Struct. **485-486** 479 (1999).

[62] Honeycutt, J. D. and H. C. Andersen. Chem. Phys. Lett. **108** 535 (1984).

[63] Honeycutt, J. D. and H. C. Andersen. J. Phys. Chem. **90** 1585 (1986).

[64] Erpenbeck, J. J. Phys. Rev. Lett. **52** 1333 (1984).

[65] Woodcock, L. V. Phys. Rev. Lett. **54** 1513 (1985).

[66] Heyes, D. M. Mol. Phys. **57** 1265 (1986).

[67] Gray, R. A., P. B. Warren, S. Chynoweth, Y. Michopoulos, and G. S. Pawley. Proc. R. Soc. Lond. A **448** 113 (1995).

[68] Evans, D. J. and B. L. Holian. J. Chem. Phys. **83** 4069 (1985).

[69] Evans, D. J., W. G. Hoover, B. H. Failor, B. Moran, and A. J. C. Ladd. Phys. Rev. A **28** 1016 (1983).

[70] Ashurst, W. T. and W. G. Hoover. Phys. Rev. A **11** 658 (1975).

[71] Liem, S. Y., D. Brown, and J. H. R. Clarke. Phys. Rev. A **45** 3706 (1992).

[72] Holleman, I., G. von Helden, A. van der Avoird, and G. Meijer. J. Chem. Phys. **110** 2129 (1999).

[73] Bartoli, F. J. and T. A. Litovitz. J. Chem. Phys. **56** 413 (1972).

[74] Bulkin, B. J. and K. Brezinsky. J. Chem. Phys. **69** 15 (1978).

[75] Edington, D. W. N., P. R. L. Markwick, W. C. K. Poon, H. Vass, and J. Crain. Phys. Rev. Lett. **82** 3827 (1999).

[76] O'Reilly, D. E., E. M. Peterson, and D. L. Hogenboom. J. Chem. Phys. **57** 3969 (1972).

[77] Andreozzi, L., N. Giordano, and D. Leporini. J. Noncrystalline Solids **235** 219 (1998).

[78] De Smet, K. and L. Hellemans. Phys. Rev. E **57** 1384 (1998).

[79] Bée, M., J. L. Sauvajol, and J. P. Amoureux. J. Physique **43** 1797 (1982).

[80] Longueville, W., M. Bée, J. P. Amoureux, and R. Fouret. J. Physique **47** 291 (1986).

[81] Yildirim, T., P. M. Gehring, D. A. Neumann, P. E. Eaton, and T. Emrick. Phys. Rev. B **60** 314 (1999).

[82] Chen, C., Y. Sheng, S. Yu, and X. Ma. J. Chem. Phys. **101** 5727 (1994).

[83] Henseler, A. and E. Vauthey. Chem. Phys. Lett. **228** 66 (1994).

[84] Heitz, M. P. and F. V. Bright. J. Phys. Chem. **100** 6889 (1996).

[85] Williams, A. M., Y. Jiang, and D. Ben-Amotz. Chem. Phys. **180** 119 (1994).

[86] Ha, T., J. Glass, T. Enderle, D. S. Chemla, and S. Weiss. Phys. Rev. Lett. **80** 2093 (1998).

[87] Nafie, L. A. and W. L. Peticolas. J. Chem. Phys. **57** 3145 (1972).

[88] Imeshev, G. and L. R. Khundkar. J. Chem. Phys. **103** 8322 (1995).

[89] Stein, A. D. and M. D. Fayer. J. Chem. Phys. **97** 2948 (1992).

[90] Depondt, P. and W. Breymann. Mol. Phys. **87** 1015 (1996).

[91] Affouard, F. and P. Depondt. Mol. Phys. **93** 703 (1998).

[92] Press, W. H. et al. Numerical Recipes, The Art of Scientific Computing, chap. 14. Cambridge University Press (1986), (502).

[93] Barrow, R. F. et al. A Specialist Periodical Reports, 2 of Molecular Spectroscopy, chap. 3. Billing & Sons Limited, London (1974), (184).

[94] Bansal, M. and A. Roy. Mol. Phys. **38** 1419 (1979).